TECHNISCHE UNIVERSITÄT WIEN
Vienna University of Technology

Dissertation

Novel Atomchip Technologies with Superconductors

ausgeführt zum Zwecke der Erlangung des akademischen Grades eines Doktors der technischen Wissenschaften unter der Leitung von

Univ.Prof.-Ing. Dr.techn. Hannes-Jörg Schmiedmayer
E141
Atominsitut

eingereicht an der Technischen Universität Wien
Fakultät für Physik

von

Fritz Randulf S. Diorico MSc.
(Matrikelnummber: 1029325)
Stättermayergasse 17/1660, 1150 Wien
8 Ganciang Street, Punta Princesa, Cebu City, Philippines 6000

Wien am October 2016 ....

Diese Disstertation haben Begutachtet: ....
J. Schmiedmayer R. Dumke

"The only thing necessary for the triumph of evil is for good men to do nothing."
Edmund Burke

Abstract

Novel Atomchip Technologies with Superconductors

This thesis reports on the group's efforts and experimental advancements on combining two different fields in physics namely ultracold atomic physics and superconductivity. The main aim is to couple ultracold atoms to superconducting microwave resonators for quantum information applications. Apart from opening up possibilities for hybrid physics experiments, the constructed experimental setup allows for the probing of superconducting surfaces using ultracold atoms. Or the other way, superconducting properties can be utilized for novel atomchip traps.

Along with this endeavor comes many technical hurdles between the different fields that need to be overcome. These are mainly in the technicalities of transporting ultracold ^{87}Rb atoms to a cryogenic environment. A realization of a robust magnetic transport scheme to bring 3×10^8 ultracold ^{87}Rb atoms into a 4K cryostat has been constructed. It begins with standard laser cooling and trapping of ^{87}Rb atoms, then transportation of the atoms first horizontally, then vertically through radiation shields into a cryostat by a series of normal- and superconducting magnetic coils. After subsequent pre-cooling in a quadrupole-Ioffe trap, about 3×10^6 atoms at $30\,\mu$K are loaded on a superconducting atomchip.

The superconducting atomchip can be fabricated from any superconducting material. Unlike its normal conducting counterparts, superconductivity brings in new features that can be useful to atomchip trapping especially the critical state behavior of Type-II superconductors. In this thesis, niobium and YBCO atomchips are designed, fabricated and studied. The various designs include features either for cQED applications with microwave resonators or novel superconducting traps for ultracold atoms using the remnant magnetization of the superconducting surface (vortex-like traps).

Evidence of a current-induced remnant magnetization behavior of type-II superconductors has been measured with ultracold atoms. This hysteresis behavior is used to control the current distribution of the trapping wire either with a magnetic field or a current pulse. Control of the transport current distribution with a current pulse is studied in great detail. A major consequence of this is the ability to tune or tailor the effective width of the trapping wire, by controlling the current-pulse history experienced by the superconductor. Understanding how superconductivity affects atomchip trapping of ultracold atoms will be instrumental for the ultimate goal of coupling to a superconducting resonator or using superconducting vortices/periodic superconducting structures to create a lattice traps for ultracold atoms.

Table of contents

Chapter 1

Introduction

1.1 A brief history of quantum nature of matter

Over the past hundred years, there has been a major revolution in modern physics particularly in quantum physics. Physicists began to venture beyond the classical picture that limited our understanding of the universe. It was not until the development of the wave mechanics understanding of matter that the course of physics was forever changed. We now know that at very small scales (eg. atoms and molecules), matter behaves like a wave. A consequence of this is that the position and momentum of a particle can not both be known precisely at the same time. This is known as the Heisenberg uncertainty, $\Delta x \Delta p \geq \hbar/2$ [1, 2]. This means that at the very small scale the position of sub-atomic particle becomes statistical or probabilistic. However, this wave nature is not visible at a larger scales since most massive objects, like everything around us, are too warm. The probabilistic nature of matter at room temperature collapses into a point which is why we don't readily observe people disappearing and re-appearing at train station platforms.

In 1924, de Broglie proposed a formula that describes how to observe the wave nature of matter. This is the de Broglie hypothesis, $\lambda_{deB} = h/p$ which up to now is still very relevant to our understanding of nature. This tells us which wavelength scale allows observation of the quantum nature of matter. Fast moving particles (high momentum, p) such as electrons accelerated in the kV regime have a de Broglie wavelength of the order of picometers. It was in around 1927, where George Thomson, son of J.J. Thomsom [3] demonstrated electron interference by accelerating electrons through a thin metal film. Ten years later, electron diffraction was observed through the crystalline structure of Nickel [4]. A similar behaviour was also eventually observed in Neutrons [5] here in the Atominstitut and other even more massive objects such as molecules more recently [6]. Just like electromagnetic waves, the same interference experiments can be performed with matter waves.

For a thermodynamic neutral gas, $p \propto \sqrt{T}$ [7, 8]. As such, it is clear that cooling down matter increases its de Broglie wavelength. For a thermal cloud of neutral atoms at a certain temperature, one can imagine that the de Broglie wavelength can become larger than the distance between neighboring particles. Eventually, below a critical temperature T_c, the entire ultracold atomic ensemble will form a degenerate system where each of the atoms has become indistinguishable from all others because its wavefunction extent is comparable to the de Broglie wavelength. This is the onset of the formation of the Bose-Einstein Condensate (BEC), a state that, because of the Pauli exclusion principle, occurs only with Bosons which can condense into this degenerate ground state. This new state of matter was first theorized by A. Einstein and S. N. Bose through a series of correspondence letters. S. N. Bose was initially looking at quantum statistics of photons which A. Einstein generalized and applied to integer spin particles, henceforth called bosons [9, 10]. They further theorized the formation of a new state of matter (BEC) below a critical temperature [11, 12].

1.2 Cryogenics and Quantum Degenerate Systems

Cooling of systems or atoms has been a big industrial breakthrough throughout the last hundred years. It allows preservation of most of our agricultural products and is also essential to fundamental physics. It was even posed as a challenge more than a hundred years ago to whoever can liquify Helium[1] first [13]. Kamerlingh Onnes initial and successful attempts to liquify Helium pushed refrigeration techniques down to 4.2 K where he discovered the resistance drop of Mercury to zero. In 1938, using similar refrigeration techniques, superfluid behaviour of Helium-4, where the substance flows with zero friction and zero viscosity, was discovered [14, 15]. This new state of matter is related to the formation of a Bose-Einstein Condensate since the isotope Helium-4 is bosonic whereas Helium-3 is fermionic. It wasn't until the development of laser cooling and trapping techniques combined with evaporative cooling that lead to the first production of a BEC more than twenty years ago[2]. The invention of the laser has allowed probing of the discrete energy levels of the atom through spectroscopy [17]

[1] Helium, He liquifies at 4.2 K.

[2] The connection between superfluidity and Bose-Einstein Codenstation is not that obvious. Superfluid Helium-4, though displays BEC characteristics where a fraction , is more of a strongly interaction quantum liquid [16]. A dilute BEC of ^{87}Rb, for example, is described by the Gross-Pitaevsky equation. The connection is subtle and is further discussed in [11]

and is very important for modern day photonics. Nobel Prizes were awarded to the founders of the experimental implementation of laser cooling and the first people to create a BEC in the laboratory [18–22].

1.2.1 Ultracold atoms

The creation of a Bose-Einstein Condensate in the lab has produced a new field of research. For the first time in the history of science, physicists have a toy-like-model that allows quantum simulation of other systems. Physicists have gained access to a purely degenerate quantum system that can be manipulated with great precision and accuracy either with light or magnetic fields. Matter Wave properties of BECs can be thoroughly studied and have been exploited for various applications such as metrology and sensing to name a few [23–26]. Fudamental properties of coupled 1D systems, even simulating Josephson junctions, have been studied with BECs [27, 28]. Interfering laser beams create an optical lattice which can be used to simulate Solid State Systems in ways never possible with Condensed Matter Physics [29–31]. With the vast amount of experimental control, it is even possible to simulate Abelian and non-Abelian gauge fields in ultracold atoms [32–37, 8].

1.2.2 Superconductivity: Cooper Pairs

On another side of the spectrum, it is also possible to create a Bose-Einstein Condensate inside a solid. This phenomena is commonly called superconductivity. The best existing theory of behind superconductivity is the Bardeen-Cooper-Schiefer (BCS) theory [38]. Superconductivity is a unique property of certain materials that exhibits zero resistance, and therefore zero heat dissipation, upon transport of electric current. In short, below a critical temperature, electrons pair up to form a loosely bound state due to phonon interactions with the crystal lattice. These pairings called Cooper pairs have an energy gap around the Fermi level which inhibit collisional interactions that produce resistivity. This is the main property of superconductors that makes them very attractive for new technologies, since the zero-resistivity implies zero heat dissipation for a transport current. Cooper pairs form a net interger spin since they are formed by two fermions. They also form a degenerate system similar to that of BECs with normal bosonic atoms or molecules[3]. Similar physics can be observed in both systems like the Josephson effect and even vortices [28, 11].

Since their first discovery and inception, superconductors have been widely used in many technologies mostly due to their vanishing thermal heat dissipation. Superconductors strongly rely on cryogenics to cool it down below the critical temperature. The non-existent heat dissipation makes it perfect for producing high magnetic fields required for accelerators, magnetic levitation for transport applications, and medical imaging devices (MRI machines). It is also promising in more advanced computation with rapid single flux quantum technology or traditional electronics fabricated on niobium [39]. With the advent of high T_c superconductors, rf and microwave filters are now made from lithographically structured YBCO or MgB_2.

With the increasing demand for computing power, scientists and engineers have been working hard to fulfill Moore's law year by year. Physicists, on the other hand are looking towards a different direction where one utilizes quantum phenomena for computation. Since the revolution of modern physics, the emergence of quantum technologies has brought a new level of experimental control on a wide range of physical systems. The quantum nature of matter has not only been unraveled but also exploited in recent emerging quantum technologies [40].

Recent advances in building alternating layers of superconductor/insulator structures have created Josephson junctions, which are the building blocks of superconducting quantum interference devices (SQUIDS). This eventually led to the field of superconducting quantum circuits (SQC) which is very promising for quantum information processing. Quantum computing has the potential of extending Moore's law as classical computation with CMOS technology will eventually reach its limit. At the time of writing this thesis, 10 nm CMOS technology is under commercial development set to be released in 2017 [41]. A quantum bit (qubit) storage can be engineered using the Josephson effect or persistent super-currents and has been improved through several versions throughout the years [42–47]. It is already possible to create a multi-qubit quantum computer with recent advances in superconducting quantum circuits [48, 49].

[3] As similar as they can be to atomic/molecular BECs, Cooper pairs are formed by long range interaction between electrons and lattice phonons. This long range interaction is around 1000 nm which is significantly larger than the crystal lattice. Atomic/Molecular BECs are usually mediated by short range interactions. However, recent experiments with laser cooling and trapping of ultracold atoms and molecules have shown tunable interaction lengths with the Feshbach resonance enough to study the BEC-BCS crossover [11]. This topic is another interesting field that is beyond the scope of this thesis.

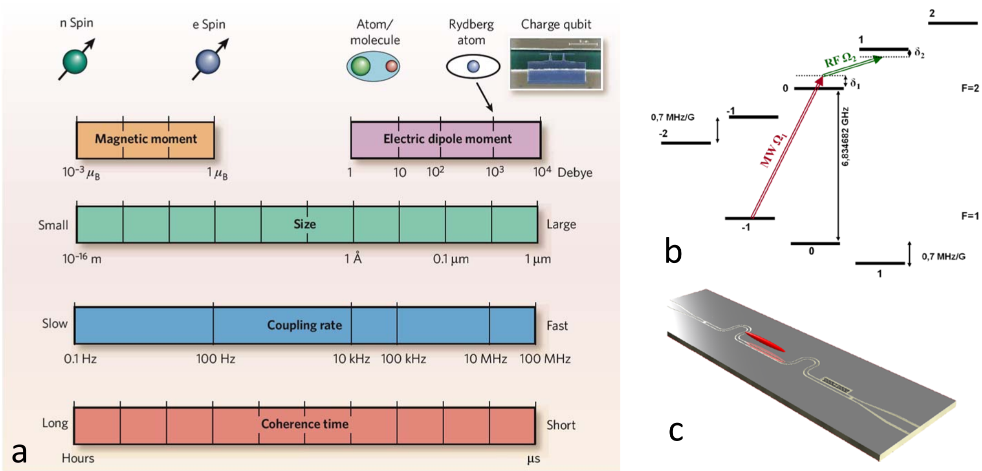

Fig. 1.1 Overview on Hybrid Quantum Systems with cavity Quantum Electrodynamics (cQED). (a) shows the different particle size scales and their corresponding coherence times and coupling rates. Taken from [68]. (b) and (c) shows ground state of ^{87}Rb ground state highlighting the clock state involving a two-photon transition between a microwave and rf photon. Both taken from [69]

1.2.3 Hybrid Quantum Systems

Superconducting quantum circuits offer promising scalability. However, SQCs still lack in qubit memory storage time compared to its coupling rate (See figure 1.1). Typical SQCs are fabricated on niobium and operated at mK temperatures with a dilution refrigerator. These circuits can have a qubit decoherence time around the µs regime depending on the qubit engineering [42–47]. This has recently been pushed up to the ms regime using 3D microwave cavities [50]. However, to truly push the boundaries even further, recent proposals suggest combining SQCs with other quantum systems that have a longer coherence times. This is illustrated in figure 1.1a where the coherence times for different particle size scales are shown with their corresponding coupling rates. Atoms and molecules are very promising for qubit memory storage [51–66] since they have long coherence lifetimes. Coupling between these different systems can be achieved through cavity Quantum Electrodynamics (cQED) [67, 51]. The alternative quantum systems will serve as the ideal quantum memory storage whereas the superconducting quantum circuit will serve as the quantum processor.

1.3 Ultracold atoms near superconducting surfaces

Bringing ultracold atoms into cryogenic environments open up new horizons in implementing proposals for hybrid quantum systems. Ultracold atoms of ^{87}Rb can be trapped near a superconducting microwave resonator that acts as a quantum bus for the qubits. The clock state $|F = 1, m_F = -1\rangle$ to $|F = 2, m_F = 1\rangle$ through a virtual state around $|F = 2, m_F = 0\rangle$ of the D2 line of ^{87}Rb is a perfect candidate for storing a qubit [70]. Figure 1.1b illustrates the hyperfine ground state of ^{87}Rb showing the clock transition. Figure 1.1c shows a 3D rendering of a ^{87}Rb atomcloud close to a superconducting coplanar waveguide resonator [59, 60]. The atoms can be magnetically trapped by a nearby microwire structure [71]. This can also be done with lumped-element resonators (inductor-capacitor, or LC circuits) [69, 72].

Ultracold atoms near superconducting surfaces also open up the path towards new quantum technologies [40]. For instance, Johnson-Nyquist noise from the thermal agitation of electrons is absent in superconductors in the virgin state. This has led to theoretical predictions of atomic lifetimes greater by several orders in the vicinity of superconductors compared to normal conductors and up to 100 s-1000 s in the mixed state [73–76]. This lifetime enhancement is the main motivation for probing Rydberg states in cryogenic environments [77]. Furthermore, persistent currents or "supercurrents" can be induced in superconductors via flux cooling around a superconducting closed loop structure. In fact, the very first superconducting atomchip trap was made from a persistent current on a niobium Z-type structure [78, 79]. With type-II supercondutors in the mixed state, remnant magnetization traps from the penetrated vortices can be created [80, 81]. This new form of trapping can also be considered as belonging to the class of permanent traps using permanent magnets [82]. However, in this case, the material is in the superconducting state and one advantage is that the magnetization is tunable and can be controlled to a certain degree of precision [83–86].

Recently, new forms of microchip-based lattice traps have been proposed using superconductors [87, 88] because superconductors such as niobium can be nanofabricated down to 100 nm or less, creating lattice spacings that can rival optical lattices [30]. This can either be done by trapping atoms directly with superconducting vortices in the Abrikosov lattice [87, 89], through periodic superconducting structures such as rectangular or disk structures [84, 81, 90, 88] or through ladder-like structures like in [82], which is yet to be realized.

The magnetization of type-II superconductors is found to be the major contributor in the course of the experiment. In its infancy, superconducting effects, especially magnetization, were ignored, since our superconducting atomchip was mostly treated as a normal conducting wire. One of the biggest discoveries of this work is that the magnetization of the superconducting film that was used plays a very important role in the current flow that creates the superconducting trap. Recent measurements indicate that current flow in the 200 µm wide Nb Z-structure is not in the virgin or Meissner state, but in the mixed state through current-pulse magnetization originally proposed in [86, 85]. The results suggest that the current distribution through a rectangular cross section can be tailored by varying the current history experienced by the superconductor which changes the effective width of the wire cross-section. The results of which are discussed in great detail in chapters 6 and 7.

1.4 Current endeavors of transporting ultracold atoms into cryostats

A major part of this thesis deals with the transport of ultracold ^{87}Rb atoms into a cryostat using a magnetic conveyor belt scheme [91]. Only a handful of similar experiments exist in the world. Reviewing existing setups will be important in improving the current setup at the Atominstitut.

Cryogenic systems offer a major experimental hurdle to Magneto-Optical Traps (MOT). Typical MOT ultra-high-vacuum (UHV) chambers require pressures down to 10^{-9}mbar and as well as a material vapor of the desired species in the chamber atmosphere. In most cases, the chosen species is Rubidium. Rubidium is usually taken from a dispenser which is heated up through an applied current. At a certain current, depending on manufacturer specifications, Rubidium 85 and 87 are dispersed into the chamber. As such, it is difficult to imagine a cold cryostat head inside a Rubidium MOT because of the major heat source that being the Rubidium dispenser.

There were initial attempts to combine cryostats directly into a MOT chamber by building a unique Rubidium dispenser using an electron beam [92]. Despite the promising results, the atom trapping rate was found to be too low for practical use. Therefore, an investigation of different loading schemes for a cryostat was undertaken [93]. The best way to bring ultracold atoms into a cryogenic environment is to trap them elsewhere and transport them to the new cryogenic environment.

Historically, the first experiment bringing ultracold atoms into a cryostat was achieved using an optical push beam from a MOT located below a cryostat [94]. The final superconducting trap was a niobium Z-structure where a ^{87}Rb BEC was also created [95]. The experiment intended to utilize the very long atom lifetime in the cryogenic environment to probe and study long-lived Rydberg states [77]. This was followed by efforts in Japan using a brute force approach by physically moving a pair of magnetic coils, which created a magnetic trap, along a motorized railway into a cryostat in order to create novel supercondcuting traps [78, 79, 96]. Subsequent experiments in

Germany involved adding a cryostat to already working BEC experiments. There, a few arrays of magnetic coils transfer the ultracold atoms to a superconducting atomchip attached to a flow-type cryocooler [97]. Since then that same group has also attempted to build a magnetic transport geometry identical to the one described in this thesis to bring ultracold atoms into a dilution refrigerator [98, 99]. Most of the groups mentioned above were using Helium based cryostats that allow them temperatures from 4.2 K down to 20 mK. It is also important to note that liquid Nitrogen experiments were also pursued with great success by R. Dumke's group in Singapore [100]. As mentioned briefly in the previous section, they have produced excellent results in interfacing superconducting properties, especially that type II superconductors and ultracold atoms [83, 85]. Lastly, there are also attempts to bring cryogenic surfaces directly into a room temperature MOT chamber [101].

The implementation of transporting ultracold atoms into a cryostat in this thesis is mainly an extension of the magnetic transport originally proposed and built by [91]. The setup involves a horizontal array of magnetic coil pairs that run along the MOT UHV chamber into a corner 205 mm away. From there, the atoms are vertically transported into a cryogenic environment about 215 mm upward. The transition from horizontal to vertical is new and pioneered by our experiment [99] and has already become the choice of magnetic transport for other groups [98].

1.5 Report structure

Since this thesis involves various combinations of topics in experimental physics, there won't be a dedicated theory chapter. However, theory will be discussed where necessary. This thesis is comprised of several parts. The first part deals with the heart of the experiment which is the magnetic conveyor belt transport scheme to bring ultracold atoms into a cryogenic environment. It starts with a brief theoretical chapter to review basic concepts of laser cooling and trapping of neutral atoms, more specifically ^{87}Rb. It then follows with an in-depth chapter explaining major aspects of the experiment. New components and schemes introduced to the experiment which were not present in its infancy will be discussed in detail [102, 103, 93]. The second part of this thesis deals with the final superconducting trap, namely the quadrupole-Ioffe configuration (QUIC) chapter 4 and the subsequent loading into a superconducting atomchip which will be discussed in chapter 5. Radio-frequency (rf) cooling trapping attempts in the QUIC trap and in the superconducting atomchip trap will be discussed briefly in chapter 4 and 5. Chapter 6 will discuss on magnetic field microscopy (MFM) using ultracold atoms above a niobium structure. These results are compared to magnetic field microscopy with a μHall probe in collaboration with Low-Temperature-Physics group in the Atominsitut [104]. The last part of this thesis discusses applications of ultracold atoms close to a superconducting structure and vice versa. Basic superconductor theory especially on the cross-sectional current distribution under various conditions will be discussed. Their implications to superconducting traps will be presented along with experimental measurements. Recent results on how the effective width of the superconducting wire trap can be tailored through current pulses will be discussed in detail. Some further outlook will be given on how superconductors can be used for novel atomchip traps and as well as hybrid quantum systems with superconducting microwave resonators.

Part I

Magnetic transport of ultracold atoms into a cryostat

Chapter 2

Laser cooling and trapping of ultracold atoms

The forces light can induce on matter is the main essence of laser cooling. The two components of the light induced force are namely radiation pressure and the dipole force. The force from the radiation pressure depends on the presence of a phase gradient of the laser beam while dipole force depends on an intensity gradient[1]. The latter can be used to create optical traps as in optical lattices. For monochromatic light interacting with a two level system, the radiation pressure force is proportional to laser detuning, $\delta = \omega_{laser} - \omega_{atom}$. The Doppler effect also plays an important role for laser cooling. For $\delta < 0$ or red-detuned light, an atom moving towards the beam propagation will be closer to resonance than atoms moving in the same direction as the beam. Thus, these atoms will scatter more and experience a deceleration in contrast to atoms moving in the same direction as the beam. This process is known as Doppler cooling. With this concept, it is easy to imagine how to construct a laser cooling setup. For a single axis, this is done by two counter propagating beams. Extending this to all spatial dimensions would require three pairs of counter propagating beams along the x, y, and z directions (eg. counter-propagating $\sigma_+ - \sigma_-$ beams on each axis).

The lowest temperature possible is defined by the Doppler limit, $T_D = \hbar\Gamma/2k_B$ where k_B is the Boltzmann constant and Γ is the natural linewidth of the atomic excited state [105]. This is about 144.1 µK for ^{87}Rb. During the early years of laser cooling experiments, it was found that this limit can easily be brought down to the recoil or sub-Doppler limit, $T_R = \hbar^2 k^2/2Mk_B$ which is about 0.7 µK for Rubidium [105–107]. The extra cooling mechanism comes from the polarization gradient in counter-propagating light fields. Polarization gradient cooling or sub-Doppler is possible with a lin $\perp$ lin

[1]An intensity gradient can be created by the interference of counter propagating laser beams.

configuration and as well as a $\sigma_+ - \sigma_-$ configuration. Both configurations produce similar sub-Doppler cooling results but differ in their cooling mechanism.

In the lin $\perp$ lin configuration, counter propagating beams of linearly polarized beams with orthogonal orientation, interfere to create a standing wave that alternates between σ_+, π', and σ_- polarizations[2] over a quarter of the laser wavelength. The changing polarization induces a sinusoidal light-shift between the ground states. As atoms roll down in the sinusoidal landscape and reaches a maximum, the atoms get optically pumped to the excited state and due to the transition rules and probabilities, will re-emit a photon with an extra momentum which corresponds to the light shift. Consequently, for every hill maxima roll, pumping, and emission cycle, the atoms keep losing energy. This is often called the Sisyphus effect.

For the $\sigma_+ - \sigma_-$ configuration[3], the mechanism is very different. There is no sinusoidal light-shift on the ground state; thus, Sisyphus effect is not possible. However, due to motion-induced atomic orientation, there is still strong differential radiation pressure between both counter-propagating beams. The motion-induced atomic orientation creates a population imbalance within the ground states which create this differential radiation pressure and consequently a net friction force.

Both configurations create net frictional forces which only become significant at lower atomic velocities. This laser cooling scheme that goes beyond Doppler cooling is usually called Optical Molasses since atoms move in a pseudo-medium where they are slowed down analogous to how an object would be slowed down in honey syrup.

2.1 Magneto-Optical Trap

So far, the cooling schemes discussed do not trap the atoms since there is no restoring force present. In order to laser cool, trap, and compress the atoms at the same time, one needs to combine laser cooling with magnetic fields to create a Magneto-Optical Trap (MOT). To illustrate, imagine a simple transition between $J = 0$ to $J = 1$ (figure 2.1). The Zeeman shift of the exicted state $J = 1$ will split along a degenerate point on the zero-point crossing of the anti-Helmholtz field. The addition of an inhomogenous linear magnetic field (eg. fields from an anti-Helmholtz configuration), creates a splitting of the Zeeman sublevels of the excited state of the atoms. This creates a position dependent scattering in combination with the selection rules. With three red detuned, $\sigma_+ - \sigma_-$ orthogonal counter-propagating beams and depending on which side the atoms

[2]See the nomemclature page at the end of this thesis for light polarization defnitions.
[3]Counter propagating right and left circularly polarized beams.

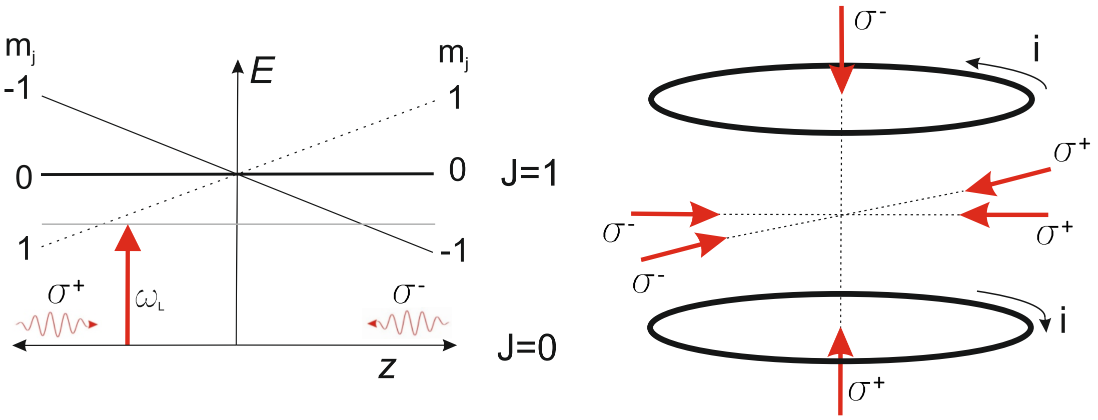

Fig. 2.1 Magneto Optical Trap basic scheme. (Left) shows the energy level scheme for a basic $J=0$ to $J=1$ transition. For ^{87}Rb D2 line, this is the $F=2$ to $F'=2$ transition which is a bit more complicated. But this simplified scheme gives a basic overview of the cooling and trapping scheme with the MOT. (Right) shows the beam polarization configuration with the coils producing the quadrupole fields.

are located, there will be a differential absorption between the ground state and the closest Zeeman excited sublevel with either σ_+ or σ_- applying selection rules. This creates a restoring force for the atoms which traps and compresses them as well as laser cools them to the zero-field point.

Figure 2.2 shows the energy level scheme of the Rubidium D2 line. The cooling transition goes from the $F=2$ ground state to the $F'=3$ excited state. The cooling transition is not closed. There is a small probability that the atoms get excited into the $F'=2$ excited state. The atoms will then decay into the $F=1$ ground state and thus be lost from the laser cooling cycle. An additional repumping beam brings the atoms back into the cooling cycle. Fortunately, ^{87}Rb only requires one rempumping beam to close the cooling cycle.

2.2 Magnetic trapping and Bose Einstein Condensation

Condensation into a ground state (BEC) is not possible with an optical molasses and/or MOT due to recoil heating. Atoms have to be loaded into a trap with sufficient potential trap depth to accommodate the Boltzmann tail of the laser cooled atomic cloud. A very useful tool to manipulate neutral atoms is through magnetic trapping.

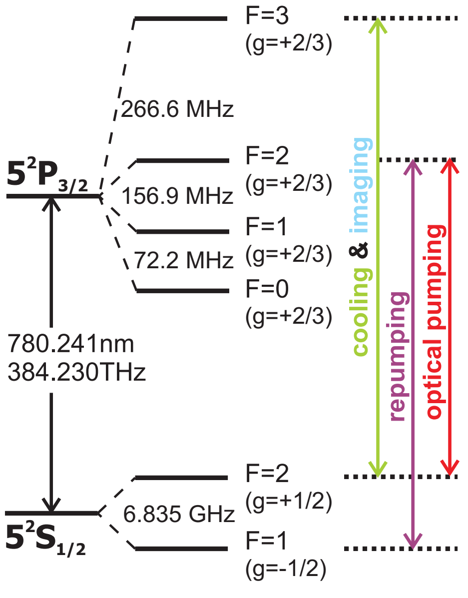

Fig. 2.2 ^{87}Rb D2 energy level scheme used for laser cooling. Taken from [102].

A neutral atom experiences a potential from a magnetic field landscape

$$V_{mag} = -g_F \mu_B m_F B$$

where g_F is the Lande-factor, μ_B is the Bohr magneton and m_F is the magnetic quantum number. Depending on whether $g_F m_F < 0$ or $g_F m_F > 0$, neutral atoms can be trapped either as high-field-seekers or low-field-seekers, respectively. In reality, however, a magnetic field maximum violates Earnshaw theorem, therefore, high-field-seeking atom traps are not favorable. Thus, most of magnetic manipulation with ultracold atoms is done with low-field-seeking states.

For ^{87}Rb, the $F = 2$ ground state can be used for magnetic trapping with $m_F = -2, -1, 0, 1, 2$. It is important to note that zero-field points create degeneracy from the Zeeman shift of the sublevels. This makes atoms forget their spin and fly off the trap, Majorana spin flips. The states $|F = 2, m_F = 1\rangle$ and $|F = 2, m_F = 2\rangle$ are both low-field seeking states with the latter being the strongest. To achieve condensation into a Bose-Einstein condensate (BEC), it is important to have a non-zero trap bottom in order for the atoms to remain in their low-field seeking state. For more information on magnetic trapping and its various applications, please refer to [108].

To achieve a Bose-Einstein in magnetic trap, evaporative cooling with radio-frequency (rf) fields is used. Since the Zeeman sublevels are shifted according to m_F with the magnetic field at the local position, atoms can be out coupled with rf field

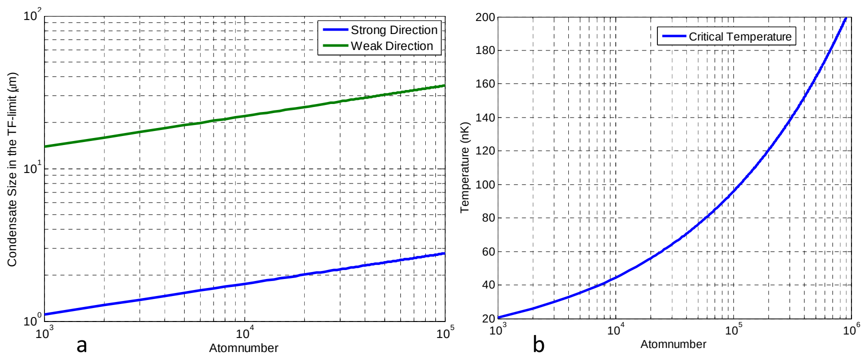

Fig. 2.3 (a) BEC Atom number versus size for a 2D trap eg. QUIC trap with 20 Hz×200 Hz and (b) Atomn number versus Critical Temperature for the condensation of ^{87}Rb

to other m_F states. For a magnetic trap, the atomic cloud can be evaporatively cooled by removing warmer atoms occupying the warm tail of the Boltzmann distribution. As this tail is removed, the atoms rethermalize to form a colder cloud analogous to the cooling down of freshly brewed coffee. For a deep magnetic trap, the Boltzmann tail is located at the outer shell of the atomic cloud. A decreasing rf frequency starting from a sufficiently high frequency to address the warmest atoms can effectively cool down the atomic cloud below the critical temperature towards condensation. In experimental physics, this is often called, an "rf knife." The rate of the rf knife depends entire on the trapping geometry, atom number and initial atomcloud temperature. Figure 2.3 shows the size and critical temperature transition versus atomnumber for a ^{87}Rb BEC. As the critical temperature is reached the phase space density (psd) $n\lambda_{deB}$ of the cloud also reaches or exceeds 2.612 where n is the particle density in space and λ_{deB} is the thermal de Broglie wavelength. Realistic BECs in atomchip experiments have atomnumbers from 10^4 to 10^5. For a 2D cigar shaped trap with trapping frequency 20 Hz×200 Hz as in several atomchip and quadrupole-Ioffe traps, this corresponds a BEC size in the Thomas-Fermi limit of about 30 µm to 40 µm in the weak direction and about 2 µm to 3 µm in the strong direction.

Chapter 3

Experimental setup: Magnetic conveyor belt transport of ultracold atoms into a cryostat

This chapter will outline and discuss important components of the experiment. An overview of the entire system will be presented first, followed by a detailed explanation of each section. The main highlight of this chapter and overall, the thesis, is the magnetic conveyor belt transport. This process allows transport of ultracold atoms to an ultra-high vacuum (UHV) chamber which contains a cryostat. Specific details of components and CAD drawings are discussed in [109, 102]. Many aspects of the optical system have also already been discussed in great detail in previous theses [110, 93, 103]. Integral components, however, are reviewed. Only the important new additions to the existing setup are discussed in detail.

3.1 Overview of the experiment

Figure 3.1 shows a CAD drawing overview of the setup with the important internal components. The entire setup is composed of two vacuum regions namely the lower chamber containing the MOT (Magneto-Optical-Trap) and the upper or science chamber. The two chambers can be isolated via a VAT valve. With the valve closed, the vacuum in the lower chamber is maintained and the upper chamber can be brought to room pressure for repairs, maintenance or upgrades. This allows rapid replacement of the atomchip within a week if necessary. Figure 3.2 shows a photograph of the experiment. The entire setup is mounted on a $3.5\,\mathrm{m}\times1.25\,\mathrm{m}\times0.31\,\mathrm{m}$ optical table

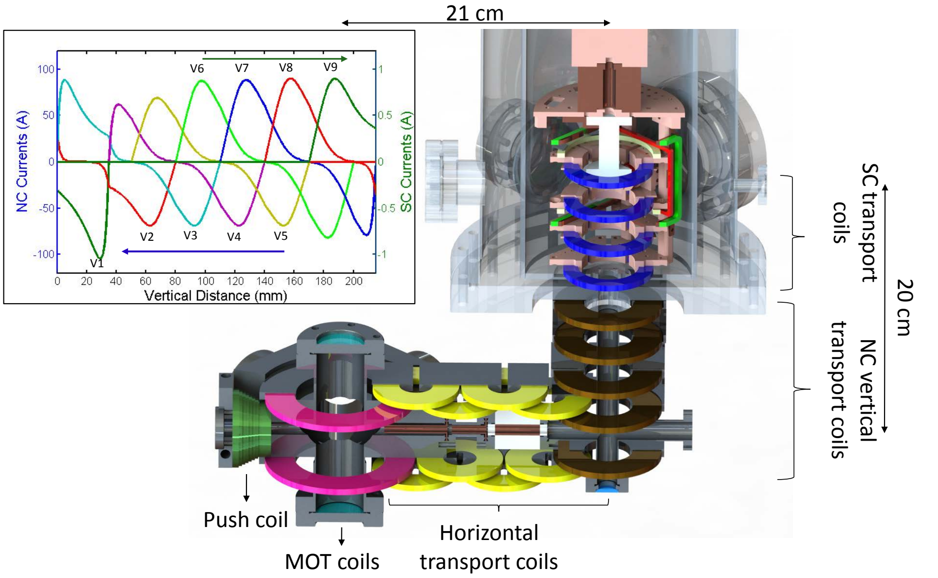

Fig. 3.1 Overview of the experimental setup.

where all the optics required for MOT and the imaging are also mounted. The entire upper chamber is supported by an item[1] structure which has a crane system in case if the cryostat needs to hoisted for maintenance and/or upgrades.

The experiment starts with laser cooling (via MOT) of the ^{87}Rb atoms for 1 s-10 s. This cools the atoms down, close to the Doppler limit of about 150 µK in the experiment. The next step is sub-Doppler cooling with optical molasses, as discussed in the previous chapter. This brings our atoms to a lower temperature of about 50 µK. After the optical molasses phase, the atoms are distributed in the $F = 2$ ground state manifold. A quantization field and an optical pumping beam (beam 1c from figure 3.3) is then applied to bring the atoms into the $m_F = 2$ strongest low-field seeking state. This is followed by switching on the initial magnetic trap formed by the MOT coils which magnetically traps the ^{87}Rb atomic cloud. The next step involves the magnetic transport to bring the atoms to the cryogenic environment. The transport takes about 1.5 s, depending on the transport settings. Specific parts of the experiment and the experimental sequence will be discussed in greater detail in the proceeding sections. Further sequences where the atoms are already in the cryogenic environment will discussed in later chapters.

[1] The original item steel structure company still exists and is called item west.

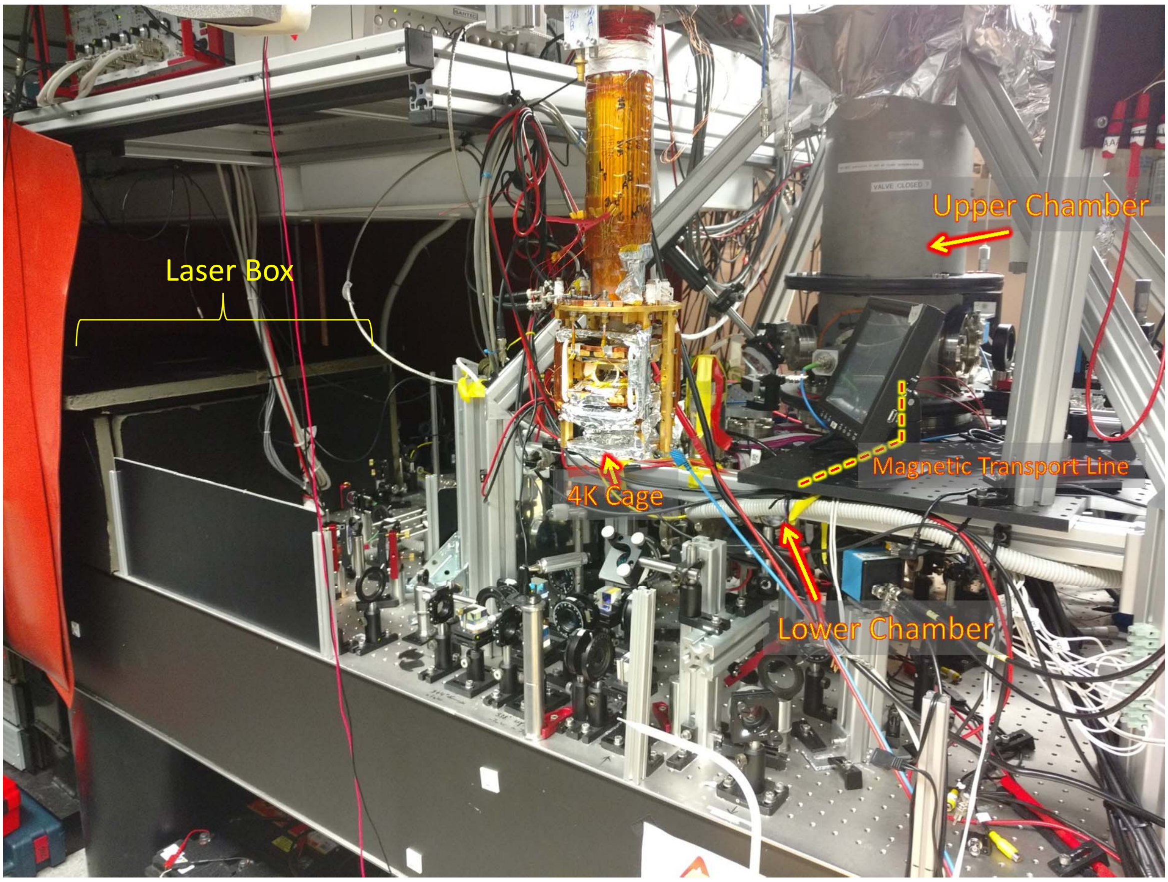

Fig. 3.2 Actual picture of the experimental setup.

3.2 Lower chamber and Laser setup

The lower main chamber is the first part of the experiment where everything begins. It is maintained by a $50\,\mathrm{L\,s^{-1}}$ ion pump at a pressure of 1×10^{-10}mbar. ^{87}Rb is obtained from six Rb dispensers (SAES Getters, inc) located just within the vicinity of the lower chamber's geometric center. The lower chamber houses the large coils which provide quadrupole fields for the MOT. These coils also serve as the initial magnetic trap for the magnetic transport (figure 3.1).

The lower chamber provides multiple optical access points, each about 2" in diameter, for the MOT beams and observation or imaging beams. The MOT beams are created by six counter-propagating $\sigma_+ - \sigma_-$ polarized laser beams and with a finger-camera aligned to look at every optical access making frequent MOT alignment easier. The main cooling beam (see figure 3.3) is produced by a Toptica TA100 laser system with a 1 W tapered amplifier diode and is beat-locked to a reference External Cavity Diode Laser (ECDL) via Frequency offset (FO). The ECDL is locked by Frequency

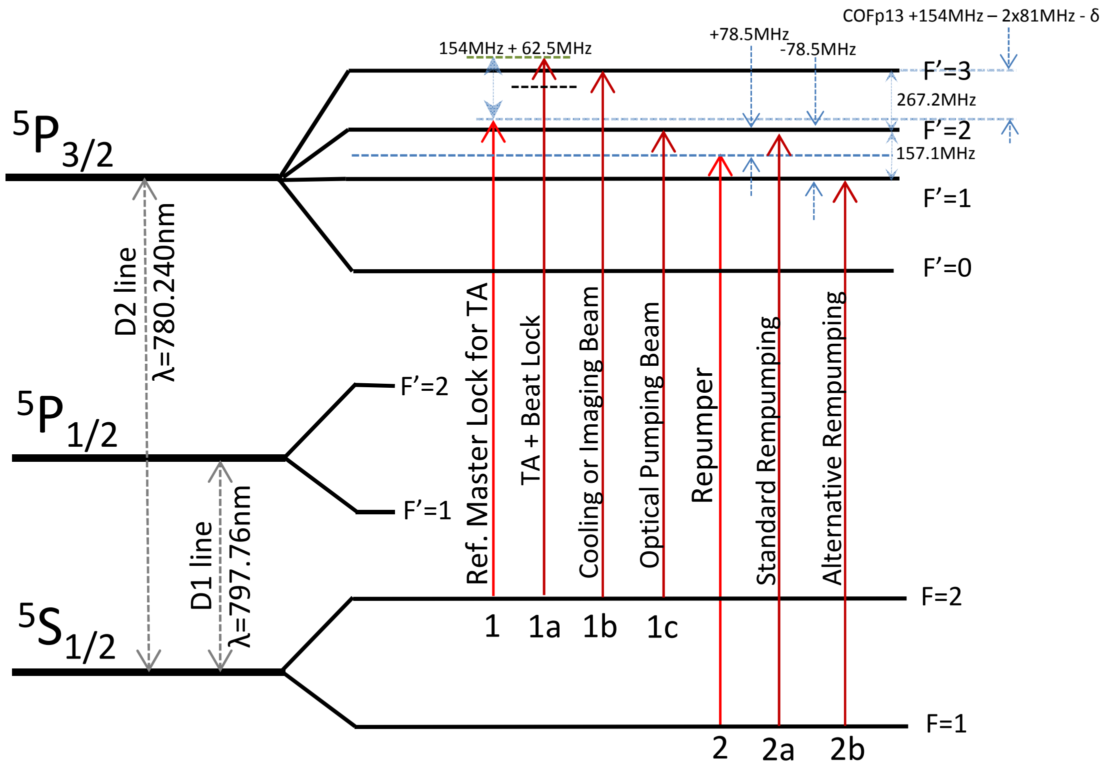

Fig. 3.3 ^{87}Rb D2 line energy level scheme used for laser cooling. The bright red transitions are the laser sources showing the corresponding cross-over lines chosen for laser locking. The dark red transitions are the corresponding frequency shifted beams either with an AOM or the beat-lock frequency offset system. Beam 1 is the reference ECDL laser beam for beat locking the TA100. Beam 1a is the resulting line from the FO beat lock and the first AOM shift of 62.5 MHz and the base offset of the beat, 154 MHz. Beam 1b is the cooling beam line which is shift by 154 MHz+62.5 MHz+δ, where the δ is the tuning possibility of the VCO. Beam 1c is the optical pumping beam taken from the zero order of the first AOM with a total shift of 154 MHz-2×81 MHz$-\delta$ relative to the $5P_{3/2}, COF' = 1,3$.

Modulation to the $5P_{3/2}, COF' = 1,3$ crossover line. The Repumper beam is produced by a Distributed Feedback (DFB) laser diode is locked to the $5P_{3/2}, COF' = 1,2$ crossover line by Frequency Modulation. Both lasers are housed in a wooden box covered with a synthetic foam material to provide acoustic shielding, as seen in figure 3.2. To probe the ^{87}Rb D2-line, Doppler free saturation spectroscopy is applied on a Rubidium Vapor cell. Specific details of the laser-locking methods and electronics involved are further discussed in [110]. The optical arrangement within the box has not changed much throughout the years and is still similar to previously published documentation [103].

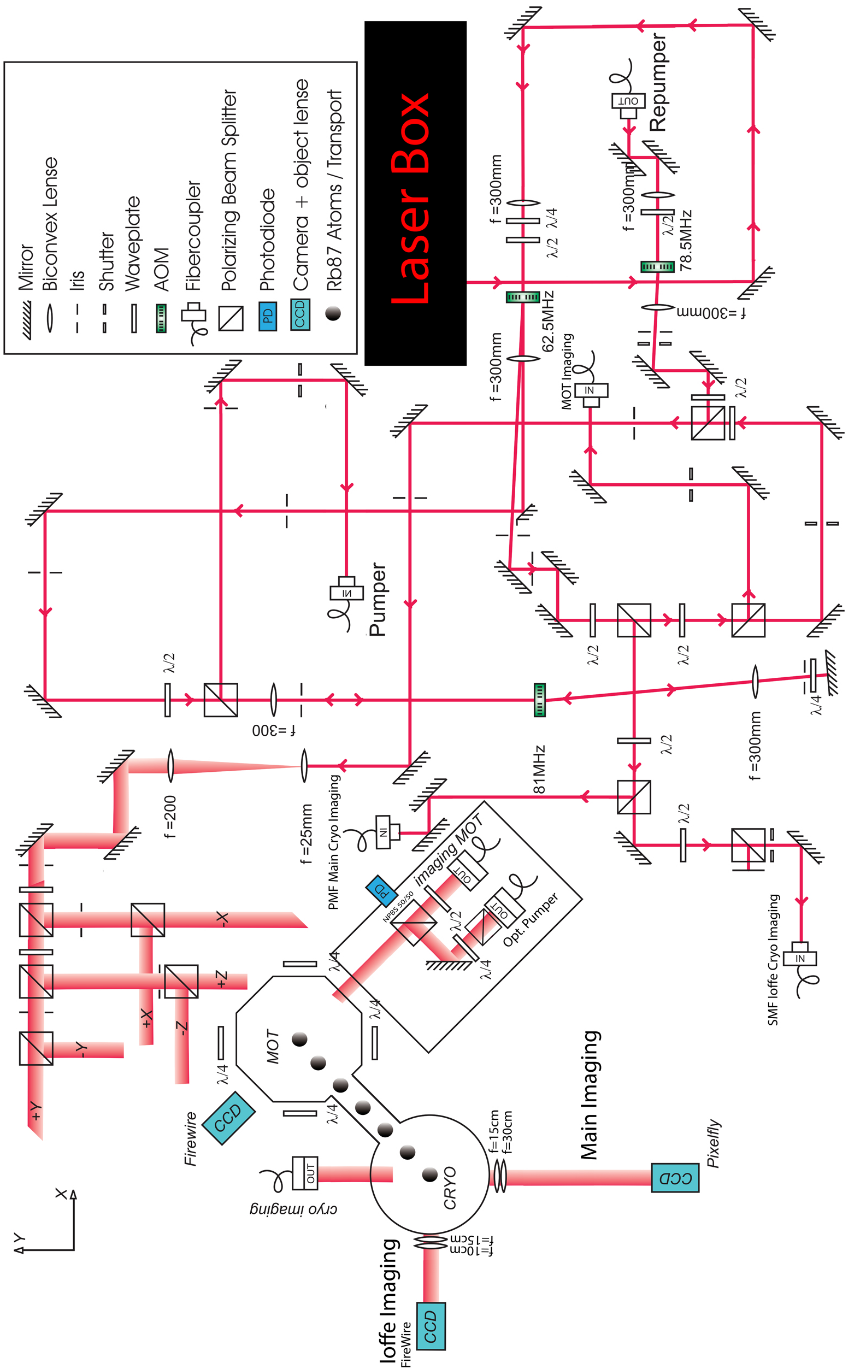

Fig. 3.4 Optical table arrangement updated from a setup previously used [103] in the lab. The laser box contains the all lasers in the setup, namely the TA100, reference ECDL, and the DFB laser. The TA100 has a 1 W Tapered Amplifier chip. It is typically set to give an output power of about 650 mW. The power coming out the rempumper fiber coming from the DFB inside the laser box is typically 14 mW. The combined cooling and repumper beams have a power of about 350 mW before entering the beam expander.

Figure 3.4 shows the latest arrangement of the optical components on the optical table, including the changes done throughout the course of this PhD. As the two beams exit the laser box, they need to be frequency shifted in ordered to obtain the MOT beams necessary, as depicted in figure 3.3. The beat FO provides a base offset of 154 MHz for the TA100 beam and can provide further detuning of $-70\,\mathrm{MHz} < \delta < 70\,\mathrm{MHz}$ with a voltage controlled oscillator (VCO). The main TA100 beam is then directed to an acousto-optic modulator (AOM) tuned to 62.5 MHz. The positive first order of the AOM is used for the main cooling line of the MOT while the zeroth order is redirected with a cut mirror to a double-pass AOM tuned to 81 MHz providing an effective shift of 162 MHz. This beam (beam 1c from figure 3.3) is used for optical pumping of the atoms to the strongest low-field-seeking state, $|F = 2, m_F = 2\rangle$.

The first half-wave plate/polarizing beam splitter (PBS cube) combination is used to clean or remove fluctuations in the linear polarization. Fluctuations in the polarization can translate into power fluctuations within both exit arms of PBS cubes in later parts of the optical path. Two PBS cubes are used to take some light for the MOT imaging and cryo-imaging. Imaging is done by absorption imaging which involves taking an image of the shadow of the atoms with a resonant beam and an image without atoms [111]. With both images plus a dark image to account for noise, an image of the atoms can be calculated (see the Appendix of [102]). The last PBS cube is used to mix the repumping beam and cooling beam, after which the combined beams are expanded to about 2” in diameter to provide six MOT beams entering the lower chamber. The repuming beam is taken out the laser box with an single mode fiber (SMF). An AOM tuned to 78.5 MHz is used to shift the beam to the $5P_{3/2}$, $F' = 2$ line.

3.3 Magnetic transport of ultracold atoms

As discussed in the last chapter, neutral atoms can be trapped in the low-field seeking state. A simple configuration of coils forming a pair with the appropriate currents can form an anti-Helmholtz configuration. Coil pairs can be used to transport cold atoms by arranging them in an array. Transport over large horizontal distance using this coil-pair array was first used by Greiner et al. [91].

Figure 3.5 shows a CAD drawing of the magnetic transport used in the experiment. The initial magnetic trap is formed by the MOT coils. In order to move the atoms to the horizontal transport direction, a massive push coil is needed to initiate the transport. By varying the currents in the coil-pair array, it is possible to move the magnetic minimum without changing the aspect ratio. This is done by having three

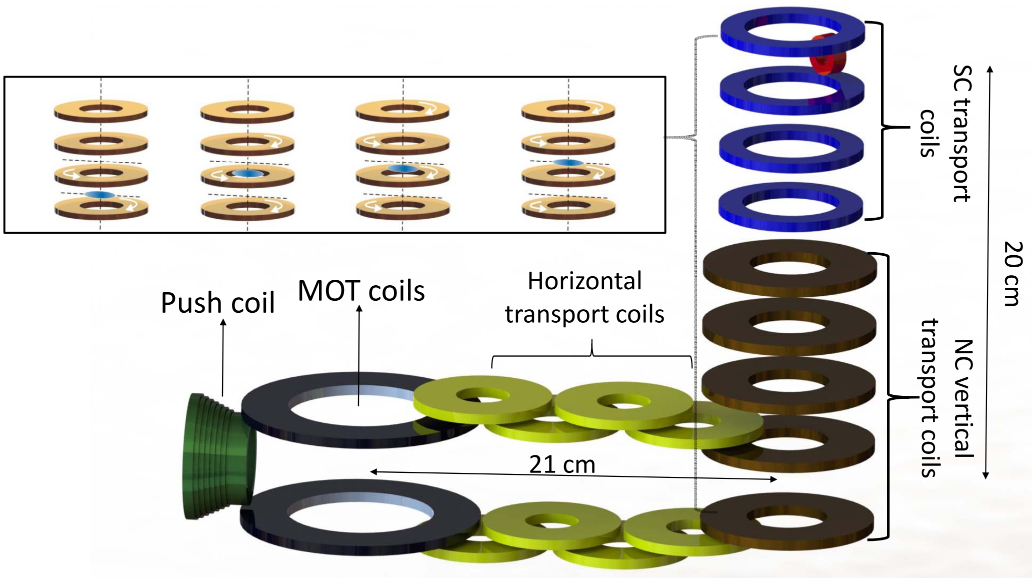

Fig. 3.5 3D CAD rendering of the magnetic transport system. The inset on the upper left-hand corner shows mechanism of the vertical transport.

coil-pairs operation simultaneously. The magnetic transport coil-pair currents are shown in the inset of figure 3.1.

In principle, a horizontal transport scheme would be enough to bring atoms into a cryogenic environment. However, the cryogenic environment will still have direct line of sight towards the room temperature chamber. A 90° turn in the transport direction avoids the direct line of sight. The geometry implemented for the horizontal transport is difficult to extend vertically due to the symmetry of the cryostat and upper chamber. Thus, vertical transport is achieved by stacking up anti-Helmholtz coils upwards as shown on figure 3.5. In this geometry, the atoms would have to cross the center of a coil, therefore bipolar operation of the coils will be required.

The magnetic transport currents has been calculated to maintain a vertical gradient of 130 G/cm which is more than enough to hold against gravity[2] and a trap minimum at the geometric center of the transport direction [93]. The horizontal transport coils and the first six vertical transport coils are all normal conducting made of copper housed in an aluminum frame with water cooling, each coil having about 30 windings [109, 102, 103]. The last four vertical transport coils are already in the cryostat and are superconducting. Each superconducting coil has 3000 windings since only a maximum current of 3 A of current is possible in the cryognetic environment whereas the normal conducting coils can go up to 200 A. The superconducting coils are made of commercial

[2]Gravity creates an effective field gradient of about 15 G/cm on ^{87}Rb.

niobium wires in a Ti-Cu filament matrix from Supercon^{Inc}. The entire magnetic transport takes about 1-2 seconds.

The last two superconducting transport coils form the final quadrupole superconducting trap for the ultracold atoms. Figure 3.6a shows an absorption image of the atom cloud in the final superconducting trap. The highest recorded atomnumber loaded into this trap was about 2×10^8 atoms at about 350 µK. There is no pressure gauge directly measuring the cryogenic environment. However, the pressure is estimated to be in the sub 10^{-13}mbar since the atoms stay trapped for very long in the cryogenic environment. This is manifested in the lifetime of the atoms which is more than 334 s as shown in figure 3.6b. Due to the large number of windings in the superconducting coils, the inductance of each coil is about 0.5 H. This creates massive induction fields when the superconducting coils are switched off in order to do time-of-flight (TOF) imaging, where the trap is switch off and, after varying waiting periods, an absorption image is made. Despite the violent induction, after about 10 ms the fluctuating fields stop and the temperature can be measured after this point [102]. The last two superconducting transport coils form the final quadrupole superconducting trap for the ultracold atoms. Figure 3.6a shows an absorption image of the atom cloud in the final superconducting trap. The highest recorded atomnumber loaded into this trap was about 2×10^8 atoms at about 350 µK. There is no pressure gauge directly measuring the cryogenic environment. However, the pressure is estimated to be in the sub 10^{-13}mbar since the atoms stay trapped for very long in the cryogenic environment. This is manifested in the lifetime of the atoms which is more than 334 s as shown in figure 3.6b. Due to the large number of windings in the superconducting coils, the inductance of each coil is about 0.5 H. This creates massive induction fields when the superconducting coils are switched off in order to do time-of-flight (TOF) imaging, where the trap is switch off and, after varying waiting periods, an absorption image is made. Despite the violent induction, after about 10 ms the fluctuating fields stop and the temperature can be measured after this point [102].

3.4 Upper chamber and Cryostat

The upper chamber of the setup is a steel chamber built in-house with optical access in four directions. It houses an Advanced Research Systems 4 K Gifford-McMahon close cycle cryostat. Figure 3.7 shows the different layers of the upper chamber system. Next to the outer steel cage is an aluminum shield that is attached to the 50 K stage of the cryostat. It has four windows for optical access made of SF57 which has negligible

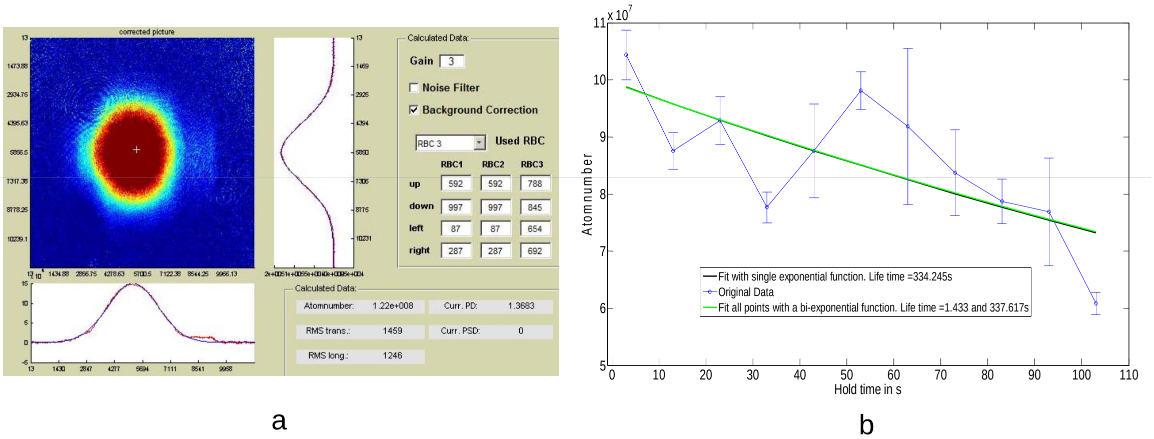

Fig. 3.6 (a) Absorption image of the atom cloud trapped in the final superconducting trap with 2×10^8 atoms and (b) Lifetime measurement of the atom cloud.

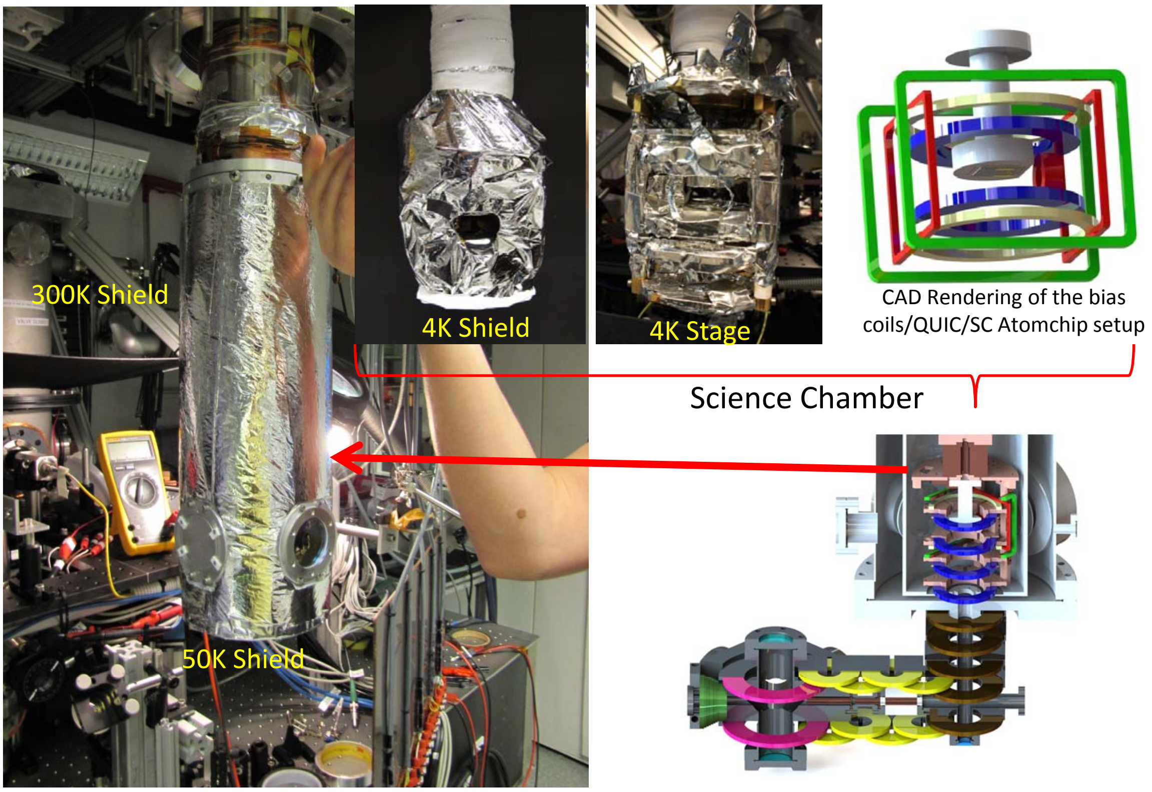

Fig. 3.7 The different layers of the Upper Chamber.

birefringence at cryogenic temperatures [94]. Within the 50 K Al shield lies the 4 K stage. It is mainly composed of a cage system that holds the final four superconducting transport coils and all critical components needed for the superconducting atomchip.

3.4.1 Science Chamber

The 4 K stage also known as "Science Chamber" is the most critical part of the setup. It holds the final superconducting chip mounting. The mounting is made of quartz to provide the best cryogenic thermal conduction; it has zero electrical conductance at cryogenic temperatures. It also has a very low dielectric coefficient for microwave frequencies which makes it ideal for superconducting microwave resonators. The uinset on the upper right of figure 3.7 shows different bits and pieces of the Science chamber. Currently, the 4 K shield is 3D printed and covered with layers of Mylar foil similar to the 50 K shield [109, 112].

The first generation superconducting atomchip is structured from niobium on a sapphire substrate. The niobium film is 500 nm thick. It forms a Z-trap with a wire-width of 200 µm and and a Z-length of 2.2 mm. In order to supply current to the atomchip, several Aluminum bonds (up to forty) are used from the niobium contact pads towards a commercial HTc YBCO wire (SuperPower^{Inc}). The SuperPower YBCO wire is made in such a way that it has a copper layer just above YBCO which makes soldering straight-forward. Further details on the superconducting properties and atomchip designs are discussed in chapter 5.

The Science chamber also houses several bias field coils for axes x-Ioffe, y-vertical, and z-imaging. The bias coils are all superconducting and made of the same commercial Nb wires as the final transport coils. They can produce 55.9 G/A, 261.0 G/A, and 127.3 G/A for the x, y, and z directions, respectively. An extra Ioffe coil is added in order to convert the final superconducting quadruple trap into a superconducting quadrupole-Ioffe trap [91].

3.4.2 Wire anchoring over various temperature stages

One of the most difficult milestones when bringing transport current into the cryostat is to avoid ohmic heating and bringing external heat from the 300 K environment. The original wiring construction composed of bringing 3 m long copper wires of 0.5 mm diameter directly to the 4 K stage [102]. From then on, the copper wires soldered to niobium wires inside a copper tube filled with solder. This method limited the critical current of the system to about 1.5 A. It also proved to be unreliable over several rebuilding operations. Exceeding the system critical current burnt the niobium wire right after the copper tube junction.

Increasing the length of copper wires decreases the thermal conduction from the room temperature environment to the 4 K environment. However, as previously discussed, this is not enough. In order to fully isolate the the the 4 K environment, a wiring scheme recipe was developed over several trial and error attempts. This allowed continuous application of 3.5 A indefinitely without heating more than 0.2 K. The recipes goes as follows:

- Use 0.4 mm diameter Copper wires, l =3.8 m
- Step 1: Anchor for 2 rounds without contacting the surface of the 50 K stage (about 50 to 60 cm of the wire).
- Step 2: Anchor for 4 rounds with good thermal contact.
- Step 3: Anchor without good contact for 2 to 3 rounds around the 20 K stage (about 20 to 30 cm of the wire)
- Step 4: Anchor with good contact for 3 to 4 rounds (≈50 cm)
- Step 5: Use HTc YBCO flat wires to transition from 20 K stage to the 4 K.

The steps above are illustrated in figure figure 3.8. From the last point with the YBCO wires, direct soldering to any niobium wire/coil can be done while making sure 1 to 3 cm of the wire after the HTc YBCO is properly anchored to the cold surface. Following these procedures always provided the same results. The only limiting factor for the current is where the copper wires are not anchored which is right at the feed-through going to the cold stages. At this point, it is nearly impossible for the wires to have thermal contact for heat dissipation to any surface. If the current exceeds 3.5 A, the system usually fails at this point. Higher current should be possible with a slightly thicker wire gauge and using an appropriate greater length.

3.4.3 Alternative Optical Pumping

Optical pumping to the $|F = 2, m_F = 2\rangle$ strongest low-field seeking ground involves applying the appropriate σ_+ polarized beam (beam 1c in figure 3.3) and a quantization field along the beam direction. The atoms will eventually become dark to the beam and all be in the $|F = 2, m_F = 2\rangle$ ground state. For cavity Quantum Electrodynamics Dynamics (cQED) applications as discussed in [59], the clock state microwave transition between the $F = 1$ to $F = 2$, $^5S_{1/2}$ ground state is used which is typically 6.83 GHz. This is from the $|F = 1, m_F = -1\rangle$ to the $|F = 2, m_F = 1\rangle$ through a virtual transition through $|F = 2, m_F = 0\rangle$ via a Raman process with an extra rf photon. In order to

Fig. 3.8 Wiring scheme from room temperature to the 4 K environment. The images show all the steps discussed for isolating and minimizing heat transport from the room temperature environment. In steps 1 and 3, plastic spacers are used to prevent thermal contact with the cold surface.

conduct cQED experiments, the atoms have to be prepared in the $|F=1, m_F=-1\rangle$ ground state rather than the $|F=2, m_F=2\rangle$.

The easiest method to implement this in the experiment without further additional optics is by slightly modifying the experimental cycle. By switching off the the repumper (beam 2a) a few 10 µs earlier than the main cooling (beam 1b) during the optical molasses phase (typically ∼10 µs), all the atoms will eventually fall off the cooling cycle into the $F=1$ ground state. This will bring the atoms into the the entire $F=1$

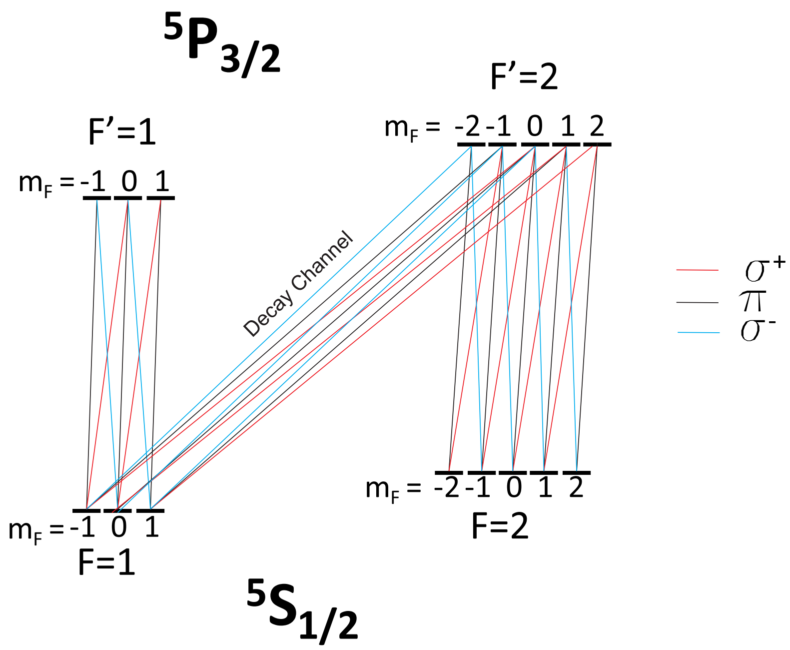

Fig. 3.9 The optical pumping scheme for various involving the $F = 1,2$ ground state to the $F' = 1,2$. The blue, black and red lines, correspond to σ^-,π, and σ^+ polarization. To see the full ^{87}Rb D2 line transition strengths for various all polarizations, see appendix A.

Zeeman manifold. Although the majority of the atoms will be lost, there will already be a fraction of the atoms in the $|F = 1, m_F = -1\rangle$.

Figure 3.9 shows the energy level scheme transition selection rules for the ground states of ^{87}Rb and the two excited states $F' = 1,2$. To pump the atoms into the $|F = 2, m_F = 2\rangle$ state would involve a σ^+ polarized beam on the $F = 2$ to $F' = 2$ line (beam 1c). The atoms will climb up and down the $F = 2$ to $F' = 2$ ladder and eventually end up in the dark state, $|F = 2, m_F = 2\rangle$. To pump the atoms into the $|F = 1, m_F = -1\rangle$ state will require and extra σ^- polarized beam along the $F = 1$ to $F' = 1$ line (beam 2b) and the original optical pumping beam (beam 1c) $F = 2$ to $F' = 2$ but σ^- polarized. This will bring them down to the decay channel towards $F = 1$.

The required beams for the alternative repumping into the $|F = 1, m_F = -1\rangle$ state can be taken off from the existing beams from the original laser setup in figure 3.4. However, building up extra optics would interfere with the experiment during operation. Therefore, a new laser setup based on the designs on [110] was constructed. Figure B.4a (See Appendix) shows the optical setup or the alternative rempumping beam. The setup contains two AOMs tuned to +78 MHz and −78 MHz, respectively. The positive

AOM output can be used as a spare beam for the experiment in case of emergency. Figure B.4b (See Appendix) is the setup for the other required optical pump beam. The laser locking scheme and the chosen locking crossovers are exactly the same as the existing DFB and ECDL setup for the repumper and reference master laser [110]. Both laser setups are built on portable bread-boards. Each bread-board is housed in a solid wooden box that is easily movable when necessary. An audio-grade sound absorbing and reflecting foam is placed on every exposed external wall of the wooden box to shield the setup from external acoustic noise. The output beams can be easily taken out by an optical fiber and brought to any location.

3.4.4 Cryo-imaging setup

The imaging setup in the cryogenic environment into the science chamber is also shown in figure 3.4. Imaging both in the traverse (main) and longitudinal (Ioffe) direction is done simultaneously using an ImagingSource DMK 21BU04 USB and Pixelfly PCO270XD cameras. Each camera is connected to a separate PC with the appropriate data acquisition (DAQ) software where absorption images are stored. Figure 3.10a shows the raw reflection microscopy image of the atomchip used. Figure 3.10b shows the absorption image of ultracold ^{87}Rb atoms trapped on the atomchip. The distance between the atom clouds is the twice the distance of the atom cloud to the chip [111].

The chosen objective lenses for both directions is a f =15 cm, 5 cm diameter lens. This gives enough space to have to atoms directly at the focal point while having enough space for the different layers (eq. 300 K shield, 50 K shield). The focusing lens is placed as close as possible to the objective lens in order to capture most of the parallel rays. This also ensures that if in case the objective lenses is slight further away from the atoms, less diverging beams escape the optical system. For the main imaging direction, a focusing lens of f =30 cm, 5 cm diameter is chosen. This gives an effective magnification of about 2.0×. To focus the optical system, the camera is moved along the imaging axis through a Thorlabs rail system until a sharp central Z-wire image is obtained as shown in figure 3.10a. The leads of the Z wire are used as a reference for focusing. The length of the central Z is used to calibrate the pixels of the camera since the length is exactly 2.2 mm. This gives an overall imaging resolution in the object space of 2.98 µm per pixel. With the 1392×1020 PCO camera resolution, this will provide a visible space in the object plane of 4.1 mm×3.0 mm which is more than enough to see the entire QUIC trap in one picture. In case imaging the original quadrupole trap after transport is desired, both cameras are mounted on an x-y-z

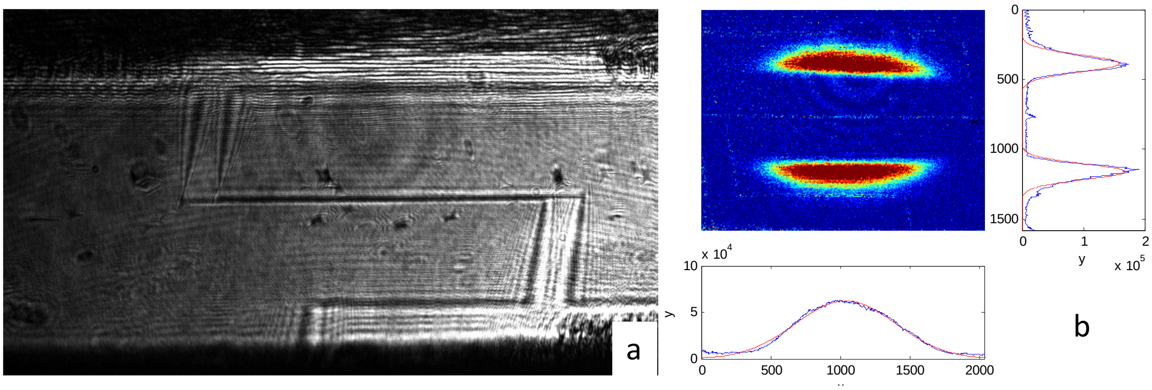

Fig. 3.10 Reflection microscopy of the atomchip chip used (a) and absorption image showing the atom cloud relfection (b).

translation stage which allows the camera to be fine-tuned in order to follow the QUIC trap formation since the QUIC trap moves about 6 mm from the initial quadrupole towards the Ioffe coil (See next chapter). It is also possible to reduce the effective focal length of the focusing lens by adding an extra f =10 cm lens. This produces a focusing lens of about f =9 cm which gives an effective magnification of 0.6×. This allows imaging both the quadruple trap and QUIC trap without further camera translation since they both traps fit in one image.

The Ioffe imaging axis is used mainly to track the movement of the QUIC trap along the x-z plane. This is very important for reloading into the superconducting atomchip which will be discussed in the next chapters. In this axis, a focusing lens that creates a magnification of 0.7× is chosen. Figure 4.1 from the next chapter shows a better visualization of the the different imaging axes. Since the the purpose of the axis is for tracking the atoms, calibration is not necessary. With this, atom number measurements from this axis is not reliable. However, reliable lifetime decay measurements can still be performed.

3.5 Further experimental details

3.5.1 Control

The entire experiment requires a plethora of controls, both analog and digital. We use an Adwin-PRO T100[3] control CPU. The system includes analog and digital cards that

[3]It is also important to note that the Adwin system produces noise from 800 kHz and multiples of this which is recently discovered will be discussed in [113]. This is also confirmed by the manufacturer

provide 32 analog channels and 64 digital channels [103]. It can provide a minimum of 20 µs time resolution, though, 25 µs is used and is more than enough in the experiment. The analog and digital channels are sent through home-built isolation amplifiers that isolate the signals from the external ground and as well as external noise sources. To communicate with the Adwin CPU, a separate PC is used that is isolated from the internet[4]. An in-house Matlab implementation through ADbasic is used with several applied modifications specific to our experiment for the magnetic transport and other special sequences in the Science Chamber [102, 103].

3.5.2 Current Sources

The experiment involves several electric currents sources. For high currents, Delta-Elektronika SM3000 series 30 V/200 A and 30 V/300 A power supplies are used. These provide currents up to 300 A to all normal conducting coils and can be controlled with an analog signal from Adwin. For switching, a home-built MOSFET network attached on copper structures with a specialized demutiplexing circuit is used. The bipolar operation of the vertical transport coils is mediated by an H-bridge MOSFET circuit construction. From the upper chamber with the cryostat onwards, everything carrying current is superconducting. The current sources (10 V/2 A) and electronics switches used are home-built electronics design for normal conducting devices with low resistance. These are the same electronics for normal conducting atomchip experiments used in [27, 114] and other related work. They work very well for the superconducting section of the magnetic transport and everything else in the Science chamber. In some cases, particularly the superconducting microstructure forming the Z, the resistance only exists on the normal conducting wires coming into the chamber. This is too low for current source to operate with good stability. This is remedied by adding an external power resistor of 1 Ω to 10 Ω. All the electronics mentioned here are discussed in great detail in [102, 93, 109]. See also Appendix B for more details.

to be caused by the CPU processor. Most experiments including ours have not been affected by this since most other critical devices are further filtered. In the future, a low pass filter can easily circumvent this problem.

[4] Frequent Windows update may interfere with the experimental cycle. Isolation from the internet also prevents infection from viruses.

3.5.3 Rf Sources and the rf/microwave setup towards the 4 K stage

Three rf sources are used for rf evaporative cooling. These are namely an SRS DS345 and two Agilents, 33220A rf sources. There is one rf/microwave feedthrough with four SMA inputs installed on the external 300 K chamber. They are brought down by rf/microwave coaxial kapton cables down to the 50 K stage where they are thermally anchored through attenuators (1 dB and 3 dB). From this point the signal is brought down by bent-to-fit steel coaxial cables 940 mm long to reduce heat transport similar to section 3.4.2. From the the 4 K stage, they are again connected to attenuators (1 dB and 3 dB) for thermal anchoring. The entire rf/microwave setup is shown in collage form on figure 3.11. Depending on the application, rf and/or microwaves signals can be brought down to the Science Chamber either with a superconducting microwave resonator, 3D cavity or a simple antenna [115, 72].

In the current setup, the signal lines are used to bring down rf signals where an improvised coil antenna using niobium wires is used. This is shown in figure 3.11. This produces an rf field perpendicular (y-axis) to the quantization axis[5] of the QUIC trap and at the same time the Atomchip Z trap. Another similar rf coil is also installed although not visible right on top of the V8 coil. The coils are wrapped with teflon to shield them from thermal radiation since the wires are superconducting. They were both found to work equally well for addressing the atoms. It is also important to note that as far as possible, aluminum tape close to the rf antenna should be avoided. This was found to dramatically attenuate the emitted rf signal in the previous rebuild iterations.

3.5.4 Acquisition and Analysis

The data analysis software used is the shared matlab-based program from the Schmiedmayer group with programming modifications depending on the the application [116, 28]. As discussed in section 3.4.4, each camera axis has a dedicated PC for data acquisition and storage. A separate PC has access to both PCs' data. A multi-purpose matlab script was written to analyze data from lifetime, trapping frequency, rf cooling, and so on. The separate PCs allow measurement and analysis to be done simultaneously without interrupting scan measurements.

The absorption imaging performed in the experiment is similar to most absorption imaging schemes used for the ^{87}Rb D2 line. Three images are captured, namely a dark

[5] The Ioffe field of the Z and QUIC traps point along the z-axis.

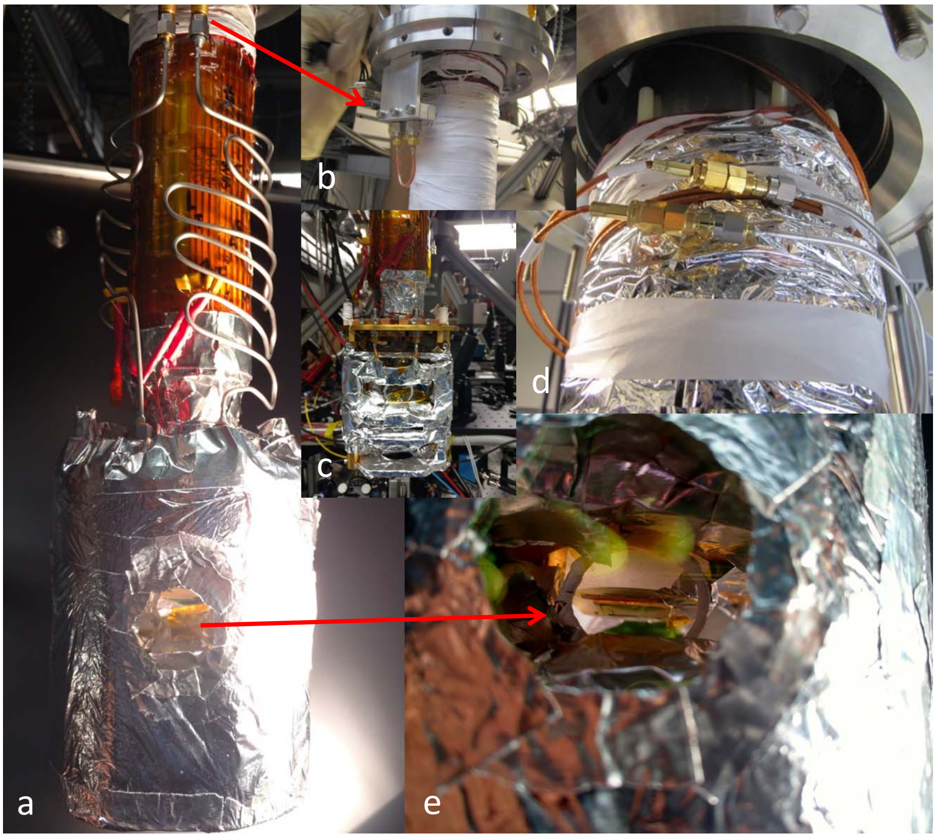

Fig. 3.11 Rf/microwave cryo setup towards the Science chamber or 4 K cage Collage. (a) shows the coaxial cables from the 50 K stage to the 4 K stage. It also shows the latest iteration of a new 3D printed 4 K stage wrapped with various layers of aluminized mylar foil. (b) shows the attenuator mount for the 50 K stage. (c) shows the the 4 K stage without the 3D printed shield. (d) shows the junction from the 50 K stage with the attenuators to a flexible kapton rf/microwave cables to the external feedthrough. (e) shows the rf antenna used (30 turns). It is made from the same niobium wire as all the superconducting coils.

background to measure dark noise, an atom cloud image shadow with the imaging beam pulse, and a raw imaging beam pulse without atoms. With these images and the camera calibration, the atom number of the cloud can be calculated [93, 117, 102]. Gaussian fits are applied to the absorption images to measure size, position, and location. For reflection imaging on the atomchip as shown in figure 3.10, a double Gaussian fit is used to measure the distance between the two clouds which is $2d$ where d is the atom cloud's distance to the chip [111] .

3.5.5 Stability and Diagnosis

The experiment involves many devices, signals, parameters, flowing currents, and temperature critical systems. This makes the experiment a massive diagnosing nightmare in case a particular device or channel goes wrong. It can take up to a day or week to diagnose a simple problem such as a broken MOSFET or fuse. In this respect, it is very important to monitor every device, current, signal and other critical systems as much detail as possible.

Each current going into a coil or into the cryostat is measured with a current sensing element. For the normal conducting coils, this is done directly inside the switch box. For the superconducting currents, this is done inside a home-built breakout box where every current that has to be brought into the chamber can be internally rewired. From the breakout box, the currents then go to the chamber through current feed-throughs. The current sensors are monitored through a Labview program where the currents of every coil or device in the experiment are monitored in real time [109].

The pressure gauge in the cryostat chamber between the 300 K and 50 K shield and the temperature sensors inside the cryostat are also monitored through a Labview program via direct USB-GPIB connection to their respectively control devices [102]. The power supply of the Rubidium dispenser is also remote-controlled via Labview. This allows the possibility of pulsing the dispenser if necessary. In case of sudden cryo shutdown, the Labview temperature program couples to another program that automatically stops the Adwin computer to prevent damage to the setup. A webcam observing the laser spectroscopy oscilloscopes also provides information on whether one of the lasers have gone out of lock.

There are also bi-metal sensors that trigger at 65 °C that are attached to every water-cooled normal conducting coil in case of water flow or water cooling failure [103, 102]. These sensors are all connected in series to a circuit that shut down the high-voltage source of the Delta-Elektronika power supplies in case one coil heats up beyond 65 °C.

Part II

From the Quadrupole-Ioffe Trap into a Superconducting Atomchip

Chapter 4

Superconducting Quadruple-Ioffe Configuration Trap

From the previous chapter, the final stage of the magnetic transport traps the atoms at the last superconducting quadrupole coil pair. These coils can be converted into a Quadrupole-Ioffe Configuration (QUIC) trap [118]. This is done with an additional smaller coil perpendicular to the quadrupole axis as shown on figure 4.1. The smaller coil geometry with respect to the quadrupole coils creates an inhomogenous field that can lift the trap bottom as shown on figure 4.2a. This effectively plugs the zero trap bottom of the quadrupole and converts the trap into an Ioffe-Pritchard type trap with a harmonic trap bottom [119]. The non-zero trap bottom prevents colder atoms from getting kicked out of the trap due to Majorana losses and allows the condensation into a BEC. Figure 4.2b and 4.2c show the trapping frequency, trap bottom, and trap position characteristics of the QUIC trap for an increasing Ioffe current I_{Ioffe}. Figure 4.2d, 4.2e, and 4.2f show the actual experimental measurements of the QUIC trap formation. These correspond directly to the calculation in figure 4.2a. The position of the Ioffe coil towards the center of the original quadrupole trap determines where the QUIC trap forms and at which current. If the Ioffe coil is closer to the quadrupole center, it requires lesser I_{Ioffe} while a trap further away would require more current [118, 103]. Ideally, a QUIC trap formation close to to the location of the atomchip Z trap is desired. This is about 6.2 mm from the central minima formed by the initial quadrupole trap (Geometric center of the blue coils in figure 4.1). The exact location of the Ioffe coil can be calculated in order to produce a QUIC trap at 6.2 mm. This corresponds to a ratio of $\frac{I_{Ioffe}}{I_{quad}} = \frac{630\,\mathrm{mA}}{700\,\mathrm{mA}} = 0.90$. Note that this ratio is only true for the very first installation position Ioffe coil in the experiment since moving the Ioffe coil during a repair or maintenance operation changes this ratio. This ratio is currently

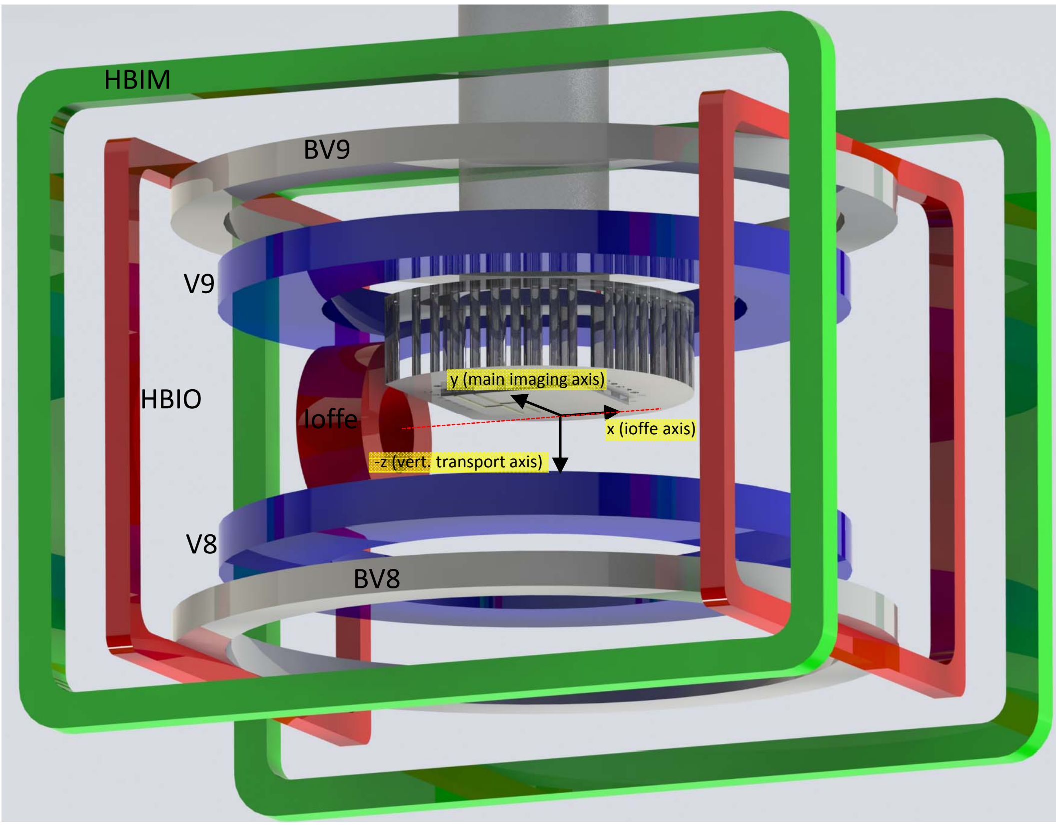

Fig. 4.1 3D CAD rendering of the Science chamber showing all the relevant coils and coil pairs. The quadrupole-Ioffe trap (QUIC) is formed by coils V8 (3000 turns, top blue coil), V9 (3000 turns, bottom blue coil) and Ioffe (1800 turns, red coil). The coil pair BV8 and BV9 (1240, gray coils) can be between switched either in Helmholtz and anti-Helmhotz configuration using solid state relays. Each coil is made from a commercial Nb-Ti filament wire. The coil pairs HBIM (820 turns each, green coils,) and HBIO (421 turns each,red coils) are internally series connected in Helmholtz configuration. The atomchip mounting is made of quartz, shown here just above the QUIC trap. Further details of the mountings and engineering are discussed in great detail in [109, 102].

approximately 0.93 [112]. From the calculations, a trap bottom of about 0.5 G should give a very high trapping frequency around 400 Hz. However, experimental trap bottom values within this range were found to create an unstable QUIC trap. Trap bottoms within the range of 1 G to 5 G provided a stable trap. At higher values, the thermal Boltzmann tail of the atoms wouldn't be addressable with an rf field since the rf generator used for addressing the atoms only goes up to 30 MHz.

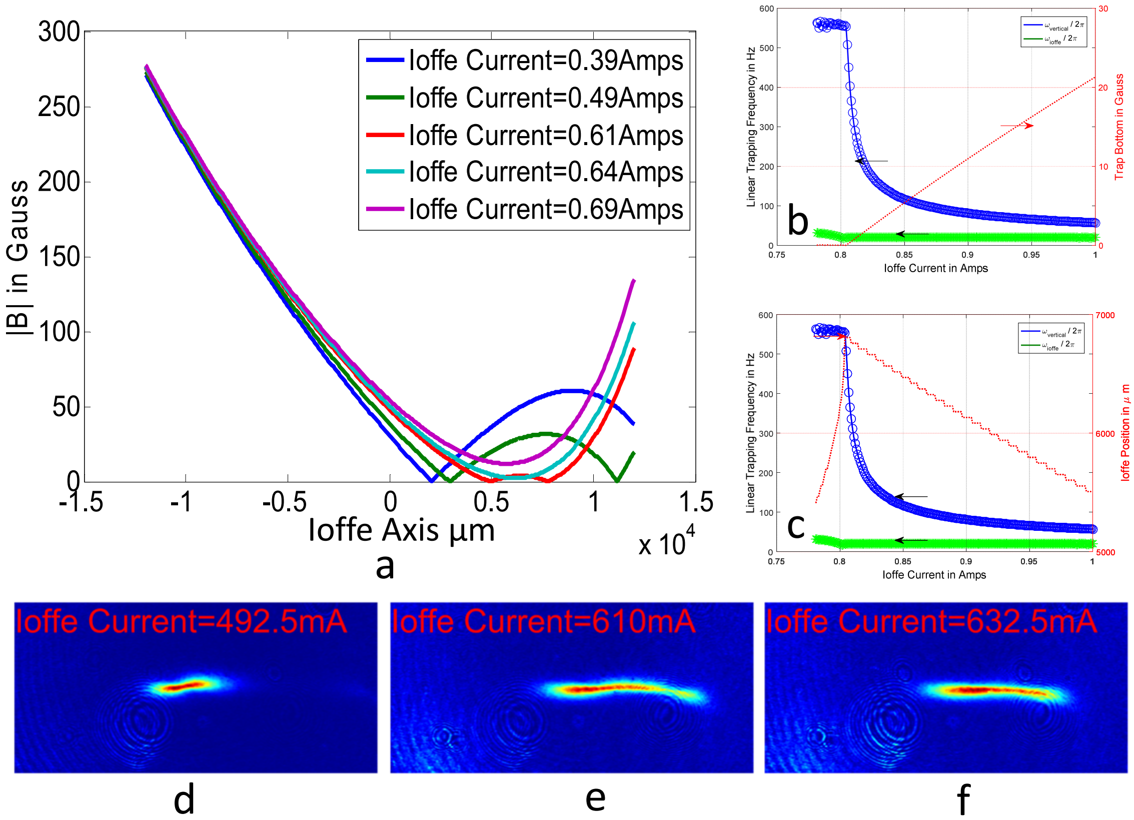

Fig. 4.2 (a) shows the potential along the x (Ioffe) axis of the QUIC trap formation as the I_{Ioffe} current increases for a I_{quad} of 700 mA. (b) and (c) show the trapping frequency characteristics of the QUIC trap compared to the trap bottom and trap position, respectively. Since these magnetostatic calculations are linear, the weak direction of the QUIC trap stays more or less constant around 20.1 Hz. The properties in (b) and (c) are calculated for $I_{quad} = 1$ A. For any other current, the simulation can be scaled up or down depending on the actual experimental parameters. (d), (e), and (f) show experimental absoroption images of the QUIC trap formation corresponding to the simulation in (a).

4.1 Electronics configuration for a series QUIC trap

The QUIC trap requires three coils to be operated at the same time. If these three coils were to be supplied by independent current sources, relative fluctuations between the sources would shake the trap unpredictably. If the QUIC trap were operated at the border between the formation of the harmonic trap bottom and the merging of two quadrupole minima, this would make the trap very unstable. The trap position would be fluctuating in space and cause heating in the atom cloud. The easiest work-around against relative fluctuations between the current sources is to force every current source to fluctuate synchronously by connecting all QUIC coils in series. The trap position will remain constant and any small fluctuations in the current will be translated into overall trapping gradient fluctuations.

Converting the last superconducting transport coils into series with an Ioffe coil can be a very tricky task. In principle, one can connect them in series from the start. However, the magnetic transport requires independent current control of each coil. Initially, the series connection of each coil was planned to be achieved using a power splitter built by our electronics workshop (circa 2011). Unfortunately, this device proved to be extremely non-linear and unpredictable and never really worked properly (See Appendix B). The best way to convert the final superconducting quadrupole trap into series with the Ioffe coil is to load the atoms into a temporary quadrupole trap so that all three coils can be externally connected in series. This can be either be done mechanically or electronically with solid-state relays. The circuit diagram to achieve this is shown on figure 4.3. Figure 4.3b shows the currrent sequence to connect all three coils into series. The buffer coils require more current to maintain trapping gradient of the intial quadrupole trap. If the coils are aligned properly, the atoms do not see the change in potential. With this, the reloading into the series QUIC trap using this "Buffer Trap Method" works very well without any noticeable atom loss.

As mentioned in the last section, in order to have an ideal QUIC trap with the appropriate trap bottom, the Ioffe coil position has to be fine tuned in order to create a QUIC trap with the appropriate trap position and trap bottom. This was done over repetitive cooling-warming-up-maintaince cycles. If the necessary, the trap bottom can be fine tuned with the HBIO coil-pair in order to obtain a desired trap bottom and trap frequencies according to figure 4.2b and 4.2c.

4.2 Time of Flight (TOF) imaging in the QUIC trap

The three coils forming the QUIC trap have a measured inductance of about 1 H using an LCR bridge at 1 kHz. This extremely high inductance makes it nearly impossible to switch off fast enough to do an appropriate time-of-flight (TOF) imaging scan. Atoms should feel the magnetic trap disappearing immediately. This is possible if the magnetic trap is switched off within a few 100 µs or less. This is a common problem for magnetic traps using coils. Most other experiments remedy their switch-off by designing specific circuits that rapidly remove the magnetic energy stored in the coils. In our QUIC trap, however, attempting to design a circuit to have sub millisecond switching for 1 H

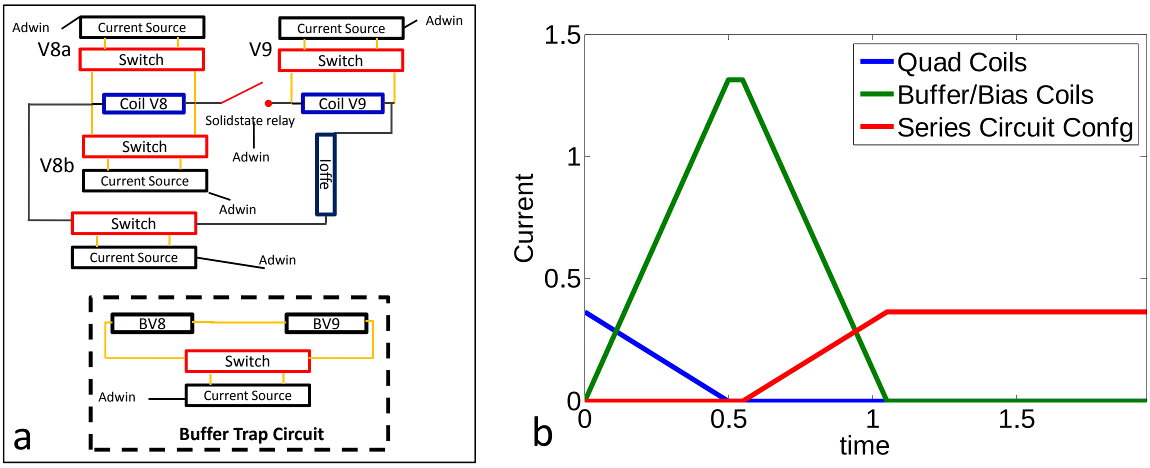

Fig. 4.3 (a) shows the circuit diagram used to connect V8, V9 and Ioffe in series and the independent buffer trap circuit. (b) shows the current sequence to for the reloading into the series QUIC trap.

inductance would be futile. Using the best available in-house electronics coupled with diodes, the lowest possible switch-off time achieved is 2.5 ms.

The main consequence of high inductance is inductance fields and eddy currents forming on nearby metal surfaces [102]. Figure 4.4a shows a TOF measurement in the QUIC trap. The fluctuating atom number during the first few milliseconds suggests that there are massive induction fields. These have been measured and studied in great detail in [102]. The fluctuations also change when different or additional devices are installed in the 4 K stage. Above 10 ms, the fluctuating fields subside. During the experiment's best state, about 2.5×10^8 atoms are in the QUIC trap of about 367 µK. Figure 4.4b shows the RMS widths of the atom cloud versus TOF^2 . It is still not clear why there is a difference in temperature between both axes.

It is also not clear whether the fluctuating fields are homogeneous or inhomogeneous. A homogeneous field would just detune the absorption imaging which was the conclusion of [102]. However, by observing the TOF snapshots, the cloud moves violently during the first 10 ms (See Appendix B for the full TOF movie.). This means that the fluctuating field is very inhomogeneous and it appears as though the quadrupolar nature of the QUIC trap is undergoing a damped oscillation. This disturbance would warm the atoms and make the measured temperature appear greater than the real cloud temperature. This also makes it nearly impossible to image a BEC in this QUIC trap since it will be heated up immediately by the violent field fluctuations.

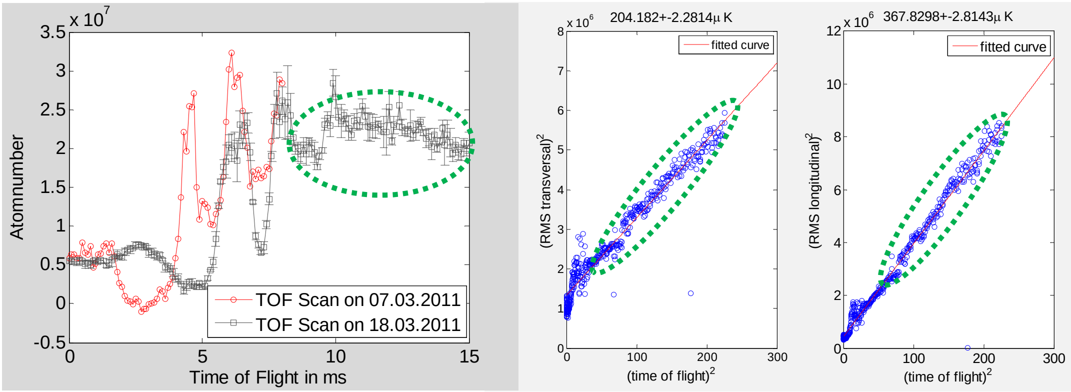

Fig. 4.4 (a) shows the atom number versus time of flight. At TOF> 10 ms, the violent fields subside and a proper atom number measurement can be done. (b) shows the RMS widths of the atom cloud in the QUIC trap versus TOF^2. There is difference in temperature in both axes, 204 µK and 369 µK.

4.3 Rf evaporative cooling in the QUIC trap

The atom cloud trapped in the QUIC trap can be addressed with an rf field [120]. Since the magnetic fields in our magnetic traps are in the low-field linear Zeeman regime, the atoms, through the rf field, can be brought out of the $|F=2, m_F=2\rangle$ into the entire m_F manifold and thus be brought out of the magnetic trap. With this, atoms can be cooled down evaporatively through the slow removal of warmer atoms while giving the cloud time to thermalize to a colder temperature. This is done with an rf knife ramp from a high to low frequency addressing the warmest atoms towards colder atoms occupying close to the trap bottom. Depending on the cloud temperature, the atoms will be distributed around the magnetic trap according to the Boltzmann distribution [11]. Figure 4.5a shows a trap-bottom spectroscopy which shows how far the Boltzmann tail of the warmest atoms reach. Above 18 MHz, there is no observable loss in atom number which is a good indicator for the starting frequency of the rf knife [95]. Figures 4.5b and 4.5c show the peak density versus rf cooling time measurements for a 30 MHz to 5 MHz and 18 MHz to 5 MHz ramp, respectively. Figures 4.5b and 4.5c show the corresponding absorption images. Despite initial predictions, the rf knife starting from 30 MHz creates the coldest and densest cloud. This indicates that there is a very long tail in the temperature distribution that is not visible with the trap bottom spectroscopy.

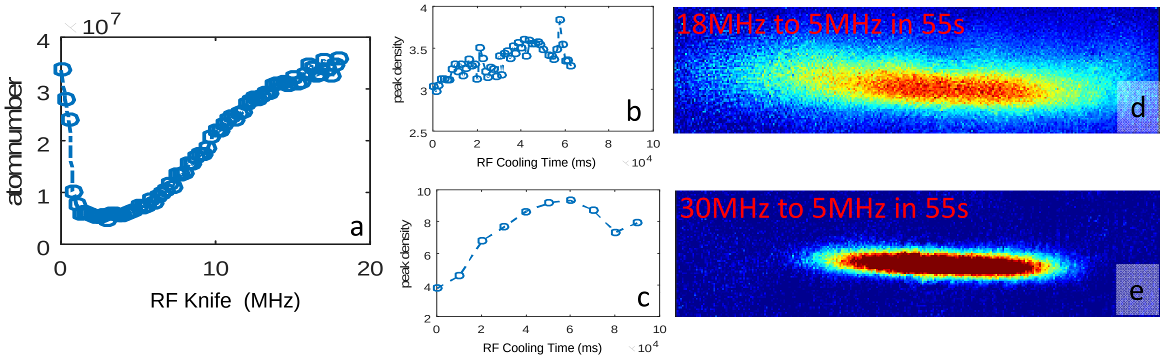

Fig. 4.5 Results for a 400 mA series current and ratio of $\frac{I_{Ioffe}}{I_{quad}} = 0.94$. Trap bottom spectroscopy with a constant rf knife is shown in (a). (b) and (d) show the results for rf cooling from 18 MHz to 5 MHz in 55 s while (c) and (d) show results the same measurement but starting from 30 MHz. This trap has measured trapping frequencies of 16.6 Hz and 166.7 Hz. See [112] for measurement details.

4.4 Heating rate and condensation-attempts in the QUIC trap

The next step is to attempt rf cooling towards condensation in the QUIC trap. Before this, it is important to characterize the heating rate of the system. The heating rate will determine whether the trap will be stable enough for condensation into a BEC. The QUIC trap is widely used for loading into other harmonic traps whether magnetic or optical [118]. It is also an ideal trap for creating an initial BEC.

A summary of rf cooling attempts is shown on Figure 4.6. Since the trapping frequencies can be measured or calculated, the atom cloud temperature can be estimated from the atom cloud widths. Figures 4.6a, 4.6b, and 4.6c shows the the RMS widths of the atom cloud and atom number versus the ending rf frequency of the rf knife. Starting from an estimated temperature of 39 µK down to a minimum of 800 nK is achieved with barely 10^5 atoms. Colder atomclouds down to about 400 nK are also possible, however, the cloud size the reaches the limit of the imaging system. As discussed in the last chapter, the imaging resolution in this axis is 2.98 µm/pixel. The estimated BEC size from section 2.2 for 10^4 atoms is about $2\,\mu m \times 30\,\mu m$ which is already too small for the imaging system. A BEC might have already been created but since TOF imaging is not possible in the QUIC trap, it has never been observed.

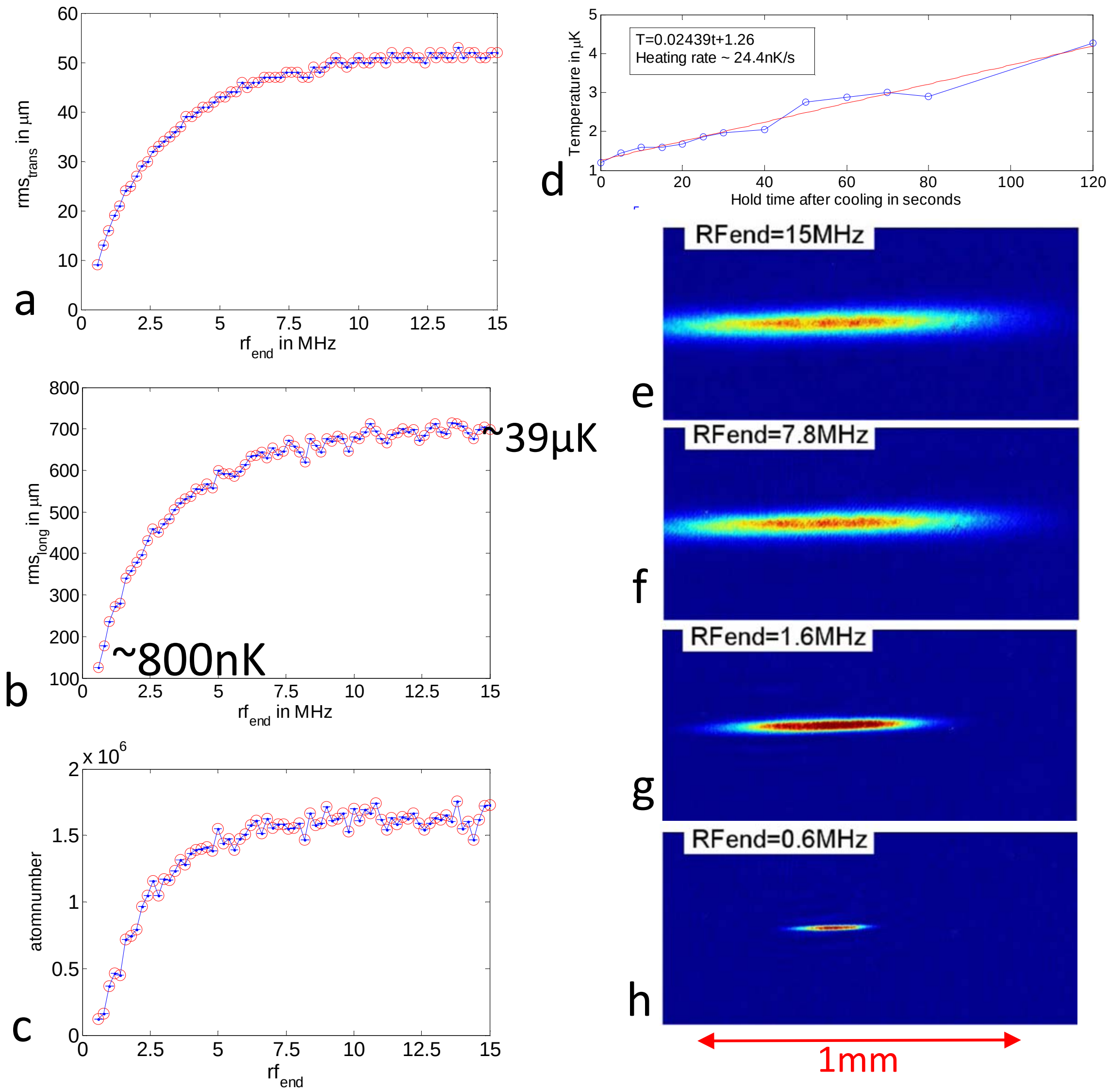

Fig. 4.6 Summary of condensation attempts in QUIC trap. The QUIC trap used has the same parameters as in figure 4.5. (a). (b) and (d) show the results for the in-situ QUIC trap widths and atom number versus rf cooling starting from 15 MHz to a scanned rf end. The cooling time for each point is optimized to obtain the best result. This is typically from 30 s to 90 s. The estimated starting temperature from in-situ widths and the QUIC trapping frequencies is about 39 µK. At an rf knife of 0.6 MHz, a minimum temperature of 800 nK (d) shows the heating rate plot of the QUIC trap which is 24.4 nK s^{-1}. (e)-(h) shows snapshots of the results of (a)-(c).

Chapter 5

Transfer into the Superconducting Atomchip

Unlike most of the atomchip experiments in the world, the atomchip in this experiment is very unique [108, 28, 27, 121]. Instead of normal conducting structures such as Gold, Copper, and Silver, the atomchip is structured from superconducting materials. In this experiment, these are niobium ($T_c \approx 9.2\,\mathrm{K}$) and Yttrium Barium Copper Oxide (YBCO, $T_c \approx 93\,\mathrm{K}$) which are both type-II superconductors. Despite the massive difference in their transport properties (to be discussed in later chapters), the same lithographic method for structuring the chip is applied [121, 122]. In this chapter, we will discuss the historical progress throughout this work on the efforts that led to the first superconducting atomchip trap in the group. Attempts towards a BEC on a superconducting atomchip will be discussed. And lastly, current distribution analysis comparing absorption images of the atom cloud and μHall microscopy measurements of the superconducting atomchip will be discussed as a prelude to the next part.

5.1 Atom trapping with wire structures

We will briefly review some important intuitive concepts of basic atomchip trapping technology, especially the basic principle in creating microtraps for low-field seeking neutral atoms around a current. The simplest case is with a current carrying infinitely thin wire. The wire creates a magnetic field $B_{wire} = \mu_o I/2\pi r$ with r as the distance to the wire and I being the transport current. The magnetic field vector rotates around the wire which is proportional to $\vec{di} \times \vec{dr}$ where $\vec{di}$ is the differential current vector and $\vec{dr}$ is the differential position vector. This is illustrated on figure 5.1a. For high-field seeking neutral atoms, this is essentially a sink trap much like planetary orbits around

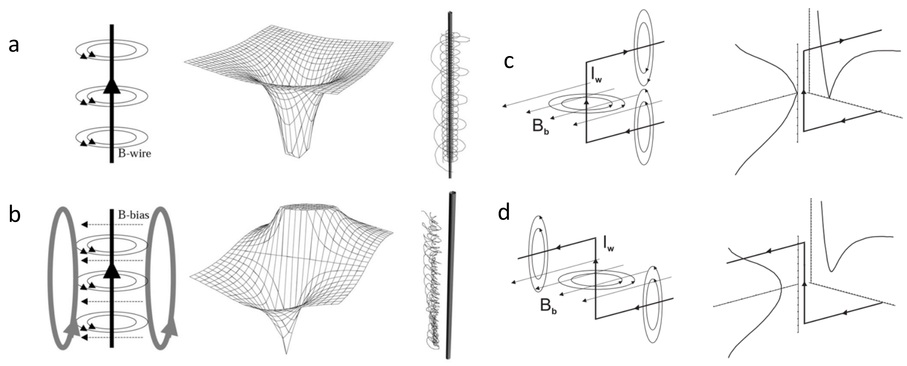

Fig. 5.1 Basic wire trapping geometries taken from [108]. (a) shows the magnetic field vector of a current carrying wire and its corresponding energy potential landscape. (b) shows the the same wire but with an added homogeneous bias field (eg. created by Helmholtz coils). Beside it is the potential landscape that shows a minimum forming above close to the wire where the field vectors cancel. (c) and (d) show two configurations that close can close the guided trap in (b), namely, the U-trap and the Z-trap.

the Sun as shown in the atomic trajectories beside the potential landscape. This trap is often called the Kepler guide. Applying an extra homogeneous magnetic field, B_{bias} perpendicular the transport direction, creates a trap minimum where the vectors of the homogeneous field and the field of the wire cancel out. The position of the trap minimum is then $r_{min} = \mu_o I/2\pi B_{bias}$. This is illustrated in figure 5.1b where low-field seeking atoms are guided beside the current carrying wire, hence called the side guide.

Note that the simple side guide trap is not closed in the current-transport direction. For practical applications, it is important to close this trap. This is done by bending the current-carrying wire in two ways, either in a U shape or in a Z shape as illustrated in figure 5.1c and figure 5.1d. Both traps produce a quadrupole-like trap rotated by 45° relative to the bias field direction. This is a very important feature to take note especially when loading atoms from a QUIC trap where there is no 45° quadrupole offset. The main difference between the U-trap and the Z-trap is with their trap bottom offset. The U-trap has a zero trap bottom whereas the Z-trap as a finite trap bottom that depends on the applied current and the length of the central closed trap. Note in the U-trap, the bends are made in such a way such that the current returns opposite to its original transport direction. Thus, the field vectors at the trap position, the Ioffe component (x-component) cancels out at the. In the Z-trap, the current of the bends move into the same transport direction. Therefore, there is a small ioffe component at the trap minimum. This inherent non-zero trap bottom can be lifted further with an

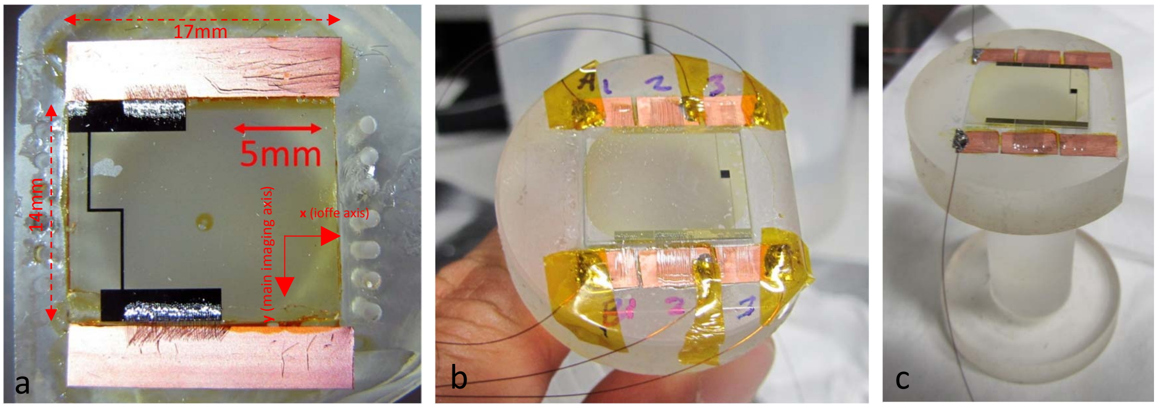

Fig. 5.2 Superconducting atomchip photos and the quartz mounting. (a) shows the very first atomchip used in the experiment. The sapphire substrate is 17 mm×14 mm in area. The Aluminum bonds going over the Nb contact pads towards the YBCO surface are visible. (b) shows a more elaborate YBCO atomchip with three Z structures using the same contacting technique. (c) shows a better view of the quartz mounting. See Appendix D for more detailed CAD drawings.

additional ioffe bias field which makes the Z-trap ideal for avoiding Majorana losses and for condensing into a BEC. The Z-trap is also an Ioffe-Pritchard type trap.

5.2 Superconducting Atomchip Designs

The first fabricated superconducting atomchip is made of structured niobium on a sapphire substrate. It is 500 nm thick and is made locally at the Austrian Institute of Technology. It has a measured T_c =9.2 K. Figure 5.2a shows a picture of the first fabricated atomchip. The wire is 200 µm wide with a Z-length of 2200 µm. It has a measured critical current of 2.1 A at 6 K and about 3.5 A at 4.2 K [109]. The Z-center is positioned exactly where the QUIC trap is predicted to form. The first fabricated superconducting atomchip is made of structured niobium on a sapphire substrate. It is 500 nm thick and has a measured $T_c = 9.2$ K.

The entire atomchip substrate is glued on a Quartz mounting using GE-varnish [102]. Contacting the niobium pads is not straightforward due to the thick oxide layer that forms above the material. The first unsuccessful attempt was done using niobium bonds directly. The first superconducting atomchip experiment [94] used a special superconducting alloy to solder directly on the niobium contact pad [123]. The alloy involved is commonly called Roses alloy, which is 50% bismuth, $25-28\%$ lead and $22-25\%$ tin, used mostly for industrial soldering purposes. Using Roses alloy along with ultrasonic solder works but was found to be too technically demanding

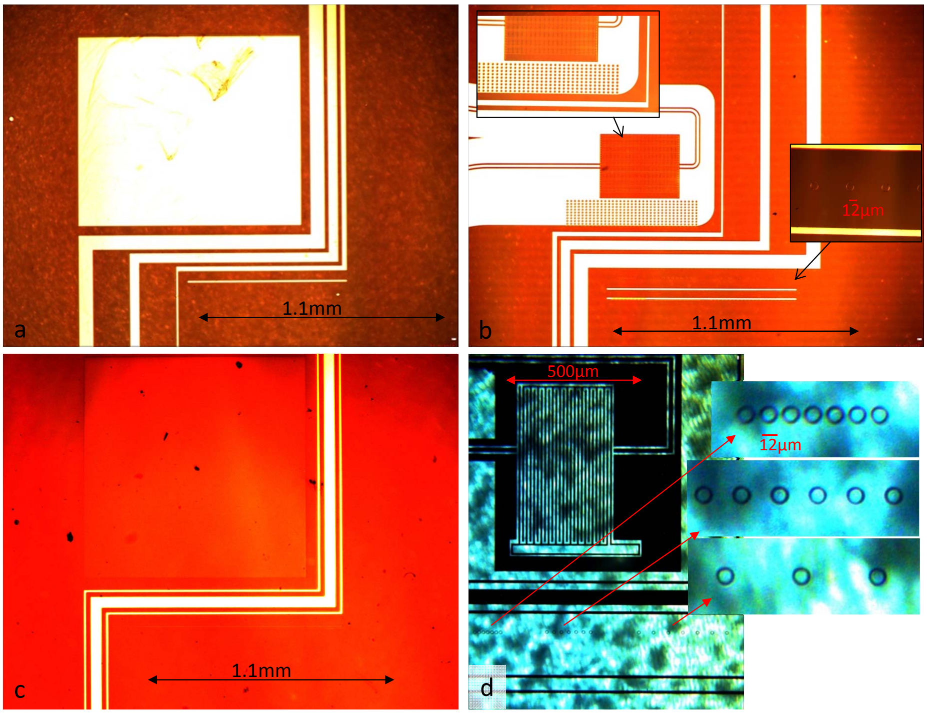

Fig. 5.3 Microscope photos of the fabricated superconducting atomchips. (a) and (b) are both microscope photos of niobium atomchips focusing on the Z-structures. These atomchips are fabricated in-house. (c) and (d) shows the YBCO atomchips structured by StarCryo where that latter is done with the microscope in transmission mode to see the bare YBCO structures without Gold. The film is produced by Ceraco which properties are as follow: 330 nm M-Type YBCO with 100 nm Gold and I_c of 10 µm A^{-1}. See Appendix D for detailed CAD drawings.

and required a lot of practice. The results were not reproducible and usually the critical current of the system was determined by the quality of the solder. The most reproducible method was to use Aluminum bonds. Aluminum bonds along with a proper bonding machine easily broke through the niobium oxide layer and provided enough reproducible contact strength. The Aluminum bonds are then bonded again to the same HTc YBCO used in section 3.4.2. With this, traditional soldering can be easily applied on the YBCO copper layer. This method is easily reproducible and systematic. To ensure maximum utilization of the critical current of the structure, up to forty Al bonds (or more) are made.

All niobium atomchips are structured in-house using a Heidelberg DWL laser writer to write on a positive resist, and reactive ion-etching is used for removing material. The laser writer allows structures down to 2 µm. Designs can be drawn with any computer animated drawing (CAD software eg. AUTOCAD). CAD designs have to be drawn in closed polygons. With this, almost any geometric structure is possible. Technologically, either with e-beam or traditional UV lithography, niobium can be structured down to 100 nm [124]. Many of the existing niobium or niobium compound technologies aim at producing traditional electronics as in CMOS in silicon using superconducting effects in the hopes of a dissipation-less circuit. If necessary, niobium can be structured much smaller than what is possible with available equipment.

Figures 5.3a and 5.3b show other fabricated atomchip geometries with niobium while figures 5.3c and 5.3d show similar designs fabricated on YBCO. The first design shown in figures 5.3a and 5.3c have three cascades of Z-structures, a 1 mm×1 mm rectangle and a thin rectangle on the other side. The 1 mm×1 mm rectangle is intended for probing lifetime enhancement in superconductors both in the Meissner or mixed state and can also be used as a remnant magnetization traps [81]. There is a slight variation on the Z-cascade on the YBCO version. It is designed symmetrically with rf-dressing in mind [125] whereas the niobium version is a simple cascade with reducing Z-lengths where the smallest Z-length is 0.5 mm long and 25 µm in wire-width. The second design is the same Z-cascade structure but with an lumped element resonator. The resonator is designed to a have resonance close to 6.83 GHz. The inductor strip of the resonator is 500 µm long, enough to accommodate the longitudinal extent of the atoms in the nearest Z-trap. On the other side opposite the resonator, several structures are fabricated. These include rings, a rectangular patch and a rectangular path with rings. These can be used for novel superconducting traps, including superconducting lattice traps, as discussed in chapter 8.

YBCO is a very unique high Tc superconductor ($T_c \approx$93 K). Unlike most elemental superconductors, YBCO is a ceramic above T_c and has a blackish color. Under a microscope in reflection mode, it is nearly invisible. This is illustrated in figure 5.3d. The YBCO Z-structures have a thin 100 nm gold layer. This protects the structure from burning-off in case the superconductor quenches. The YBCO film is structured by StarCryo and grown by Ceraco has a critical current property of 10 µm A^{-1}. The central Z-wire is 50 µm wide thus giving it an I_c of 5 A. The two rf Z-wires beside the central Z-wire are both 10 µm allowing I_c of 1 A.

5.3 Transfer from the QUIC trap into the superconducting atomchip

Going back to figure 4.1, the atomchip mounting has a 2 mm vertical offset relatively to the center of both quadrupole coils where the vertical part of the magnetic transport ends. This gives enough space for the atoms after magnetic transport and conversion into the QUIC trap. The very first method for loading the QUIC trap atoms into the superconducting Z-structure was first proposed in [102]. The proposed sequence is shown on figure 5.4a. The sequence involves ramping up the chip current and bias the subsequently ramping down the QUIC series current with the vertical field used to move the QUIC trap closer to the atomchip surface. This sequence never worked in experiment mainly because of the 45° offset between the QUIC trap and wire Z-trap. The trick is to account for the 45° offset. This can be done by applying an extra field opposite the bias field, B_{bias} needed to create the trap. The sequence shown in figure 5.4b was found to work very well for QUIC to chip loading after several magneto-static optimizations. With the QUIC trap on, I_{QUIC}, a vertical field, B_{vert} and a negative bias are applied. This brings the trap close to the chip surface and sideways in the direction of the bias field, as illustrated in steps A to B on the figure 5.4b. The next step from C to D involves the actual loading process. At this point, the chip current I_{chip} is ramped up while I_{QUIC} and B_{vert} both ramp to zero. B_{bias}, however, ramps up to the opposite polarity to create the chip trap. The side-ways movement compensates for the 45° offset between the two different traps. To illustrate and visualize the loading sequence, the magneto-static simulations are presented in figures 5.5 and 5.6. Since the trap minima starting from the QUIC to the chip trap swing around the wire trap, we have called this method the 'swing-by maneuver.'

The full loading process is too lengthy to fully illustrate, therefore only interesting events are shown. Figure 5.5 shows a 3D snapshot illustration at different points in figure 5.4. Despite the unstable iso-surface rending of Matlab, the QUIC minima can

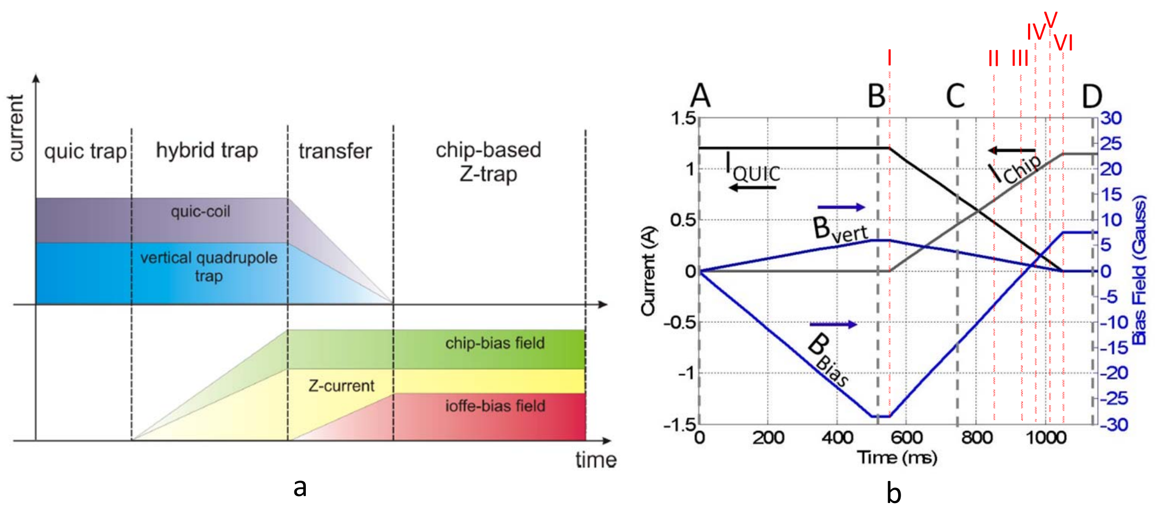

Fig. 5.4 (a) shows the original proposed loading sequence in [102] and (b) the sequence that works and is also the actual current sequence used in the experiment.

still be tracked with the x-y and x-z contour slices. The trap remains closed during the entire sequence which is best illustrated in the contour plots on figure 5.6 where the quadrupole axes are also depicted. It is through these illustrations that we can see

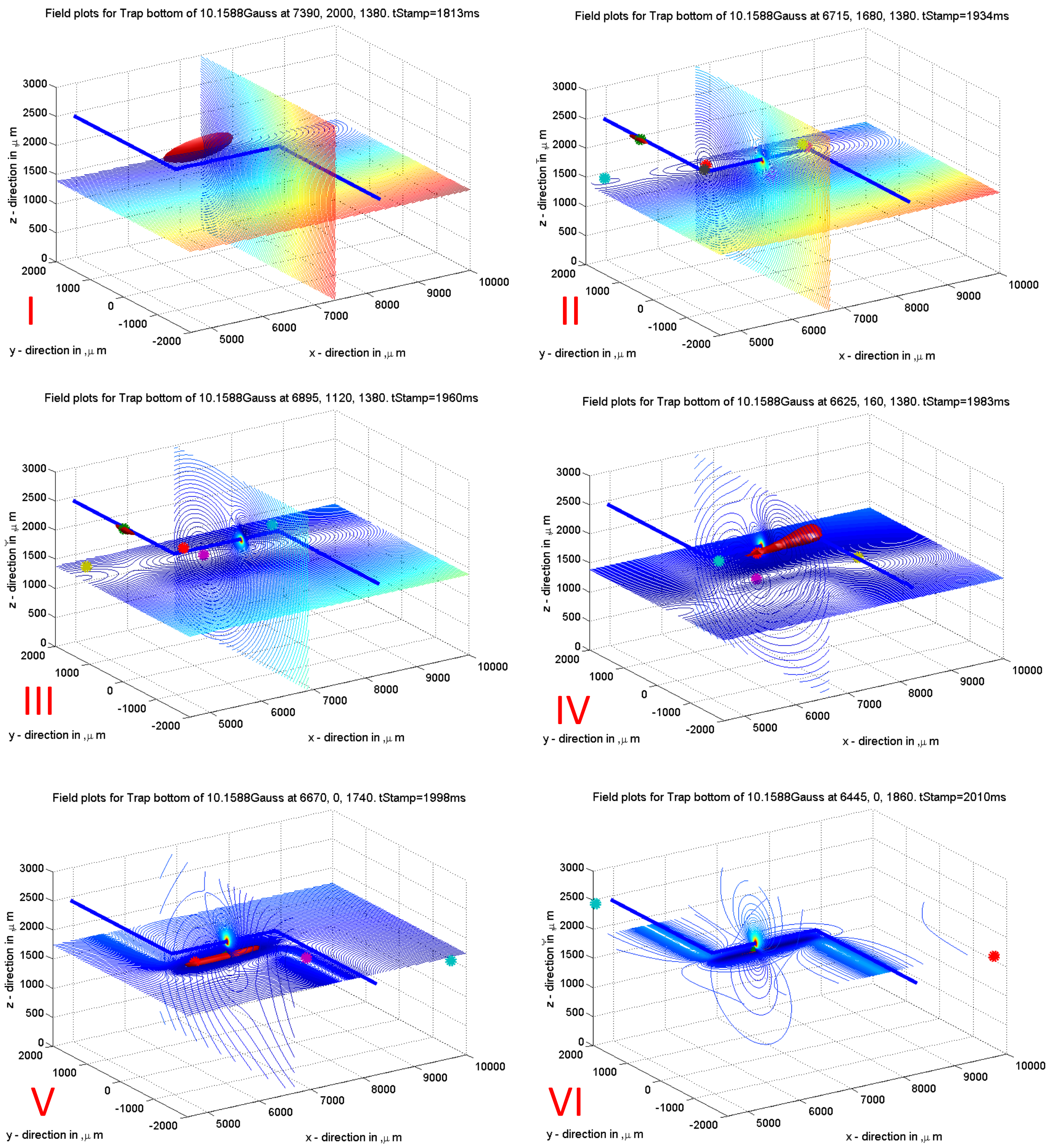

Fig. 5.5 Full loading simulation from the QUIC trap to the Z-wire trap. The Roman numerals correspond to the time stamp snapshot markers denoted on figure 5.4b. The iso-surface is set to 3 G. However, in some of the snapshots there is no iso-surface. The trap is can still be seen with the contour plane cuts since these are cut through where a properly trap minima is found.

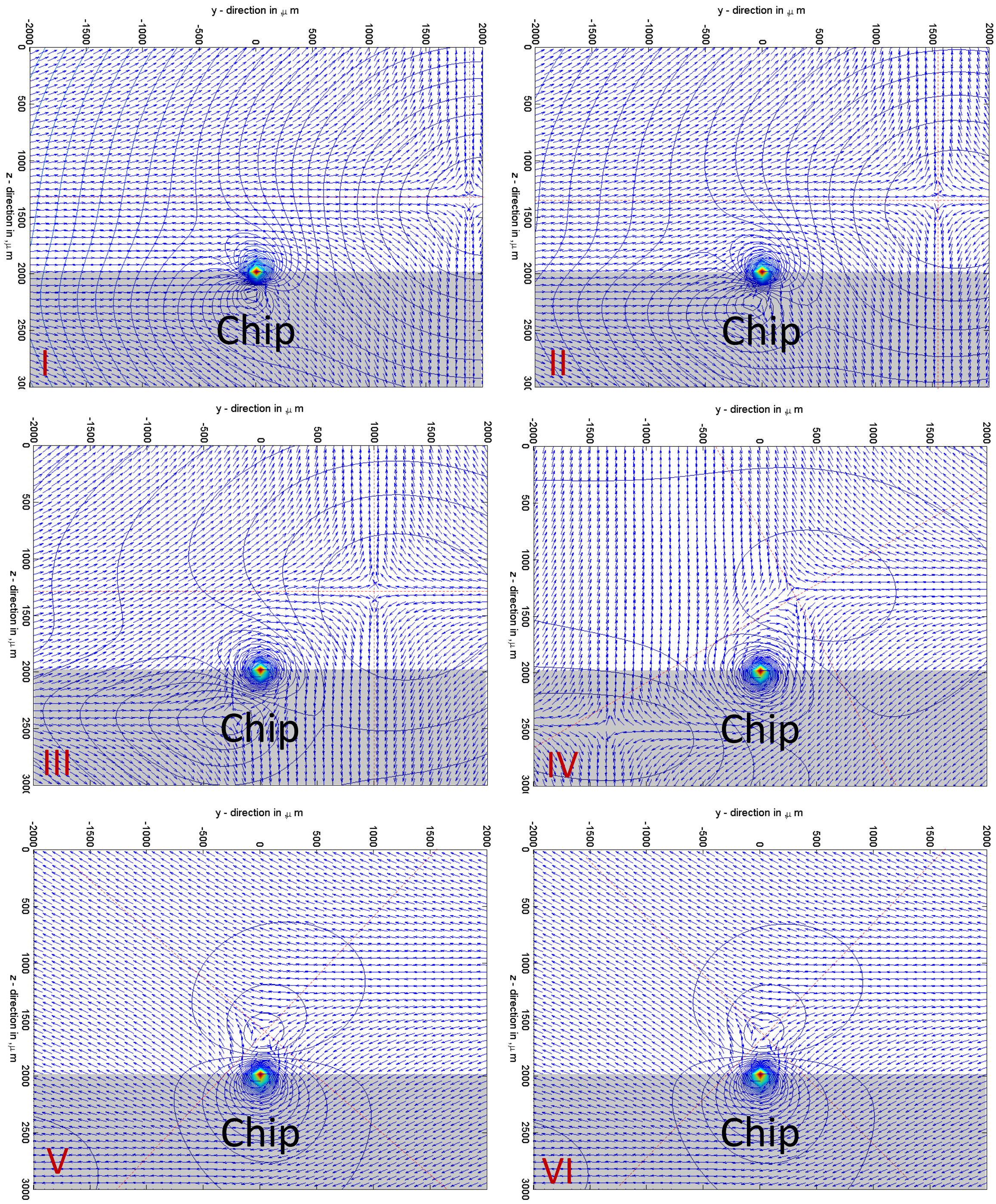

Fig. 5.6 Loading contour cuts at the y-z plane of the 3D visualizations of figure 5.5. Note that only the interesting snapshots when the actual loading takes place. This happens between points III and V where the QUIC quadrupole rotates to 45° to fit into the Z-wire trap as the ramps occur.

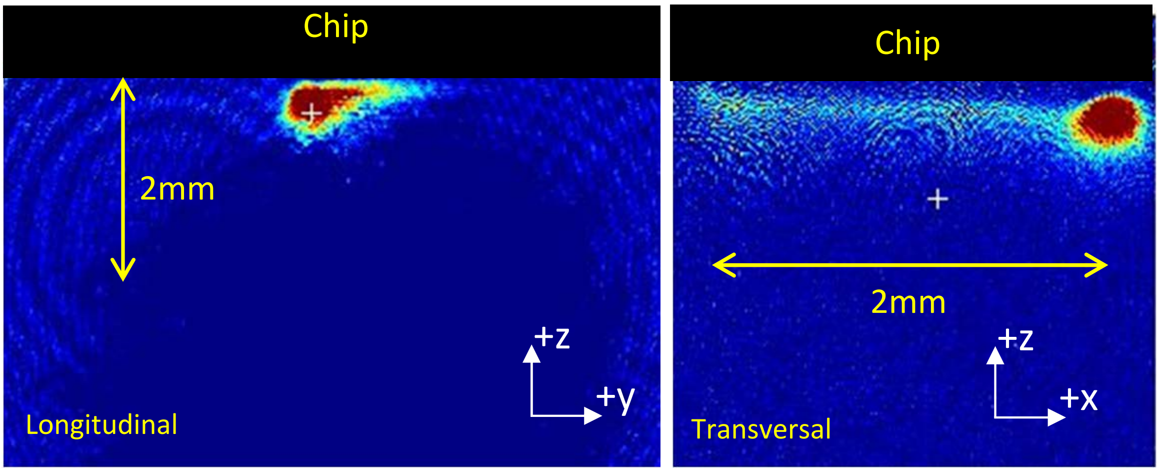

Fig. 5.7 Meissner trap along the niobium Z-structure using both imaging directions.

how the QUIC quadrupole axis rotates to the new quadrupole orientation as the I_{QUIC} is decreased. The trap easily slides into the new field vector orientation. Despite the slight changes in the trapping strengths, the entire loading process can still achieve 100% loading if done slow enough not to induce non-adiabatic heating in the atoms.

Experimentally, it is very difficult to find out where the Z-wire is located with respect to the QUIC trap or whether or not they are aligned with each other. Without the longitudinal or ioffe axis imaging in combination with the main imaging axis the loading process would have been difficult to implement. In order to locate the Z-trap, the Z-structure has to be mapped out relative to the both imaging planes. Fortunately, superconductors have a handy property for this to be possible. This was done by using the Meissner effect which can also be used to make a temporary trap to map out and outline the Z-trap [80]. A vertical field normal to the niobium film will be deflected around the superconductor through the Meissner effect. This creates a trap at the surface of the superconductor. Since the trap is not a closed, atoms are not long lived. Despite this, it can still be used to map out the Z-structure. This is shown in figure 5.7 where the Z-structure is clearly outlined.

Figure 5.8 shows the implementation of the sequence in figure 5.4b. The proposed loading sequence worked immediately even without further fine-optimization. Further optimization produced colder atomclouds. From the initial QUIC trap to the final superconducting trap, there is a slight offset in the Z-trap position along the y-axis. The same goes for the x-axis. After testing several atomchip after the very first one, the loading sequence implemented here was found to be robust and worked nonetheless.

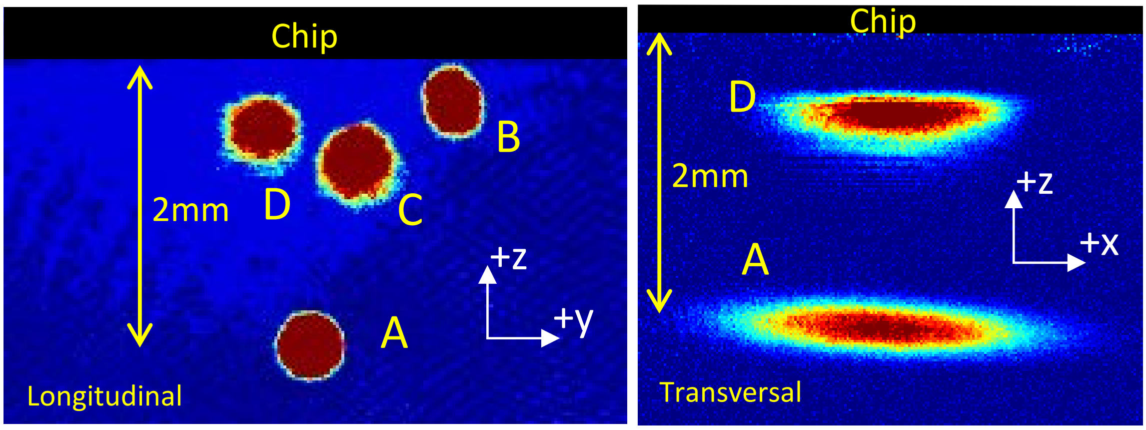

Fig. 5.8 Time of Flight snapshot composite images of the loading sequence implemented in the experiment. Steps A to D correspond to the markers on figure 5.4b. The longitudinal direction illustrates the swing-by maneuver from the QUIC towards the chip trap.

5.3.1 Towards condensation in a superconducting environment

It is also important to note that the atoms loaded from the QUIC trap are pre-rf cooled. From figure 4.6, atomclouds from about 40 µK or colder can be loaded into the superconducting Z-trap. The pre-cooling ramp typically goes from 30 MHz down to 15 MHz or less in about 30 s. Colder atomclouds can also be loaded. However, depending on the desired measurement on the atomchip, pre-cooling can be optimized for a faster cycle with a reasonable amount of atoms in the trap. The first atoms loaded into the Z-structure were about 2×10^6 and typically about 30 µK warm depending on QUIC pre-cooling.

One advantages of the Z-trap is the significantly lower inductance compared to the coils, so it can be switched off in around 50 µs. This allows TOF imaging in the atomchip trap. The bias coils also have fewer windings compared to the QUIC coils and currents required to provide homogeneous fields only go up to a few hundreds of mA. They can be switched off in about 150 µs. Figures 5.9 shows one of the very first TOF measurements on the atomchip. Both axes provide similar measurements. However, the strong trapping direction provides better accuracy since the expansion rate on this axis is faster.

As briefly discussed in chapter 1, there is a massive lifetime enhancement for atoms near superconducting surfaces in the Meissner state. However, this hasn't been observed. Figure 5.10a shows the lifetime of the atom cloud versus its distance to the chip surface. There is a massive reduction of the lifetime ($\approx 5s$). This was greatly

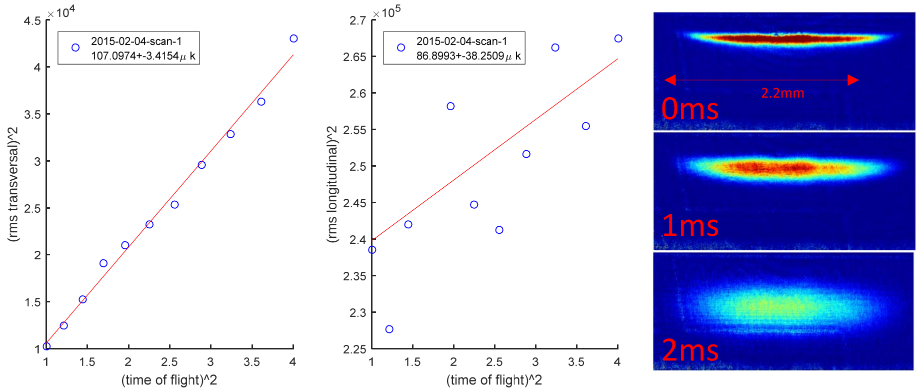

Fig. 5.9 (Left) shows one of the first TOF measurements measurements from the atomchip. The strong trapping direction provides a more reliable result. However, the weak direction with enough data repeats also gives similar results. (Right) shows a few snapshots of the TOF expansion.

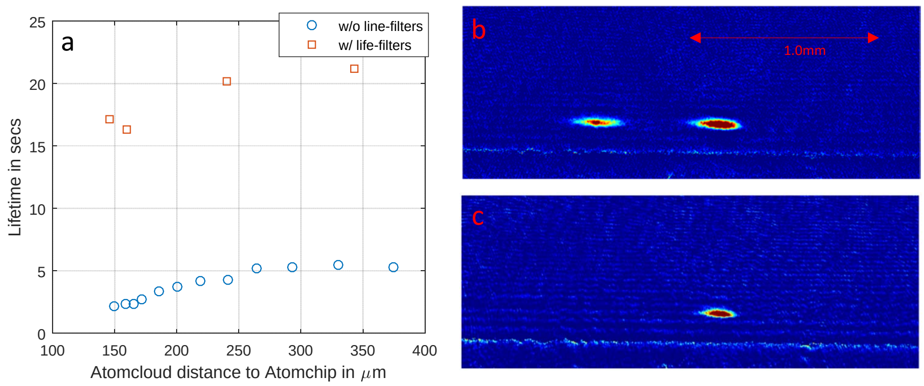

Fig. 5.10 (a) shows the lifetime versus atom cloud to chip distance of behviour of the superconducting trap. (b) and (c) shows the coldest achieved clouds with rf cooling in this superconducting trap using 1.9 A transport current. (b) and (c) depicts the shot to shot variation of the cloud minimum from single to double minima. The atomchip parameters are I_{chip} =1.9 A, B_{ioffe} =3.8 G, B_{bias} =20.4 G, and a measured trapping frequency of 35 Hz×250 Hz.

improved by a factor of 3 to 4 by running the transport current connection feedline with AC-line-filters.

Pre-cooling in the QUIC trap was already performed and optimized even before the presence of the superconducting atomchip. With the addition of the working superconducting atomchip, there was a noticeable degradation of the QUIC lifetime which affected the pre-cooling. This was found to be caused by the presence of the niobium Z-structure. Installing solid-state-relays to disconnect the connection to the atomchip during QUIC pre-cooling (only connecting it when needed) improved the lifetime in the QUIC. The extra noise received by the connections leading to the switches and current sources affected the QUIC lifetime and also the atomchip lifetime. Despite the improvement, there is still a noticeable noise from the Z-wire which will have to be addressed in the future. Currently, there are passive low-pass filter capacitors directly installed at the 4 K stage at the HTc wire solder transition to the coils as shown on figure 3.8. This will ensure maximum noise isolation from everything outside the entire 300 K chamber. These are still currently under going testing.

Figure 5.10b and 5.10c show the coldest achieved atom cloud in the superconducting structure. The cloud temperature is ≈300 nK with 10^4 atoms. Despite this, Bose-Einstein Condensation was not achieved due to the double minima at the trap bottom. Figure 5.10b and 5.10c are shot to shot variations of the cloud without changing a parameter in the trap settings or the rf cooling ramp. The minimum alternates between a single and a double minima. It is also clear during the rf cooling ramp that the cloud splits to both minima. This reduces the evaporative cooling effect of the initial atomnumber as soon as the cloud splits. The trap bottom on the left side is probably fluctuating up and down since the trap bottom on the right side is always filled with atoms. It is still unclear what causes this. A similar double trap behaviour was also observed in the superconducting atomchip of [94]. However, no evidence of shot-to-shot fluctuations of the trap bottom was reported.

Chapter 6

Magnetic Field Microscopy

This chapter deals with probing the current distribution of the niobium film from the atom cloud absorption imaging measurements. These measurements are also compared to magnetic field microscopy (MFM) measurements to confirm the features observed with atom cloud absorption images. At distances closer than $2.5w$, where w is the wire width, the magnetic field produced by the transport current along the cross-section starts to deviate significantly from that of a single, infinitely thin wire carrying the same current [71]. Figure 6.1 illustrates a 3D rendering of the atom cloud above the niobium structure. Since the Z-wire is 200 µm wide, atom cloud to chip surface distances of around or less than 250 µm is easily accessible. At distances smaller than the wire width, the atoms are very sensitive to inhomogeneous variations in the current either local or global.

One of the first experiments performed during the initial inception of normal conducting atomchips was magnetic field microscopy of the metal trapping structure

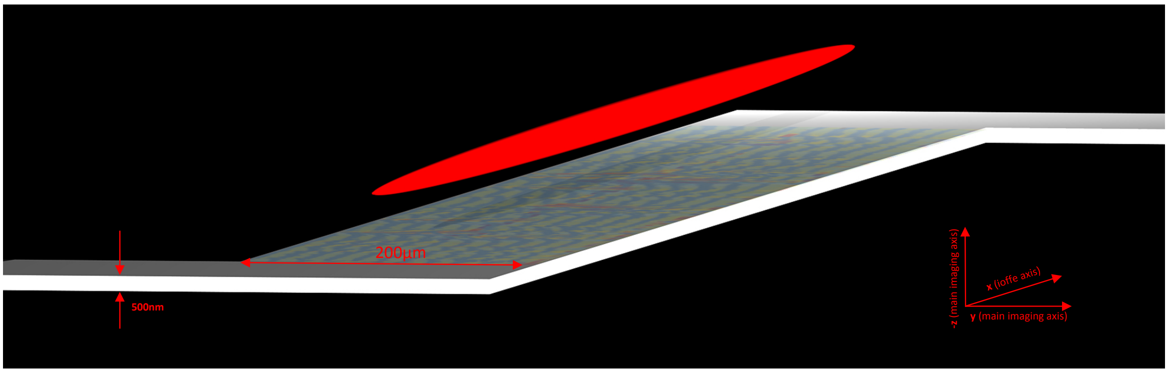

Fig. 6.1 3D rendering of the atom cloud above the 200 µm wide niobium Z-structure. Results of the MFM measurement is overlaid on the Z surface.

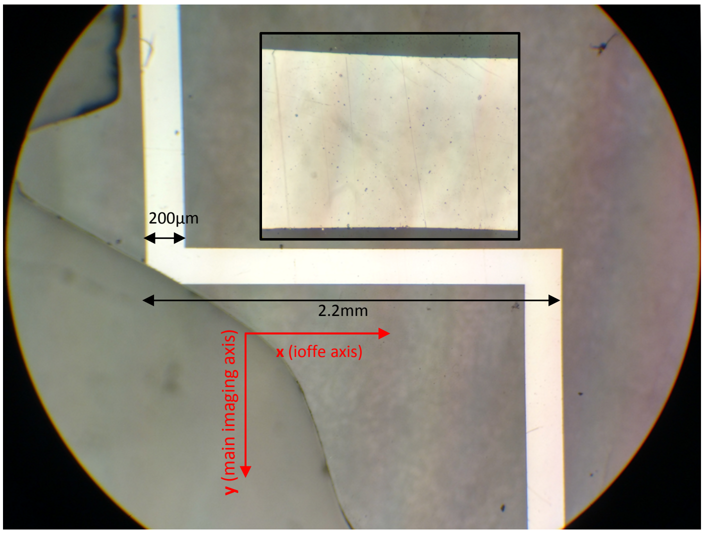

Fig. 6.2 Microscope image of the atomchip in figure 5.2. The inset is a higher magnification image of the niobium surface. The niobium film is 500 nm thick.

using the ultracold atoms [126–130]. The ultracold cloud is very sensitive to magnetic field variations at the trap bottom. For normal conducting current, the current distribution for direct-current (DC) transport current is fairly homogeneous across the cross-section. Any inhomogeneity is caused by either surface roughness, impurities, and/or material defects [127, 129]. These inhomogeneities create local deviation of the current along transport direction that can be measured by the atomic density fluctuations of the ultracold atoms.

6.1 Current distribution analysis of the superconducting trapping wire

Figure 6.2 shows a microscope image of the atomchip in figures 5.2 and 4.1 with the same axes definitions. If the atoms are trapped closer to the wire surface at distances smaller than the wire width, the atom cloud will be sensitive to local currents slightly deviating from the transport direction (see figure 6.1). For a more or less homogeneous current distribution along the film, the atoms can probe local defects that cause the current to vary slightly from the transport direction. These defects may either be material defects, surface or edge roughness [126, 128]. This sensitivity is mainly due to the separability of the trapping potential's transverse harmonic component, $V_{harm}(y,z)$ and longitudinal density, $V_x(x)$ for a total of $V(x,y,z) = V_x(x) + V_{harm}(y,z)$ [127]. The longitudinal density $V_x(x) = -k_B T ln[n(x)]$, where $n(x) = \int\int dydzn(z,y,x)$[1] carries the interesting information of the current variations along the longitudinal direction. Since the trap is very elongated, the atoms act as current ruler probe that can scan the local current variations of the trapping wire [128, 129].

The density of the atoms is $n(x) \propto exp(-V(x,y,z)/k_B T)$ where T is the atom cloud temperature. The atom cloud is thus sensitive to ΔB_x along the longitudinal direction x. However, this is only true for normal conducting wires where the current is homogeneous and for which the separability condition discussed above holds true. Slight variations of $V_x(x)$ can be probed since $V_{harm}(y,z)$ doesn't depend on x. Supercurrents, however, behave differently to their normal conducting counterparts. The magnetic field microscopy methods most especially probing the 2D current distribution of the current flow are not directly applicable to the superconducting case [128–131]. This is mainly due to the Meissner-London currents of the supercurrent where the current distribution tends to stay at the edges of the cross-section to maintain a zero field within the superconductor [132]. Despite this limitation, it is still possible to probe the overall current distribution along the Z-wire using a similar analysis as done in [126, 127]. For low-field seeking ^{87}Rb atoms in the $|F = 2, m_F = 2\rangle$ state, the potential landscape is proportional to the magnitude of the field, $V \propto |\vec{B}|$. For a general inhomogenous current distribution, the atoms at the trap bottom will be sensitive to $\Delta|B|$. For a ^{87}Rb atom cloud at 30 µK, this corresponds to about 222 mG. Longitudinal density variations down to 10% are easily visible with our imaging setup which gives a magnetic field sensitivity of about 22 mG. With colder clouds and Bose-Einstein Condensates, sensitivity down to the nT regime is possible [129] and more recently with a robust cryogenic setup in [133]. However, it is not necessary for now especially when superconductors are involved.

The absorption images for atomclouds about 30 µK at various distances to the atomchip surfaces are shown in figure 6.3. At distances closer than 200 µm, unique features start to appear on the absorption image. The features are the same for all transport currents and after several warming-cooling-down cycles in the experiment. There are points along the longitudinal direction where the trap minimum moves closer to the chip surface. There are also width variations across the cloud. To analyze the data, double Gaussian profiles are fit to the each slice of the atom cloud reflection absorption image. This is illustrated in figure 6.4 which shows a reflected absorption image of the atom cloud. From the double Gaussian fits, the distance to the chip,

[1] The absorption imaging produces $n(x,z)$ which already integrates the density information along the imaging direction y [102, 111].

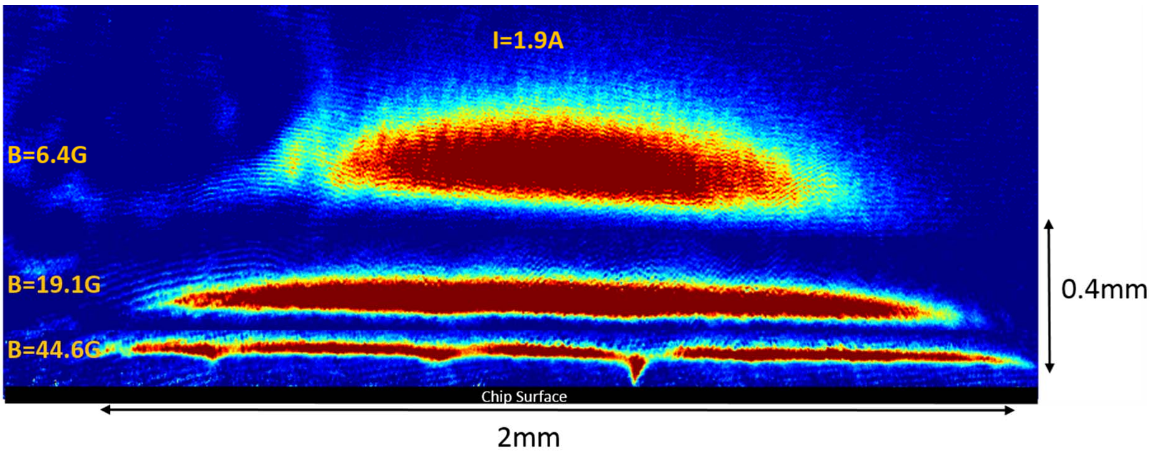

Fig. 6.3 Superconducting atomchip trap absoprtion image composites for various applied bias fields using the niobium structure shown in figure 5.2a. The atom cloud is about 30 µK with about 10^6 atoms. At closer distances, current inhomogeneities start to distor or fragment the cloud.

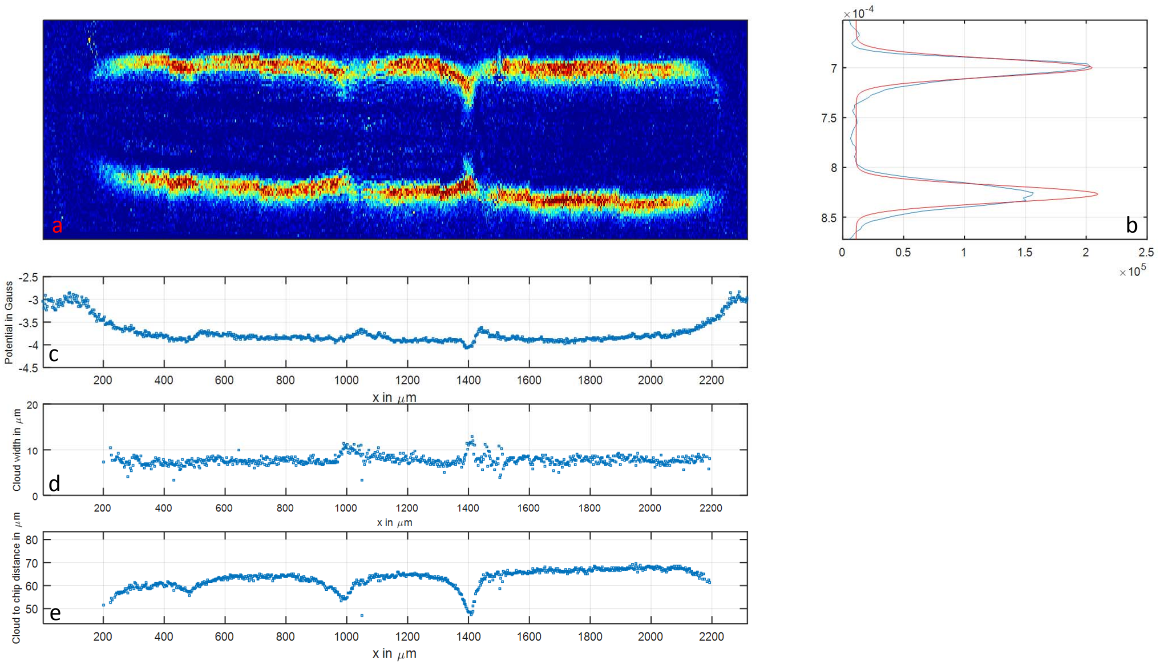

Fig. 6.4 Reflection absoroption image of the atom cloud about 65 µm away from the surface. A current of 1.9 A through the Z-wire and a B_{bias} if 60.4 G are applied. (b) shows the integrated profile along the transport direction with the corresponding double Gaussian fit. The same fit is applied to every vertical slice of the image in order to obtain the atom cloud width (d) and the distance to the chip surface (e).

d, the atom cloud-width per slice, and the trap potential along x can be obtained from integrated atomic density ($n(x)$) as shown in the figure 6.4c. For this particular measurement, the average cloud distance is about 60 µm. At this distance, many of the features are visible. A thorough analysis of the data for all distances is shown on figure 6.5.

Assuming that current flow through the wire is unknown and that there is enough net flow in the transport direction, makes the analysis of the data different from previous experiments. As mentioned earlier, the low-field seeking atoms will be sensitive to $\Delta|B|$ especially at the trap bottom. This means that the atom cloud-chip-to-distance variation along the wire can be due to either a weakening or strengthening of the applied bias field, B_{bias} at certain positions, or redirection of the current away from the transport direction. Local variations of the bias field close to the surface is less likely to be caused by Meissner shielding[2] along the thin niobium film (500 nm) since the wire width (200 µm) is significantly much longer than the film thickness. Meissner shielding is only significant if the applied field is normal to the film. The same arguments can be made with the atom cloud width which depends on the harmonic potential V_{harm} where is in this case it also varies along the transport direction. The potential landscape measures the net distortion of $\Delta|B|$ along the trap bottom whether it is caused by a redirection of current or bias field inhomogeneity. This is clearly illustrated in figure 6.5 where every clear distortion in the absorption image is seen in both Gaussian fit parameters (figure 6.5d, 6.5e) and the potential landscape (figure 6.5c). It is clear that the unique features in the atom cloud distance, width, and potential along the longitudinal direction is caused by overall local current disturbances in the wire cross-section. However, it is still not clear which feature is caused by a current redirection symmetrically which is converging or diverging of the current or asymmetrically where the current makes a turn in one direction.

6.1.1 Comparison with μhall magnetic field miscroscopy measurements

To better understand the observations from the last section, the niobium atomchip used was placed in a μHall magnetic field probe microscopy to measure the current flow characteristics of the the niobium film. The measurement is done in collaboration with the low-temperature-group in the Atominstitut. The device is a bath-type Helium cryostat with a precision multi-axis piezo scanning probe from Attocube with a μHall probe at the tip. It allows magnetic field microscopy (MFM) of magnetic thin films including magnetization and transport current measurements. The probe measures the

[2] With applied fields in the direction of the thin-film, the supercoductor is transparent to the field.

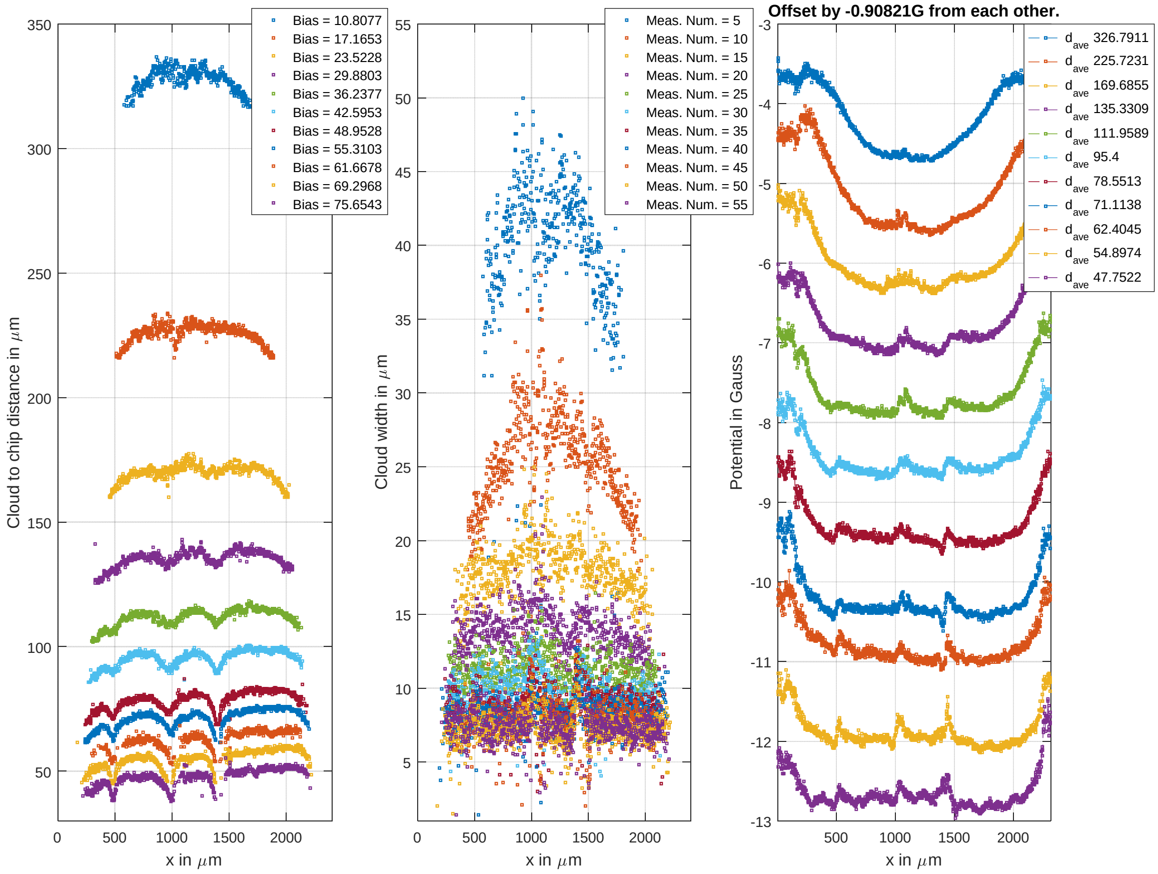

Fig. 6.5 A compilation of various measurements with varying applied B_{bias} from 10.8 G to 75.65G on the chip while maintaining I_{chip} =1.9 A. (left) shows the atom cloud distance towards the chip surface along the wire. (center) shows the width across the length of the atom cloud. (right) shows the calculated potential, from $n(x)$, converted to Magnetic field as the cloud moves closer to the chip surface. Each measurement is offset by an arbitrary amount for better visualization. Note that each legend color and legend entry per plot corresponds to each other only with varying information.

magnetic field component normal (z-diretion) to the film being probed. Details of the setup are well documented in [104, 134–136].

Figure 6.6a shows the raw magnetic field measurement of niobium film. Before measurement, the film is fully magnetized with about 2 T. This ensures that the superconductor is fully penetrated and saturated with vortices forming an Abrikosov lattice [89]. The macroscopic effect of the vortices is a current circulating around the film or simply a magnetization [137]. The measurement shows a lot of interesting features as shown in figure 6.6a. One might immediately be tempted to compare them directly to the atom cloud measurements in the previous section. At first glance, there is a clear defect affecting the critical current along the slice at $x \approx$2.1 mm. This is also

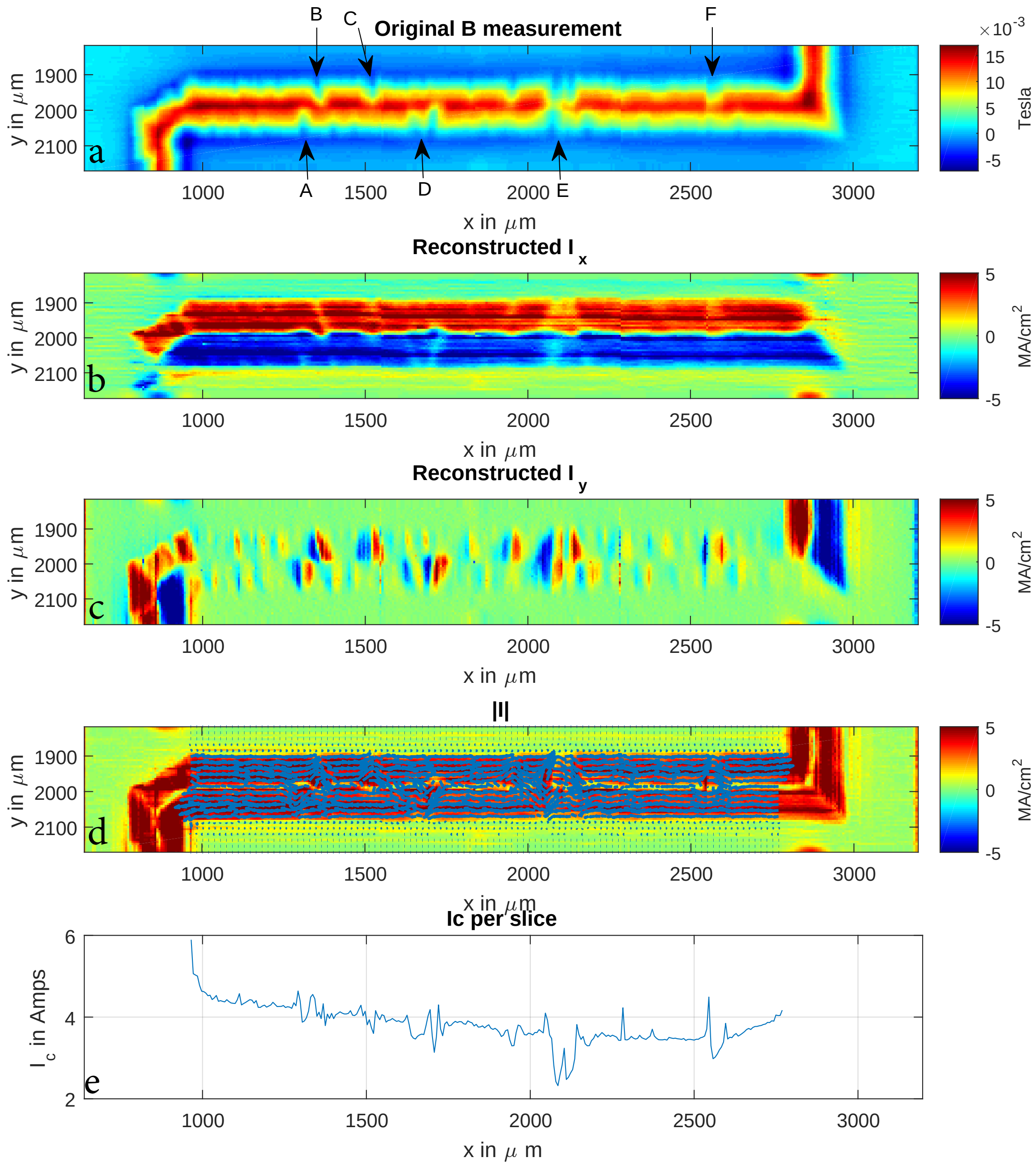

Fig. 6.6 Analysis summary plot compilation of the Magnetic Field Microscopy using a μHall probe of the niobium Film in figure 6.2. (a) shows the original magnetic field measurement of the a fully magnetized niobium film. (b) and (c) show the reconstructed current distribution in the both axes using the Toeplitz matrix inversion algorithm. (d) shows the magnitude of the total current with the vector directions of the currents. (e) shows the critical current for every location of the wire cross-section along the transport direction, x.

the weakest link in the superconducting strip limiting the overall measured critical current of the film. In this case, the measured field is significantly lower that other slices along x. The points along the strip where there are possible defects are indicated by the arrows. At around $x \approx 1.3\,\mathrm{mm}$, the currents makes a zig-zag motion where at points $x \approx 1.52\,\mathrm{mm}$ and $x \approx 1.7\,\mathrm{mm}$, the currents favor flowing on one side of the wire. These all appear to be asymmetric redirections of the current.

Although, the measurement is not a direct current transport measurement, the magnetization currents still allow probing material properties of the superconducting film. From the magnetic field measurement, reverse calculation of the current distribution through the Biot-Savart law is not straightforward but also not impossible. It can be done through Fourier domain or convolution methods [138, 139]. To reconstruct the current distribution, we used the method developed by the Low-Temperature Physics group of the Atominstitut [134]. To summarize, the method involves finding the inverse of a Toeplitz block Toeplitz matrix[3]. From [134], the main problem is to solve the matrix equation,

$$\sum_{k=1}^{n_x}\sum_{l=1}^{n_y} K_{i,j,k,l} M_{k,l} = B_{i,j} \tag{6.1}$$

where $K_{i,j,k,l}$ is the Toeplitz block Toeplitz matrix, $M_{k,l}$ is the magnetization matrix, and $B_{i,j}$ is the magnetic field matrix which corresponds to the measurement in figure 6.6a. $K_{i,j,k,l}$ is generated through a discretization of the Biot-Savart law equation with the planar boundary conditions. The derivation is shown in great detail in the appendix of [134]. The key feature of the method is the one-to-one mapping using $i' = i + j(n_x - 1)$ and $k' = k + l(n_y - 1)$ of equation 6.1 which simplifies it into

$$\sum_{k'=1}^{n_x n_y} K'_{i',j'} M_{k'} = B_{i'}. \tag{6.2}$$

$K'_{i',j'}$ is now a block Toeplitz matrix which can be handled easily with common desktop computers' RAM capacity rather than $K_{i,j,k,l}$. To reconstruct the current distribution, one needs to find the inverse of $K'_{i',j'}$ in order to obtain the magnetization $M_{k'}$. The current distribution can then be easily calculated through $\vec{J} = \vec{\nabla} \times M\vec{e_z}$.

Calculating the inverse of a block Toeplitz matrix is not straightforward and can become numerically demanding [140]. The original implementation by [134] was done in C/C++ since an existing implementation of Toeplitz matrix inversion was readily

[3] A Toeplitz matrix is a matrix in which the (main) diagonal for every term from left to right is a constant. A block matrix is simply a matrix that is built in partitions or submatrices. A Toeplitz block Toeplitz matrix is a Toeplitz matrix that can be made from several smaller block Toeplitz matrices.

available. However, recent progress and advancement in open source machine learning coding has provided many scientists an avenue to share numerical techniques and their implementation in various platforms. The vast library includes a very efficient Matlab implementation of Toeplitz matrix inversion [141]. The resulting calculation of the reconstruction current distribution components are shown in figure 6.6b and 6.6c. Figure 6.6d shows the magnitude of the total current with corresponding current vectors to indicate the direction of the current. At first glance, it is clear that the magnetization measurement has provided a lot of information on the current flow in the niobium film used. At about 2.2 mm, there is a clear defect which is causing a constriction on the magnetization current which is also evident on figure 6.6e which shows the critical current across the cross-section along the length of the wire. This is marked point E in figure 6.6a. A similar behavior, although not as strong is observed on Point F. These points are weak links for the critical current which can also be seen in figure 6.6e which shows the critical current of the wire for every cross-section. The measured critical current of at wire is 2.1 A at about 6.0 K and 3.5 A at 4.2 K. Points A and B on figure 6.6a indicate a zig-zag behavior of the current which can seen in the current components in figure 6.6b and 6.6c and as well as the current vectors in 6.6c. On point D, a similar behavior is observed. Although, the current appears to favor one side.

The magnetization measurement is not enough to describe the real transport current distribution along the cross-section of the niobium film for an applied current. However, it still reveals defect areas that might deflect the currents if a transport current is applied. From figure 6.6d, it is clear if a transport current were applied, it would encounter similar distortion. The initial observed defects (arrows in figure 6.6a) already indicate where the currents are massively inhomogeneous. The net transport current even with the superconducting effects (eg Meissner-London currents) will be very inhomogeneous.

There were already hints of the niobium film's defects or current distribution inhomogeneity with the measurements using the ultracold ^{87}Rb atoms in the previous section. With the reconstruction analysis of the MFM measurements, the different measurements can be compared side by side. Figure 6.7 shows a comparison of the measurement from the ultracold atoms and the MFM. Figures 6.7a, 6.7b, and 6.7c are properties obtained from the absorption imaging of the cloud whereas figures 6.7d, 6.7e, and 6.7f are the reconstructed current distributions from the MFM measurement. The green dashed lines indicate the points where the atom cloud measurement match with the MFM measurement whereas the red dashed lines indicate a feature in one

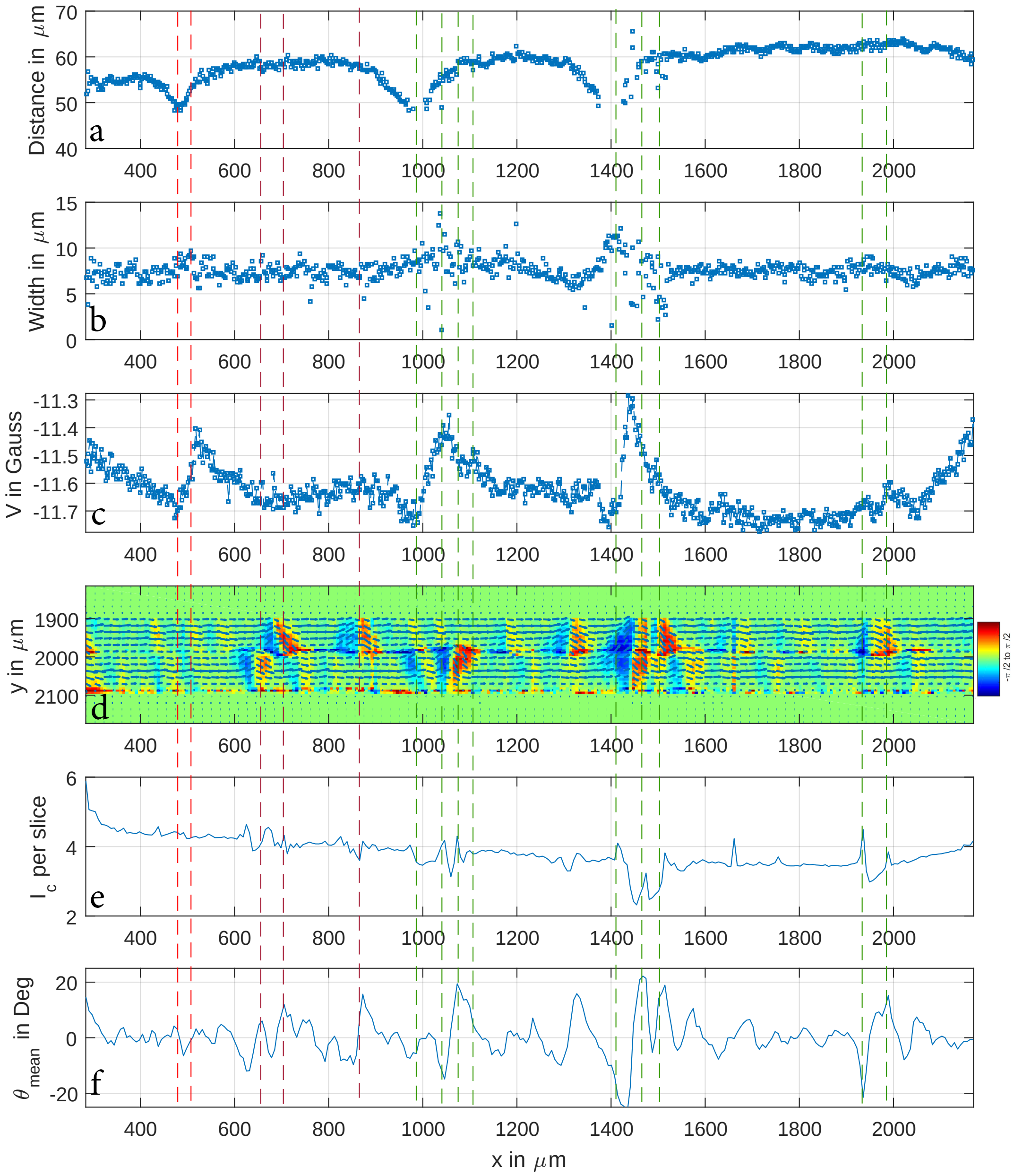

Fig. 6.7 Comparison between atom cloud absorption imaging measurement and the MFM measurement with the μHall scanner. The first three plots are for the atom cloud where (a), (b), and (c) show the atom cloud distance to the chip surface, the atom cloud width variation and the potential along the Z-wire, respectively. The bottom three are from the MFM measurement where (d), (e), and (f) show the angular deviation of the current from the transport direction, the critical current I_c variation, and the average angular deviation of the current along the entire wire length, respectively. The arrows indicated in (d) illustrate the net direction of the current at the local position with the colormap underneath indicating every local angular deviation in the niobium film.

measurement that is not correspondingly visible in the other. The potential measurement in figure 6.7c probes the general distortion of the current along the transport direction.

It is also important to note that the MFM measurement was done right after this chip broke after quenching attempts. The niobium film fractured enough to break sapphire substrate. Or perhaps, the rapid thermal expansion from heating on top of very cold surface broke the sapphire substrate. This is visible in figure 6.2. The cracked side corresponds to the left side of the measurements in figure 6.6. During the quenching event that broke the atomchip, it is possible that new defects might have been introduced within the niobium film.

6.1.2 Atom cloud-distance-to-chip Analysis

In the previous chapters, the cross-sectional current density distribution of the 200 µm wide niobium Z-wire has not been considered. So far, only the atom cloud density fluctuations were considered to indicate the presence of possible material defects that massively redirect current. However, simple atom cloud distance to the chip surface for varying applied bias field has not been analyzed. The distance behavior of the cloud for various bias fields and currents can tell a lot about the current distribution along the cross-section of the wire. Figure 6.8 shows the distance of the atom cloud at the center towards the chip surface for increasing applied bias fields for a transport current of 1.9 A as well as for 1 A and zero current. For every possible transport current, the same features from the previous section are observed in the absorption image of the atoms.

Due to the Meissner effect, the cross-sectional current density distribution is expected to be very different [142]. Currents that flow on the edges of the wires often called Meissner-London currents. Currents minimize the magnetic field within the superconductor. This was the first cross-sectional current density distribution proposed to fit the data. The plot also includes the curve for a homogeneous current over the 200 µm width. The Meissner-London currents approach a homogenous current distribution for increasing I_t/I_c. Since Meissner-London currents are very small in the middle of the wire, the trap approaches the wire surface faster as the chip bias increases. Beyond 40 G, the trap opens up to the surface. However, as shown in the fits, none of the proposed models fit the experimental data for a transport current of 1.9 A. The best possible fit appears to be from a simple case of an infinitely thin wire. The atom cloud distance ranges from from 350 µm down to about 50 µm. Below 250 µm, the current distribution along the cross-section should deviate from the infinitely thin

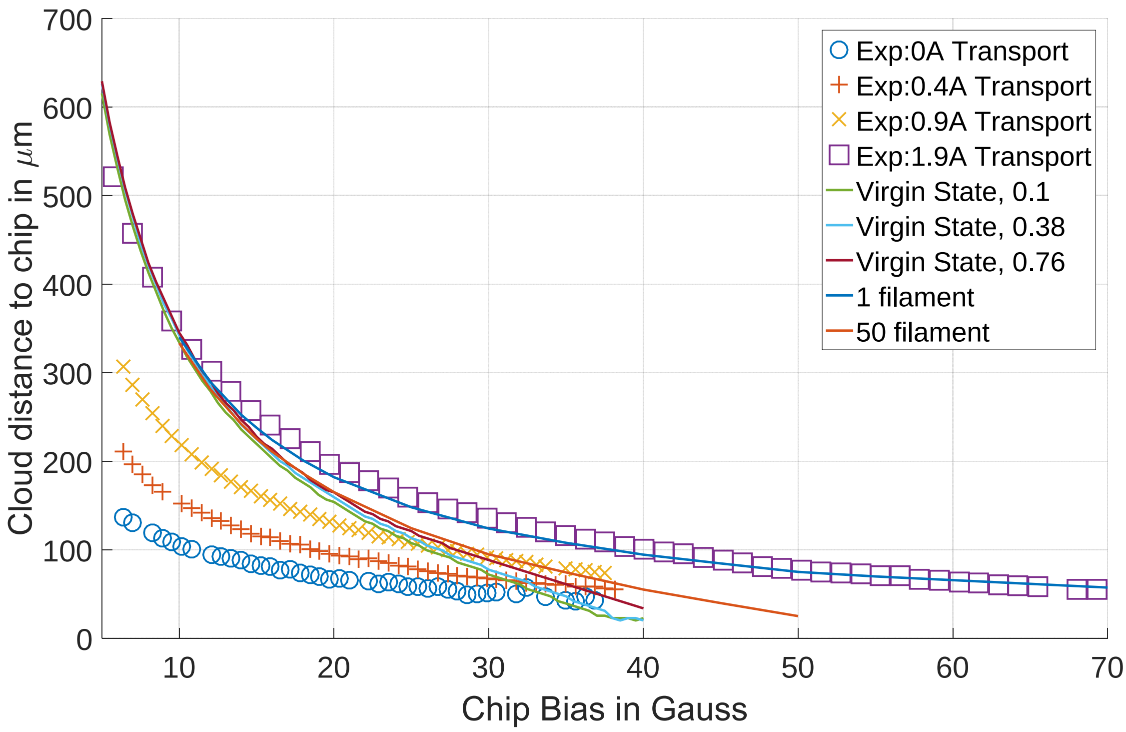

Fig. 6.8 Atom cloud distance to chip versus bias field. The discrete solid dots are measurement points for an applied transport current of 1.9 A. The solid curves shown are the results minima of the full 3D simulation of the wire geometry according to various cross-sectional current distributions. The first three fits are for virgin state Meissner London currents for a rectangular cross section superconductor for I_t/I_c ratios: 0.1, 0.36, and 0.76. The last two fits are for a single Biot-Savart filament and a 50 filament stack spanning across the 200 µm width.

wire approximation. This was found to be puzzling in the beginning. However, it was found to be evidence of current-pulse magnetization of the niobium film which can happen for type-II superconductors. The presence of the current pulse magnetization is evident especially with the presence of the zero-current trap where a Z-wire-like trap still exists even a transport current. The zero-current-trap has never been observed before especially for current-pulse magnetization which was predicted by [143]. The full analysis will be discussed in detail in the following chapter.

Part III

Novel Science and Technology with Ultracold Atoms near Superconducting Surfaces

Chapter 7

Novel Superconducting Traps

In the very last section of the previous chapter, evidence of a remnant magnetization trap was presented. A typical atomchip trap was still observed despite the lack of transport current. This indicates the presence of a current-pulse induced magnetization. This process is not often studied in the superconducting community since magnetization in type-II superconductors is more easily induced with magnetic fields. In this chapter, we will look into superconducting properties of type-II superconductors, especially regarding how they can affect the atomchip trap. The macroscopic theory of magnetization of hard superconductors will only be discussed qualitatively. Various atomchip based traps using superconducting properties will be discussed and measurements will be presented where available. The last section of this chapter will deal with how the cross-sectional current density distribution in superconductors can be controlled through the superconducting film's magnetization history. This feature can be used to control the effective width of the wire trap by inducing a magnetization with a current pulse. This type of trap has never been demonstrated with standard room temperature atomchips. Typically, a narrow wire is desired for atomchip[1] Z-structures since it provides tighter traps. However, due to the possibility of the controlling the remnant magnetization, thicker Z-wires can be prepared to behave like a thin wire.

7.1 Introduction to Basic Superconductor Theory

As briefly discussed in the introduction, superconductivity is the formation of loosely bound pairs of electrons called Cooper pairs that couple via lattice vibrations in

[1] Ultracold atomic physicists are used to the unit Gauss. From this point onwards, all bias field units for the atomchip will be expressed in Gauss for the the atomic physicists' pleasure. Superconducting properties like critical fields will be expressed in proper SI units, Tesla.

the material [38]. They have a net integer spin making them behave like bosons and thus can occupy the same ground state and form a condensate. This occurs below a critical temperature, T_c, for certain materials that allow this pairing which are hence called superconductors. According to BCS theory, Superconductivity is characterized by an energy gap (Δ) that is proportional to Debye frequency (ω_D). A simple picture illustrating Cooper pair formation from the BCS theory is through the lattice-deformation picture [144]. An electron moving through the lattice with the fermi velocity (v_F) deforms the lattice locally by $\approx v_F \frac{2\pi}{\omega_D}$. The local distortion creates a pseudo ion and attracts a second electron with opposite momentum. Typical deformations range from 100-1000 nm. Hence, Cooper pairs are extended objects[2]. The Cooper pair ground state levels are separated by 2Δ from unpaired electron states. Thus, in order to break the Cooper pairs, an energy greater than 2Δ is required. This is the main consequence of the BCS theory where the BCS ground state of the Cooper pairs lies below the fermi surface by an energy Δ.

The BCS theory as briefly mentioned in the introduction explains superconductivity for type I superconductivity[3] very well [38]. It also explains type-II superconductivity as long as it doesn't concern the vortex line formation. Despite the success of BCS theory, it is only limited to superconductors in the weak coupling limit. Most elemental superconductors such as niobium, tin, and aluminum can be explained nicely with BCS theory. Recent experiments with unique high pressure conditions have shown BCS theory to hold for diatomic compounds under high pressure with a critical temperature of 203 K [145].

Another theory that describes superconductivity very well especially the difference between type-I and type-II is the Ginzburg-Landau[4] (GL) theory [89, 147]. The GL theory, in a nutshell, is a phenomenological theory which assumes a complex order parameter, ψ that defines the state of order of the material. This order parameter is related to the density of superconducting electrons by $n_s = |\psi|^2$. In the GL formalism, superconductors are characterized by two length scales: the coherence length, ξ and the penetration depth, λ. The energy gap, Δ of the superconductor depends on ξ which gives the spatial coherence length scale between electrons within the superconducting

[2]In contrast to Alkali BECs where the interaction lengths are shorter. Though, it can tuned with the Feshbach resonance.

[3]Type I superconductors are often called conventional superconductors exactly for the reason that it can be understood very well using the BCS theory.

[4]Microscopic and macroscopic theory of superconductors is a very extensive field that in itself can be a separate work. It was found that the Ginzburg-Landau equation can be derived from BCS theory by [146]. Though, a motivated reader who is not specializing in superconductivity is encouraged to read more about this topic for more clarification.

electron pair cloud. The perfect diamagnetic behavior of superconductors called, Meissner-Ochsenfeld effect (Meissner effect for short) is characterized by λ. The Meissner effect is the shielding effect that type-I superconductors produce when there is an applied magnetic field. Supercurrents that shield the interior of the superconductor are created to counteract the field. The spatial extent to which a magnetic field can penetrate the surface of the superconductor is the penetration depth, λ.

BCS theory, however, does not thoroughly explain high critical temperature, T_c of hard superconductors which are classified type-II. Type-II superconductors can have a T_c as high as 138 K (not subjected to high pressure). They are mostly insulators or have very bad conductance in their normal conducting state. They are best characterized by the formation or penetration of vortices if an applied field exceeds a certain critical field, H_{c1} [89]. Above H_{c1}, magnetic fields start to penetrate the superconductor along flux lines of width 2λ through superconducting vortices. A superconducting vortex is a quantized supercurrent circulating around a normal conducting core of diameter 2ξ. Each vortex contains a quantized flux of $\phi_o = h/2e$ where h is the Planck's constant and e is the elementary charge in the Ginzburg-Landau theory. The difference between type-I and type-II superconductors is determined by the ratio between the coherence length and the London penetration depth, $\kappa = \lambda/\xi$ called the Ginzburg-Landau parameter [147]. If $\kappa < 1/\sqrt{2}$, the the superconductor is type-I whereas if $\kappa > 1/\sqrt{2}$, it is type-II. If $\lambda\sqrt{2} < \xi$, the vortices are not allowed to form since the superconductor would just collapse back into the normal conducting state. Hence, type-I supercondcutors are only characterized by one thermodynamic critical field, H_c. For type-II superconductors, the first critical field is $H_{c1} = \frac{\phi_o}{4\pi\mu_o\lambda^2} ln(\kappa)$ and the second critical field is $H_{c2} = \frac{\phi_o}{2\pi\xi^2}$ in the approximation of the Ginzburg-Landau theory. Note that H_{c2} only depends on the size of a single vortex.

Figure 7.1 shows a phase diagram for type-II superconductors. Below H_{c1}, the superconductor is in the Meissner state, which is often called virgin state since vortices are absent. Above H_{c1} and below H_{c2}, the superconductor is in the mixed or Abrikosov state where vortices have started to penetrate forming an Abrikosov lattice [89]. If the total amount of vortices produced is enough to exceed H_{c2}, the superconductor returns to the normal conducting state. For a thin film superconductor of a certain area (A), the maximum number of vortices that can penetrate before superconductivity breaks down is $n_{max} = \mu_o H_{c2} A/\phi_o$, where A is the total area of the superconducting film.

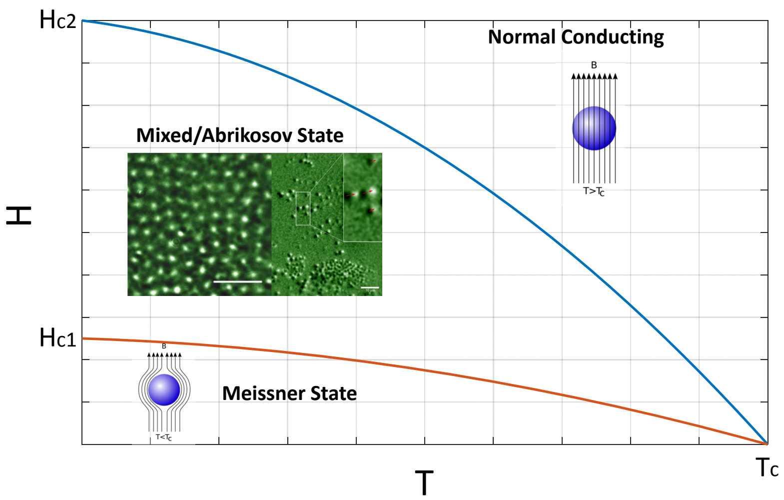

Fig. 7.1 Superconducting phase diagram of type-II superconductors. Type-I superconductivity is characterized by a single critical field, H_c wheres type-II superconductors have two critical fields, H_{c1} and H_{c2}. If $H < H_{c1}$, the superconductor is in the Meissner state where if $H_{c1} < H < H_{c2}$, field lines start penetrating the superconductor through vortices. The photo inset shows magneto-optical imaging of vortices in the Abrikosov or mixed state which is a unique method that allows time-resolved imaging of superconducting films using the Faraday polarization rotation of light [148]. Exceeding H_{c2} will bring the superconductor back into the normal conducting state.

7.1.1 Hysteresis Behavior in type-II superconductors

One main consequence of vortex formation of vortices is the hysteresis behavior of the type-II superconductors in the mixed state. Superconductors can maintain a remnant magnetization even after the application of the magnetic field exceeding H_{c1}. This is due to the vortices that remain in the superconductor due to vortex pinning. The pinning sites are usually defects or simply holes that allow the formation of a normal conducting cores where the position of the flux is energetically favored. This manifests itself as an irreversible magnetization of the superconductor. The magnetization behavior of type-II superconductors in the mixed state gives rise to the hysteresis behavior similar to magnetic hysteresis in ferromagnets.

Superconductivity is still a widely growing and improving field. There is no absolute microscopic theory to describe type-II superconductors, especially not their high T_c. For describing the magnetization though, it is enough to use macroscopic or phenomenological theories. One of the most successful macroscopic theories is the Bean critical state model [137, 149]. The model is widely used to describe nearly all high T_c superconductors such as YBCO. The Bean model assumes a vanishing H_{c1}

and only one relevant critical field, H_c. Thus, the model only describes everything that can happen in the mixed state or critical state. In summary, the model treats vortices as macroscopic currents which induce a field gradient, $\vec{j} = \nabla \times \vec{M}$ where $\vec{M}$ is the magnetization of the supercondutor. As the applied field H_a is increased, vortices start penetrating the edges of the superconductor up to a certain boundary. In the areas where vortices have penetrated, the critical current density J_c flows and creates the field gradient.

The Bean model describes high T_c superconductors very well since H_{c2} for most of these superconductors reaches values as high as several hundred Tesla and H_{c1} can reach as low as a few mT. Later, it will also be shown that it is enough to describe niobium which is the highest T_c elemental type-II superconductor. It can also be considered a low T_c type-II superconductor. It has a rather high H_{c1} of about 0.15 mT and an H_{c2} of nearly 300 mT for clean niobium[5]. In the dirty limit, which is the most typical case, these values vary significantly [150].

For superconducting atomchip applications, there are only a few experiments in existence that have probed superconducting properties or used it for trapping ultracold atoms. The hysteresis behavior of type-II superconductors applied to atomchip trapping of ultracold atoms has been studied theoretically [86] and both theoretically and experimentally [85]. Experimentally, type-II traps using YBCO have been studied [85, 81, 83, 84, 74, 100] with emphasis on field programming a remnant magnetization and in niobium [90, 151]. In [80, 79, 78, 96], a persistent current trap for cold atoms was created with a niobium film loop containing a trapped flux. The hysteresis behavior of type-II superconductors has promising applications for atomchip technology. In the next sections, the hysteresis behavior of type-II superconductors will be briefly reviewed, especially regarding current pulse magnetization of the superconducting film following the macroscopic models described in [137, 149, 142] for an infinitely long rectangular thin-film superconductor. The model also accounts for the Bean critical state model for type-II superconductors and applies conformal mapping to calculate the current distribution around partially penetrated regions that resemble Meissner-London current density distribution profiles [132]. Understanding the basics of the current distributions in the film will give clearer insight into the atomchip trapping dynamics observed in the experiment since the ultracold atoms are very sensitive to the transport current producing the magnetic trap. A comprehensive review on sheet current density

[5]The values presented are valued measured for the purest biobium available to the low temperature group of the Atominsistut.

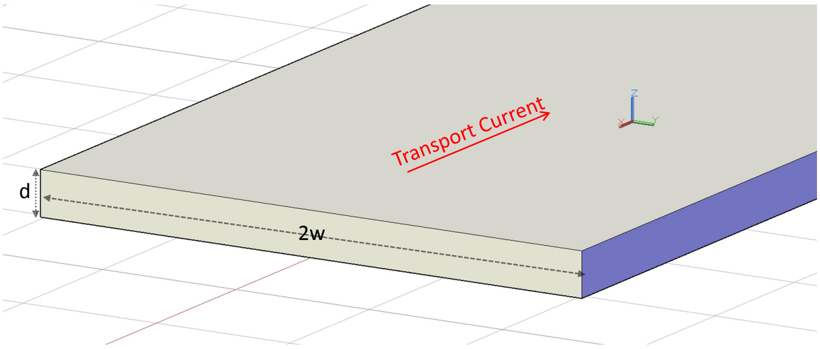

Fig. 7.2 A schematic drawing of a rectangular thin film where d is the film thickness and $2w$ is the wire width. The wire is assumed to be infinite long in the x-direction. Magnetic fields applied in the z-direction induce magnetization currents in the x-direction that vary throughout the cross-section, y-direction.

distributions of infinitely long rectangular type-II superconductors can be found in [152].

Field Hysteresis

Figure 7.2 shows a sketch of a superconducting film wire of width $2w$ and thickness d. Since the superconducting films used fulfill the thin film condition $2w \gg d$, the current density distribution in the z-direction can be neglected making the problem simpler. For an applied field (H_a) normal to the film, the current density distribution of the cross-section is

$$J(y) = \begin{cases} \frac{2J_c}{\pi} \arctan\left(\frac{cx}{(b^2-y^2)^{1/2}}\right) & |y| \leq b \\ J_c y/|y| & b \leq |y| \leq w \end{cases} \tag{7.1}$$

where $b = w/\cosh(H_a/H_c)$ and $c = \tanh(H_a/H_c)$. The region where $b \leq |y| \leq w$ defines the fully penetrated region that is saturated with vortices, forming an Abrikosov lattice. The superconductor is the partially penetrated in the region where $|y| \leq b$. Equation (7.1) is plotted in figure 7.3a for an applied field H_a/H_c increasing from 0 to 2.5. For an oscillating magnetic field with a maximum of $\pm H_o$, the current density distribution along the wire width can be calculated with

$$J_{H\downarrow}(y, H_a, J_c) = J(y, H_a, J_c) - J(y, H_o - H_a, 2J_c). \tag{7.2}$$

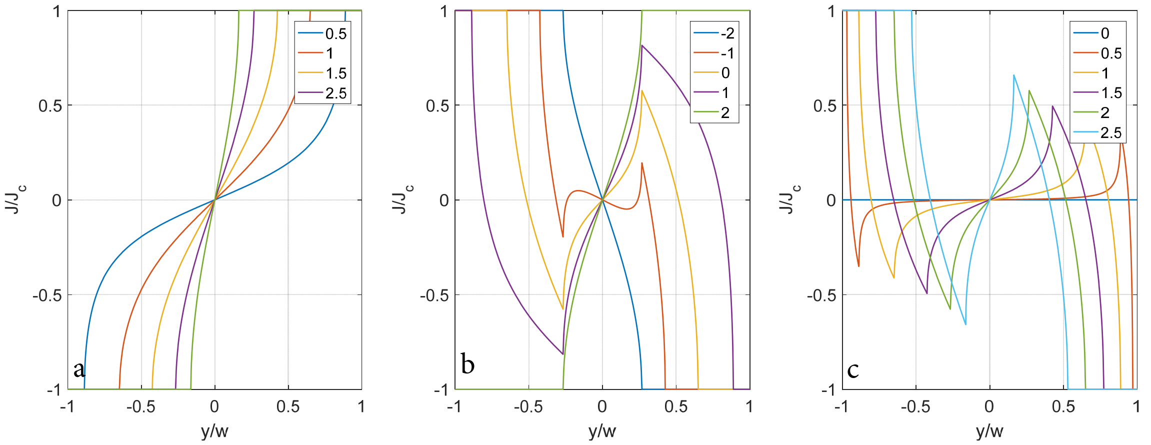

Fig. 7.3 Magnetization currents induced in the x-direction from applied magnetic fields in the z-direction through the superconducting film cross-section y-direction. (a) shows the induced currents by the penetrating vortices for an applied field, $H_a/H_c = 0.5, 1, 1.5, 2$. (b) shows the induced currents if the field is decreased from $2H_c$ to $-2H_c$ starting from (a). Starting from (b), (c) shows the different remnant magnetization currents for a field ramp $0 \to H_a/H_c \to 0$ where $H_a/H_c = 0.5, 1, 1.5, 2$.

To reach H_o from the virgin state[6], equation (7.1) applies. When H_o is decreased to $-H_o$, the current density distribution is governed by equation (7.2). This shown in figure 7.3b. Figure 7.3c shows the remnant magnetization current density distribution for a field ramp $0 \to H_a \to 0$ for various H_a. From the results above, a field magnetized wire can be treated as two wires with a certain spacing carrying opposing currents. For additional field pulses applied, the current density distribution can be calculated by accounting for the entire magnetic field history of the superconducting film. To erase the remnant magnetic field history, a field pulse greater than any other field applied is required. For complete reset of the remnant magnetization history, the superconducting film needs to be brought back into the normal conducting state. This was studied in detail in [85] for ultracold atom trapping applications where the results in figure 7.3 were compared to the combination of two wires carrying opposite currents, or even more wires with alternating current direction.

[6]The virgin state of the superconductor is when there is no sheet current in the superconductor. This is when the superconductor is cooled down below T_c with zero field or quenching it.

Current Hysteresis

For an applied transport current on the same geometry in figure 7.2, the current density distribution starting from the virgin state is described by

$$J(y) = \begin{cases} \frac{2J_c}{\pi} \arctan\left(\frac{w^2-b^2}{b^2-y^2}\right)^{1/2} & |y| \leq b \\ J_c & b \leq |y| \leq w \end{cases} \tag{7.3}$$

where $b = w(1-(I_t/I_c)^2)^{1/2}$ and $I_c = 2wdJ_c$ is the critical current of the superconducting film cross-section. Flux penetrates from the edges up to b similar to the field magnetization case (critical state model). Between $-b$ to b, the current density is governed by Meissner-London distribution [132]. For transport currents close or equal to I_c, the current density distribution is more or less homogenous throughout the cross-section, similarly to a normal conductor.

Figures 7.4a shows the current distribution for various ratios of I_t/I_c. Figure 7.4c shows an image representation for all possible I_t/I_c. It is clear that if $b \approx w$, the superconducting film is nearly in the Meissner state. This approximation is valid for $I_t \leq 0.01 I_c$ where the superconducting film remains nearly vortex free. From figure 7.4c, the fully penetrated regions are the regions indicated by the red colormap threshold where the current density is J_c. This is important to consider for experiments involving lifetime enhancement of ultracold atoms near superconducting surfaces since significantly longer lifetimes are predicted for purely vortex-free films [73].

Decreasing the transport current from a previous maximum value, I_{max} leads to a unique distribution similar to the field magnetization case, where the current distribution for $I_t < I_{max}$ depends solely on I_{max}. The current density distribution can be calculated with

$$J_{I\downarrow}(y, I_t, J_c) = J(y, I_t, J_c) - J(y, I_{max} - I_t, 2J_c). \tag{7.4}$$

The results for the equation above are shown in figure 7.4b and 7.4d for $I_{max} = 0.88 I_c$. As the applied current decreases from I_{max}, the vortices at the edges flip polarity immediately. At zero transport current, $I_t = 0$, there is also a remnant magnetization. Like the field magnetization case, the current distribution in the cross-section at $I_t = 0$ after reaching a previous current maximum (I_{max}) is essentially formed by vortices in the superconducting film. For a certain transport current, its current density distribution is mainly determined by the previously reached maximum, $-I_{max} \leq I_t \leq I_{max}$. Unlike [84], where the trap was formed by remnant magnetization sheet current produced by a

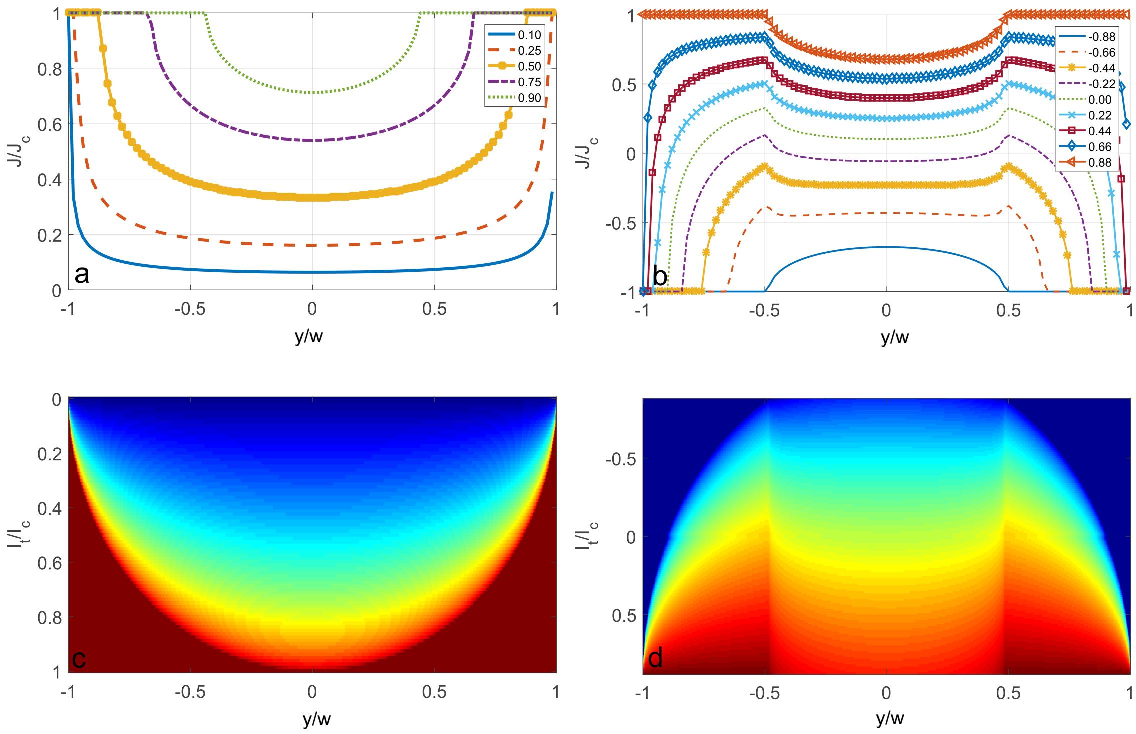

Fig. 7.4 Current density distribution for a rectangular thin film superconductor. (a) shows virgin state current distribution for various I_t/I_c ratios: 0.1, 0.25, 0.5, 0.75 and 0.9 while (c) shows an image representation for all possible values of I_t/I_c. With this, it is easy to pinpoint regions that are fully penetrated with vortices since the colormap clips red at J_c and is fully bllue at $I_t = 0$. (b) shows the current distribution for across the wire width, w for transport current, I_t/I_c varied from I_{max} to $-I_{max}$ where $I_{max} = 0.88I_c$. At $I_t = 0$, there is an induced remnant magnetization. (d) shows all the possible current distributions along the cross-section for a given I_{max} of $0.88I_c$ where the colormap ranges from $-J_c$ to J_c for blue to red, respectively.

field plus an appropriate bias field, a similar trap can also be formed by the application of a current pulse. Resetting the superconducting sheet current memory can be done by either quenching the superconductor or increasing I_{max} beyond its previous value.

Current versus/plus Field Hysterises

The main difference of the current-pulse magnetization compared to the field case is that here the current density distribution along the cross-section is symmetric whereas in the field case, it is asymmetric. The symmetry axis is defined by the center of the wire cross-section. Due to the symmetry, the net current distribution of the current pulse induced remnant magnetization almost resembles three wires with the two outer wires carrying opposing currents to the transport direction. Current pulse

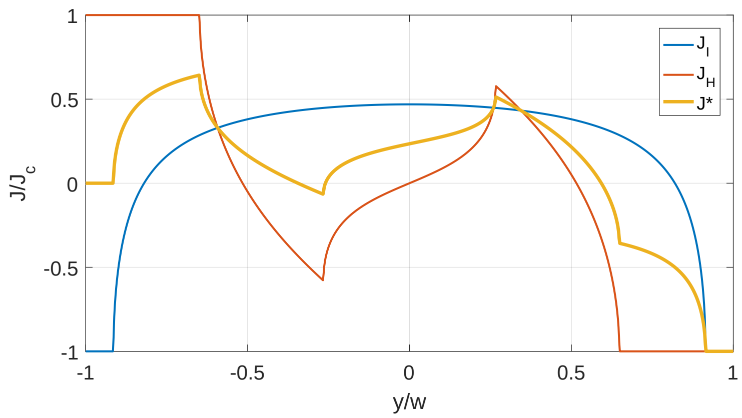

Fig. 7.5 Current density distribution for a remnant magnetization for both field and current-induced. The current-induced component is form by a $I_{max} = I_c$ and $I_t/I_c = 0.19$ where the field component is form by a field pulse $0 \to 2H_c \to 0$.

magnetization may be useful for atomchip applications. The net effect can be viewed as a homogeneous current distribution with a tunable wire thickness. This is essentially the key feature in tailoring the desired current distribution in the superconducting cross-section which will be discussed later. According to [142], the combined effect for a transport current in a perpendicular field can be calculated as an equally weighted sum of the results of the previous section. The net current density distribution is the sum of a combination of the current and the field part where $J^*(x) = (J_I + J_H)/2$. This is shown in figure 7.5 for one case. The field term introduces an asymmetry to the net current density distribution.

7.2 Atomchip traps using remnant magnetization

Both magnetic field and current pulses can be used to induce a remnant magnetization that produces a non-zero sheet current in the superconducting film. This can either be done simultaneously or individually. The superconductors used in the experiment are niobium and YBCO. YBCO is a type-II superconductor with a T_c of $93K$ and a lower critical field, B_{c1} in the order of mT at about 10 K which can decrease with increasing temperature [153]. Its upper critical field B_{c2} can reach up to 140 T making it an ideal hard type-II superconductor that obeys the critical state model very well. YBCO atomchips were studied in great detail in [84, 100, 83] where field pulse magnetization was utilized for trapping ^{87}Rb atoms using the remnant magnetization currents. It was also shown that by controlling the magnetic field pulse history experienced by

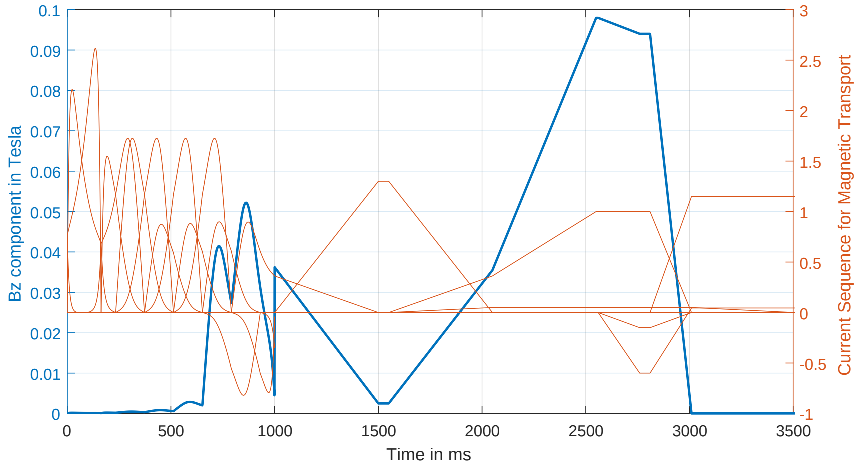

Fig. 7.6 Magnetic field history from the magnetic transport that is experienced by the superconducting film at its mounting position exactly at the surface of the Z-wire in the experiment. From 1500 ms onwards, the transport current for the superconducting Z-trap is ramped up. Ideal wires are used to simulate the field for this case where up to 100 mT is reached. In reality, however, the Meissner effect will prevent this this from happening.

the superconducting film, the current density distribution of the cross-section can be programmed. This mechanism adds a new level of versatility for atomchip trapping.

Niobium, on the other hand is a very unique superconductor. Most literature considers it as a type-I conventional superconductor. In reality, it always behaves as a type-II superconductor [154]. It has a T_c of 9.2 K and B_{c1} of about 150 mT and B_{c2} of 200 mT [150]. There is not enough literature available to explain the peculiarities[7] of niobium. Despite this, niobium can still described by the critical state model to a certain extent. Similar to the YBCO Atomchip results from [83], it can be also be programmable through a field or current pulse. Evidence of niobium's critical state behavior in atomchip trapping was already studied in [151]. Trajectories of ultracold atoms were found to indicate a strong deflection from the magnetization of a nearby niobium surface.

Before going into the results of remnant magnetization traps, we will first examine how the experimental sequence affects the superconducting film. Figure 7.6 shows the magnetic field history experienced by the superconducting film at the position of the Z-structure. This field history is the net perpendicular component produced by all

[7]It is important to remember that only approximate values are presented. Superconductors vary greatly in properties depending on material properties from fabrication. This is true for both YBCO and niobium. For instance, the low temperature group of the Atominstitut has spent years on studying grain boundaries of YBCO and how they affect its superconducting properties. Yet, it is still very much not understood. There is no absolute measured property for type-II superconductors, unlike type-I superconductors which can be described very well with the BCS theory.

the coils in the experiment during magnetic transport. The film experiences about 50 mT during the magnetic transport. For YBCO, this already induces a remnant magnetization in the film. Even right after cooling below T_c, YBCO is said to already have a slight remnant magnetization. Thus, the magnetic conveyor belt transport discussed in chapter 3 will always induced a remnant magnetization for the YBCO atomchips during every loading cycle of ^{87}Rb atoms. For niobium, however, this depends entirely on the material properties of the niobium especially on its actual B_{c1}. This is usually around 100 mT but it can also go as low as 50 mT if the film quality is bad [150, 154]. If the niobium film used in the atomchip has B_{c1} close to literature values, then the magnetic transport should not induce any magnetization. This opens up the possibility of isolating field and current magnetization for total sheet current density distribution control with niobium.

The real current density distribution of the 2D Z-wire across the thin film includes self-inductance effects within every wire cross-section with respect to each other. The current density distribution close to the Z-wire leads becomes different from the infinitely long wire approximation [155, 156]. However, self-inductance effects at the center of the Z-structure are minimal. Thus, the infinitely long wire cross-section hysteresis model described in the previous sections is likely the distribution governing the center of the Z-wire length. The same approximation was successfully applied in [151]. As a first order approximation, the different possible history dependent cross-sectional current density distributions can be assumed to be uniform throughout the entire length. This allows the 3D trapping characteristics of the atomchip for both YBCO and niobium to be investigated without resorting to numerical methods.

7.2.1 YBCO Atomchip

As discussed in the previous sections, the main difference between the sheet current cross-section from field and current-induced magnetization lies within their symmetry. Current-induced magnetization produces symmetric magnetization currents along the film cross-section. This is similar to the trapping behavior of normal conducting trapping structures where the current distribution along the cross-section is usually homogenous. The asymmetry in the field-induced magnetization currents creates an extra field component perpendicular to the film. This tilts the direction at which the trap moves towards the film surface for an increasing bias fields.

Figure 7.7 shows a 3D rendering of the YBCO atomchip used in the experiment. The central 50 µm wide wire is used for trapping the atoms although the two 10 µm wires can also be used. Figure 7.8 shows a simulation of a field-induced remnant

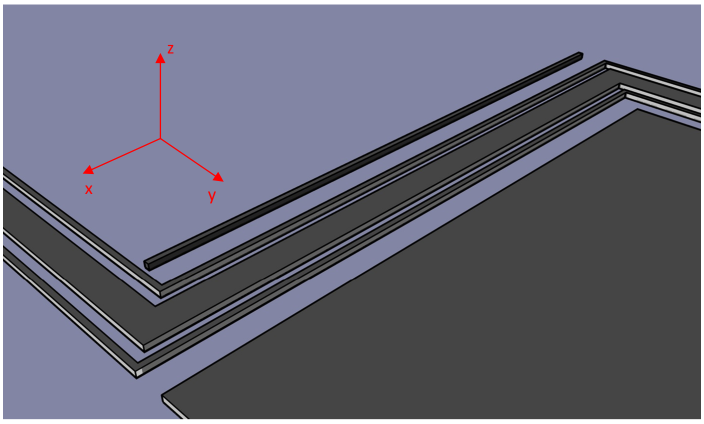

Fig. 7.7 3D redendering of the YBCO atomchip shown in figure 5.3. The film fulfill the thin-film approximation since the YBCO film is 330 nm thick. There is a 100 nm gold layer above the three Z-wires that serves as a quench protection layer since YBCO is a very bad conductor if superconductivity breaks down.

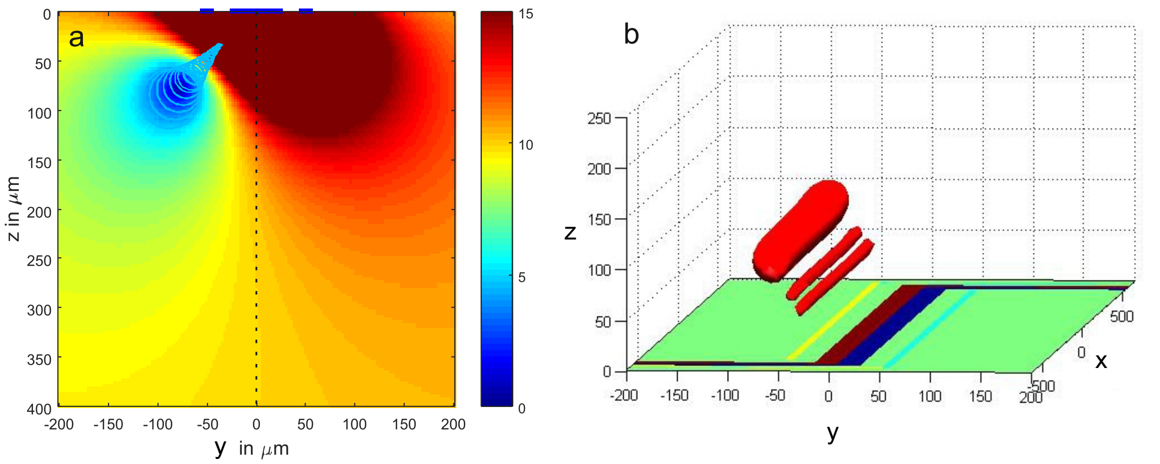

Fig. 7.8 Simulation for a nearly fully penetrated field magnetized YBCO atomchip in figure 5.3 with an applied bias field in the y-direction. This corresponds to an effective counter-propagating current of about 2 A on each side of the central wire. (a) shows potential landscape in the y-z plane at $x = 0$ or center of the Z-structure for a bias of 10 G where the colormap scale is in Gauss. The contour outlines a trap depth of 5 G for an increasing bias of up to 30 G with 1 G increments. The dashed line is the symmetry axis of the atomchip to emphasize the rotated axis of the atomchip trap for increasing bias. The solid blue lines are the outlines of the Z-wires' cross-section. (b) shows a few 3D iso-surface pltos for 10 G, 20 G and 30 G. The colormap on the x-y plane also shows the magnetization currents inside the film.

magnetization trap for the atomchip in figure 7.7. As predicted, due to the asymmetry of the field-induced magnetization currents the trap moves diagonally along the y-z plane for an increasing bias field unlike traditional wire traps, where the trajectory of

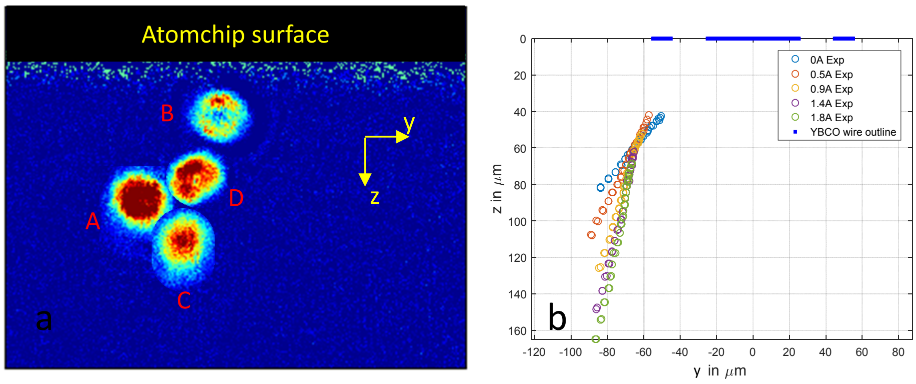

Fig. 7.9 YBCO atomchip in-situ measurements through the Ioffe-imaging (y-axis) direction. (a) shows the absorption images for the remnant magnetization trap (A and B) and the remnant magnetization including a 1.8 A transport current (C and D). The applied bias fields (y-direction) are 10 G (A and C) and 30 G (B and D). (b) shows a summary of the trap positions across the y-z plane for remnant magnetization plus transport currents from 0 A (pure remnant trap) up to 1.8 A. The Z-wire outlines are estimated from the trajectories and the known position of the chip-surface from the absorption image.

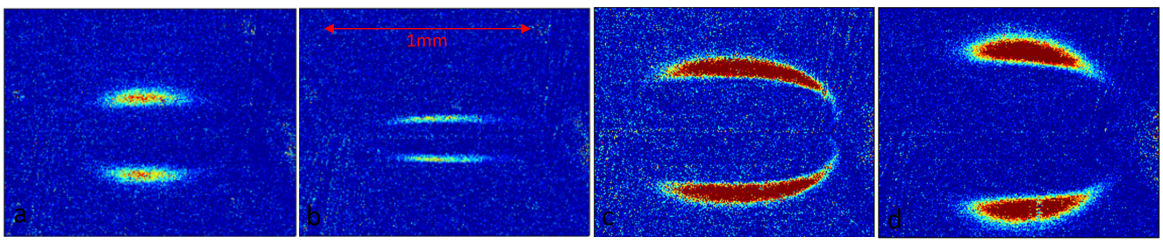

Fig. 7.10 YBCO atomchip in-situ measurements through the main-imaging (x-axis) direction. The imaging system is set in reflection mode where the reflection image is also shown. (a), (b), (c) and (d) corresponds to A, B, C, and D of figure 7.9a, respectively.

the trap for increasing bias moves along the z-axis. This behavior is similar to that of a wire trap with an extra field (z-direction) component perpendicular to the bias (y-direction) field that rotates the trap with respect to the axis normal to the atomchip. The simulation only includes the effects of the three Z-structures and ignores the small and big rectangular islands beside the Z-structures. Similar results can also be obtained by two wires with counter-propagating currents [85].

Figure 7.9 shows the atoms trapped below a YBCO atomchip through the Ioffe imaging direction which images the y-z plane. Figure 7.9a shows the absorption images for purely field-induced remnant magnetization trap and as well as a transport current plus the remnant magnetization. Figure 7.9b shows the extracted positions of the cloud for increasing transport current starting from the pure remnant trap (zero transport current). For the results with transport current, it is very difficult to simulate the full system since the full geometry of the YBCO atomchip involves many structures. Full simulation of the entire system would require a full 2D calculation of the entire structure similar to [151] using numerical methods [143, 156]. Despite the lack of a full comparison between simulation and experiment, the experimental results for the YBCO atomchip indicate that the trap is dominated by the field-induced remnant magnetization trap especially for the pure remnant magnetization trap (0 A transport current). This is indicated by the tilt in the trapping trajectory for increasing bias field. The results obtained here are similar to the results of [83, 100].

Figure 7.10 shows the same results from the main-imaging direction. During experimental operation and measurement (figures 7.10c and 7.10d), the MOT was optimal, hence the high atom number. When the measurements focusing on the remnant magnetization trap were performed, the MOT was not at its optimal performance. This includes all of the results from figure 7.9. The low atom number or atom density has no dependence on the on strength of the trap and was not thoroughly investigated in this case. The lifetime on the YBCO atomchip ranges from 26 s to 3 s for a cloud-to-chip distance of 525 µm and 325 µm. The lifetime decreases dramatically below 325 µm. This is mainly due to Johnson-Nyquist noise from the gold protective layer above the YBCO Z-wire structures [151, 74]

7.2.2 Niobium atomchip

The last section of chapter 6 already hinted on a possible magnetization present in the niobium atomchip Z-structure shown in figure 6.2. The wide 200 µm width niobium Z-structure makes it ideal for testing out the magnetization hysteresis behavior of type-II superconductors. As mentioned earlier, there is a possibility that the magnetic transport might create a field-induced remnant magnetization in the niobium film. Field-induced remnant magnetization adds an observable tilt to the trapping trajectory for increasing bias fields. For all the measurements in chapter 6, there was no tilting in the atom cloud trajectories with respect to the z-axis. This suggests that the magnetic transport does not induce any remnant magnetization.

A perpendicular field was applied up to the highest value that the entire coil setup can provide while measuring the critical current density of the niobium film (See Appendix D). This was an attempt to quench the superconducting film without having to warm up the cryostat. The consequence of this measurement was the inadvertent production of a field-induced remnant magnetization in the niobium film, which is illustrated in figure 7.11. After the application of the maximum field that the bias coils can produce, about 2400 G(240 mT), the reloading scheme into the niobium

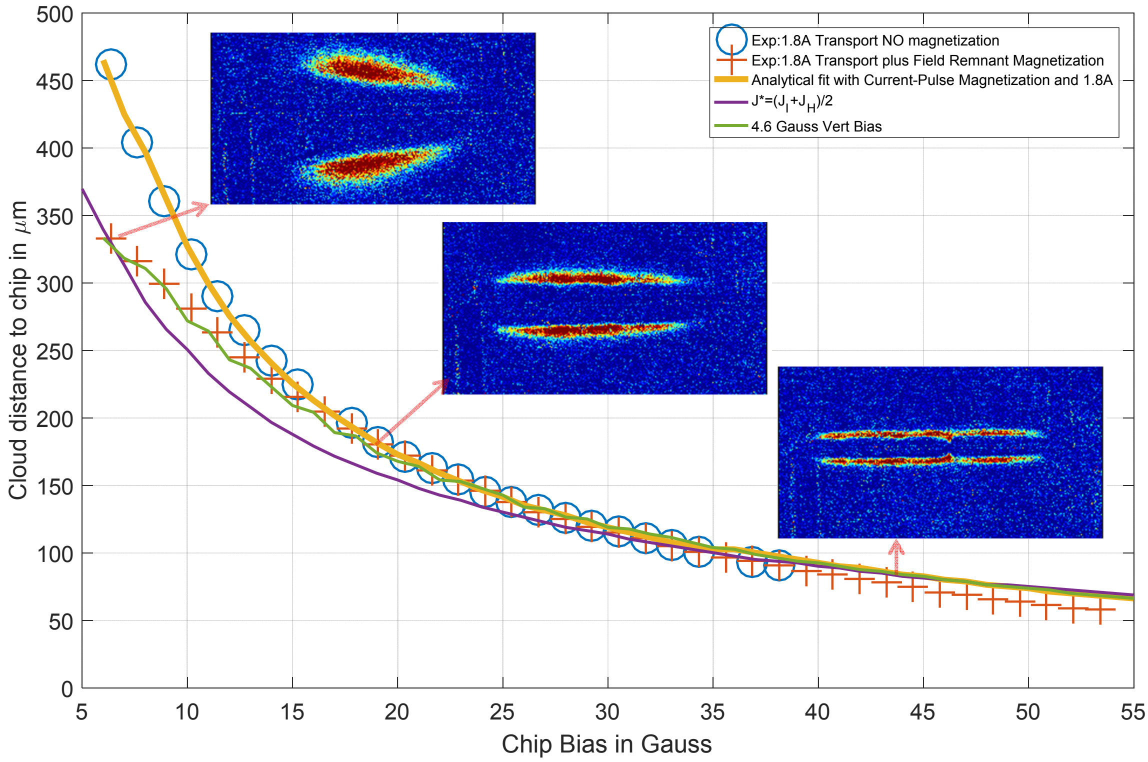

Fig. 7.11 Cloud-to-chip distance versus bias field comparison between non-magnetized (circles) and field-induced magnetized (crosses) niobium atomchip in figure 6.2. A transport current of 1.8 A is applied to create the trap. The inset shows reflection absorption images of the atom cloud trapped in the field-induced trap which can be compared directly to figure 6.3 from the previous chapter. The solid lines are fitting attempts to the experimental data.

atomchip discussed in chapter 5 no longer worked. The loading scheme required an extra perpendicular field (4.6 G) to be ramped up along with transport current.

For a transport current of 1.8 A after field magnetizing the wire, there is a noticeable difference in the cloud-to-chip distance for increasing bias field[8]. The solid yellow curve is a fit using a cross-sectional current density distribution similar to $I_t/Ic = -0.88$ show in figure 7.4b. A similar fit can be done by a simple infinitely thin Biot-Savart wire[9]. The solid violet curve shows the best obtained fit using the model described in section 7.1.1 and shown in figure 7.5. A better fit is obtained by simply adding a 4.6 G homogenous field to the fit of the non-magnetized niobium, which is exactly the same field required in the experiment for loading scheme to work in the field-magnetized

[8]The reflection absorption imaging measures the distance of the cloud to the atomchip. This means that if the trapping trajectory for increasing applied bias field tilts with respect to the z-axis, the distance measured is the z-component of the distance of the trap towards the trapping wire center or simply the distance of the atom cloud towards the atomchip surface.

[9]The physical implications of this behavior will be discussed in great detail in the next section.

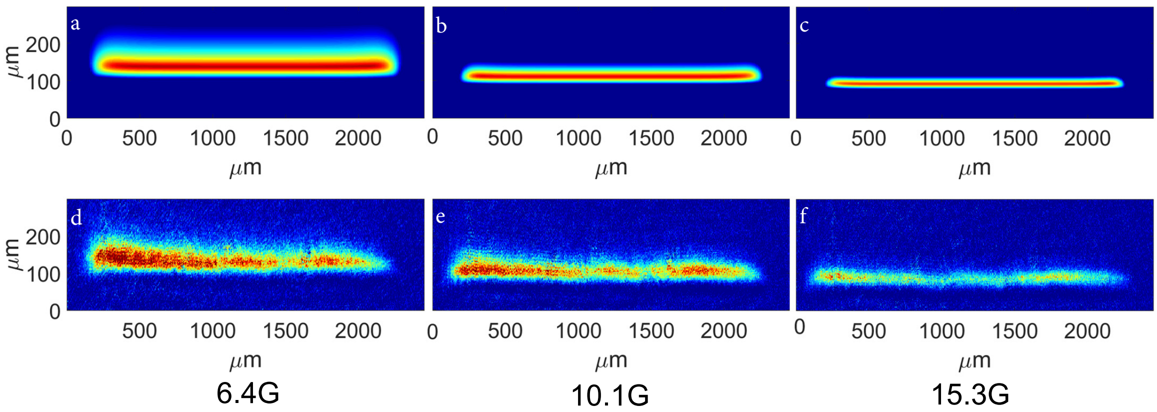

Fig. 7.12 The top row (a-c) shows the potential landscape simulation for a current-induced remnant magnetization trap of the niobium thin film in figure 6.2. The colormap is inverted where red corresponds to the trap bottom and blue clips the colormap to a trap depth of 4 G. The current density distribution cross-section used is shown in figure 7.4 for a current pulse $0 \rightarrow I_{max} \rightarrow 0$. The bottom row (d-f) is a series of absorption imaging measurements in the experiment for exactly the same trap. The applied bias field are 6.4 G, 10.1 G and 15.3 G. The atom cloud temperature is around 50 µK.

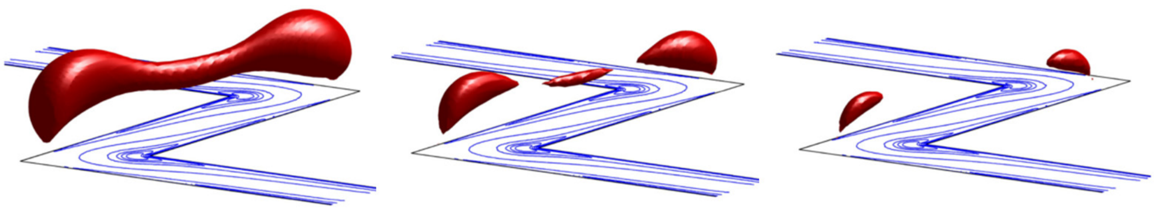

Fig. 7.13 Full 2D Z-wire simulation of a current pulse remnant magnetization trap taken from [143]. The trap depth for the iso-surface is approximately 4 G. The bias field increases from left to right comparably to figure 7.12.

niobium. This is illustrated by the green curve in figure 7.11. This suggests that niobium magnetization is very much current-induced rather than field-induced which is also true for YBCO atomchips. The reflection absorption insets show the atom clouds' physical appearance as the applied bias field is increased. At a low bias fields, there is a clear asymmetry of the atom cloud when compared to the non-field-magnetized niobium (figure 6.3). This indicates that the cross-sectional current density distribution of the wire deviates from the infinite approximation away from the Z-wire center. At close distances, the same magnetic field microscopy features are observed as described in chapter 6.

One of the very peculiar features discussed in the last section of chapter 6 is the existence of an atomchip Z-wire like trap at zero transport current. This feature is clear evidence of a current-induced remnant magnetization trap as discussed in section 7.1.1. Figure 7.12 shows a current-induced remnant magnetization trap for increasing applied bias fields with direct comparison to simulation. The simulation assumes the current-induced magnetization in figure 7.4b where a current pulse $0 \rightarrow I_{max} \rightarrow 0$. In the simulation, I_{max} is set close very close to the critical current, I_c. This kind of trap was briefly discussed in [85] and numerically simulated in full 2D in [143]. In [143], the current-induced remnant trap that was calculated through an energy minimization algorithm which accounts for the Meissner-London currents and as well as the critical state model. The relevant results from paper are shown in figure 7.13 which can be compared directly to figure 7.12. The simpler simulation done using the infinitely long wire model throughout the entire Z-wire cross-section as shown on the top row of figure 7.12 already provides fairly comparable results to the experiment. The atom cloud cloud distance to the chip is nicely replicated, especially the constant distance throughout the Z-wire length. There is also an asymmetry in the atomic density of the current-induced remnant magnetization trap observed suggesting that the trapping potential in the weak direction is slightly asymmetric or deeper on one end. It is not clear whether there is a trap splitting behavior as discussed in [143]. The full numerical simulation suggests that the trap is still highly symmetric along across the Z-wire length and splits into two smaller traps at the edges of the Z-length.

In the experiment, right after a full cool-down of the cryostat, it is standard procedure to test the whether the niobium film is superconducting. This is usually done by applying transport currents and exceeding the critical current (I_c) for niobium which is 2.1 A at 6 K. This usually quenched a part of the entire system. It was initially believed that the niobium film quenched. However, the film still produced a current-induced remnant trap which indicates that it is very likely that the commercial niobium wires soldered to the HT_c wires quenched first. This also means that the measured I_c is not the real critical current of the thin film. This is also confirmed when attempting to quench the niobium film in the attempts of reseting and getting rid of the field-induced remnant magnetization present. There are three temperature sensors mounted on the cage holding all the coils and the atomchip mounting. Two of the sensors are mounted on top of the first and last transport coils and the last one is mounted directly on the 4 K base-plate. The measured values (crosses) in figure 7.11 only disappeared and reverted to the original behavior (circles) when the temperature sensors read ≈50 K. This takes up to an hour of warm up. Since the measured T_c

of the niobium film is 9.2 K, this indicates that the temperature[10] of the atomchip sapphire substrate is taking much longer to rise that the rest of the system[11].

7.3 Tailoring Current Distributions with Current Pulses

From the previous section, it is clear that it is possible to isolate field-induced or current-induced magnetization of the niobium atomchip despite the magnetic fields produced by the magnetic transport. Starting from the virgin state where there is no sheet current present, a remnant magnetization can be induced by ramping the a transport current to a maximum (I_{max}) and back to zero transport current or simply, $0 \rightarrow I_{max} \rightarrow 0$. From the results in equation 7.4 and figure 7.4, even when there is no net transport current, there is still a non-zero sheet current. For a subsequent applied transport current that stays below I_{max} or $I_t \leq |I_{max}|$, the current density distribution across the superconducting film cross-section is always defined by the previous reached highest I_{max}. This makes it possible to tune the current density distribution across the cross-section for a desired transport current, I_t by controlling the previously reached I_{max}. This means that for $I_t \leq |I_{max}|$, there are infinite possible profiles for the distribution in the superconducting film cross-section.

Figure 7.14a shows the different cross-sectional current density distributions for a constant transport current of $I_t = 0.24 I_c$. Just like the field-induced magnetization, this implies that control over the remnant magnetization, which in this case is current-induced, determines how the current density distribution behaves for different transport currents. The polarity of I_{max} affects where majority of the transport current flows. This is illustrated in figure 7.14b where an image map for all infinitely many possibilities of the current distribution along the cross-section. The overall of effect of the tailoring of the cross-sectional current distribution through its previous maximum applied current history is the tuning of the effective width of the wire cross-section. If $I_{max} > I_t$, majority of the current flows around the central region of the wire while on the edges, there are counter-propagating currents. This feature makes the wire appear thinner and in the extreme case infinitely thin. While for $-I_{max} > |I_t|$, majority of the current

[10] At that time, it was very difficult to mount a temperature sensor close to the sapphire substrate on the quartz mounting.

[11] A faster way of quenching the niobium film is by applying a small transport current ($\approx$100 mA) while applying a maximum possible perpendicular field and warming up the cryostat. However, this is highly discouraged since the third time this was attempted resulted into a burnt/cracked sapphire substrate as shown in figure 6.2.

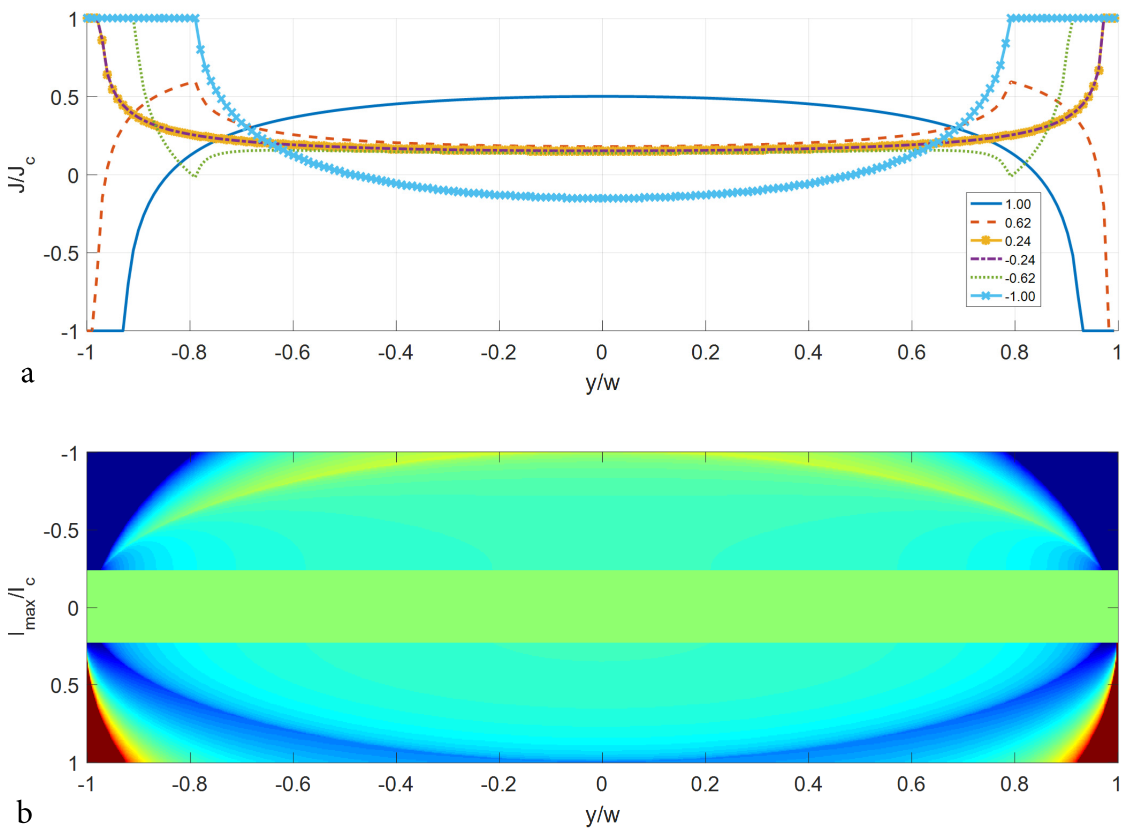

Fig. 7.14 Current-induced magnetization of a rectangular cross-section superconductor: (a), current distribution for across the wire width, w for constant transport current, I_t of $0.24I_c$ for various I_{max} varied from $-I_{max}/I_c \leq I_t \leq I_{max}/I_c$. (b) shows all the possible current density distributions for a transport current of $I_t = 0.24I_c$ where the colorbar scales from $-J_c$ to J_c.

flows at the edges of the wire cross-section, thus making the wire cross-section appear wider. For maximum tunability of the current distribution, transport currents should be much less than the critical current. This will provide a high dynamic range for I_{max}. For desired transport currents close to I_c, the tunability is limited since the distribution is nearly homogeneous across the film cross-section.

In figure 6.8, the zero-current remnant magnetization trap was already presented. As mentioned earlier, the niobium atomchip always experiences an $I_{max} \approx I_c$ right after cooldown. The possibility of being able to tune the current distribution was initially unknown so there was no attempted I_{max} tuning done in order to vary the current density distribution. However, a simple scan of the atom cloud trajectories for increasing applied bias fields for different transport currents already shows evidence of the current-induced remnant magnetization. Figure 7.15 shows an atom cloud-to-chip

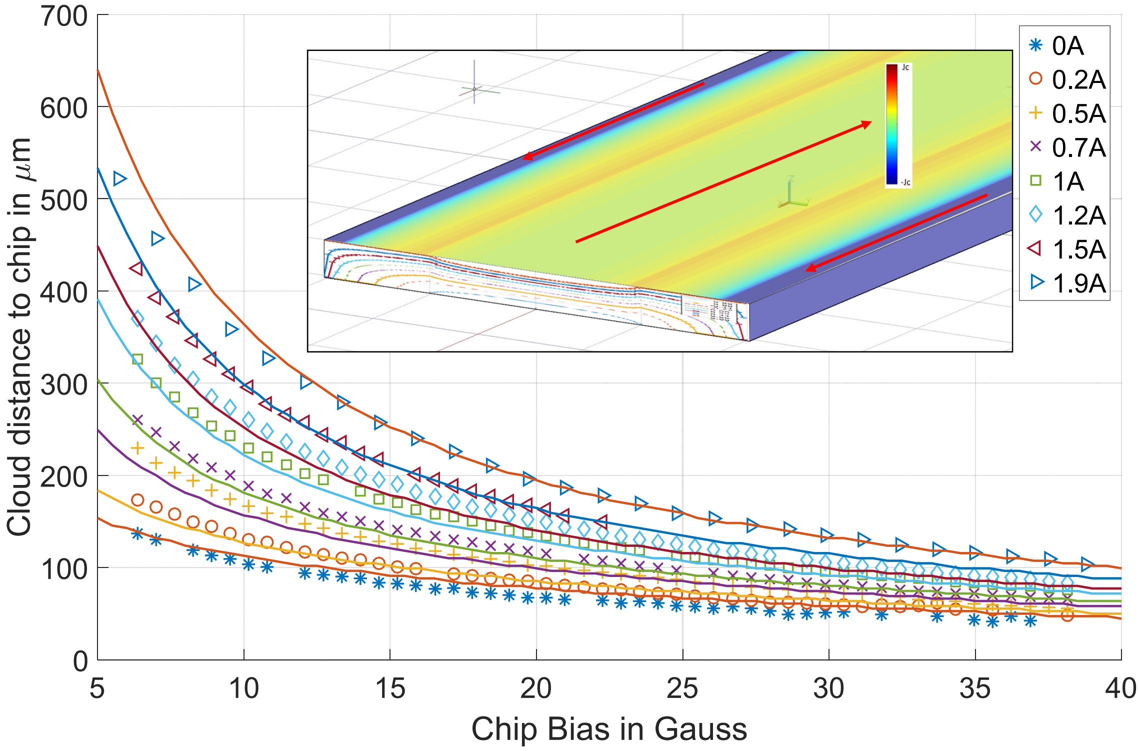

Fig. 7.15 Probing current pulse magnetization in superconductors with ultracold atoms. The discrete markers are experimental measurements of the cloud-to-chip distances versus applied bias field for various currents down to zero transport current. The presence of the zero current trap indicates the presence of remnant magnetization in the superconducting film. The solid curves are fits using the current-memory history assuming the corresponding transport current and a previously reached I_c and I_{max} of 10 A. The inset shows 3D illustration of the film wire cross-section where the top face is a colormap image of the current-induced remnant magnetization. The arrows indicate the direction of the currents at different positions. The cross-section face is overlaid with figure 7.4. This summarizes the current density distribution varies for measurements with different I_t.

distance versus increasing applied bias field for all different possible transport currents. The atomchip trap at $I_t = 0$ is the same trap illustrated in figure 7.12.

The fitted models are obtained from the potential minima calculated in 3D taking into account the 2D film geometry of the niobium atomchip in figure 6.2. A uniform current density distribution for the entire wire cross-section is assumed which is based on the model described in the previous sections. The model fits the experimental data very well for an assumed I_{max} =10 A and I_c =10 A even the zero-current trap at $I_t = 0$. Unfortunately, the assumed I_{max} and I_c are unrealistic values. The critical current of the niobium structure I_c is measured to be about 3.5 A at 4 K and 2.1 A at 6 K which means I_{max} should also be around this value or lower. The assumed condition that $I_{max} \approx I_c$ still holds true.

With the niobium film dimensions of atomchip, the demagnetization effect is estimated to be around 0.9975 [157] which means the the field will be amplified by approximately a factor of 400 at the film edges. Despite this, the atom-cloud trajectories shown in figures 7.15 and 6.8 are moving purely along the z-axis or normal to the film which means that the sheet current on the film is symmetric. Demagnetization effects would mean that the niobium film is also slightly field-magnetized. Although, there is no clear theory to explain the real physics behind the value of I_{max} =10 A and the magnetization of niobium microscopically, the critical state model is still sufficient for a qualitative understanding of the macroscopic behavior of the niobium film. In principle, YBCO should obey the critical state model much better than niobium. The only downside is that there will always be a field-induced magnetization from the magnetic transport. Niobium is still the better choice for the experimental setup. The model assuming an infinitely long rectangular cross-section that includes the critical state fits the transition for a transport current of 1.9 A down to 0 A (current-induced remnant magnetization). Despite the unrealistic assumed value of $I_c = 10\,\mathrm{A}$, the phenomenological model gives a nice macroscopic picture of how superconducting atomchips should be handled. The assumed value of I_c =10 A is the key parameter that fits all the experimental data very well as shown in figures 7.15 and 7.12. The highest possible I_c for the niobium film geometry used according to literature is 5 A. This deviation might be due to the lack of information regarding the superconducting properties of niobium. Niobium is a key superconductor since it lies between type-I and type-II superconductors. There is evidence pointing out the need of modifying or extending the critical state model for niobium [158–160]. However, this is a vast field and is beyond the scope of this thesis.

The results shown in 7.15 and the calculated values plotted in figure 7.14 suggest that the tunability of the current density distribution through the cross-section since it changes the effective width of the niobium wire. This has major implications for future fabrication of niobium atomchips or any other type-II superconducting material. The wire width does not necessarily have to be very small since through current-induced magnetization, the effective width can be controlled through the magnetization history experienced by the superconducting film. The discovery of the current-induced remnant magnetization trap was unintentional. Therefore, no attempts were made to tune the magnetization history of the film (and consequently the effective width of the wire). A key experimental feature is the rapid quenching of the superconducting film in order to reset the superconductor. The easiest way is warming up the superconductor. However, a high power laser (≈2 W) is currently being built in the experiment. The laser shines directly onto the superconducting film and should quench[12] it. Further obtained results especially in current pulse tailoring of the current distribution will be reported in [161, 112].

[12]Upon the writing of this thesis, the current team working on the experiment has succeeded on quenching the niobium film with 1080 nm laser with 1 W of power

Chapter 8

Further Promising Prospects

The last chapter discussed the possibility of being able to control the current density distribution of the superconducting film through magnetization hysteresis behavior. At the start of the superconducting atomchip experiment in the group, the superconducting side of this new atomchip was not fully considered which led to many misunderstood phenomena. This chapter will deal with further promising applications that can be done in this cryogenic atomchip experiment especially in the direction of using superconducting properties to develop new kinds of atomchip designs. There is also a major prospect is in the direction of cavity Quantum Electrodynamics with ^{87}Rb ultracold atoms and superconducting microwave resonators. This topic will be discussed briefly since a major review and progress on the topic will be written in the following thesis of [109].

8.1 Vortices in Supercondutors and Ultracold atoms

The macroscopic effect of vortices in superconductors has been thoroughly studied for atomchip applications in the last chapter. There are only a few experiments in the world that combine superconductors and ultracold atoms. One of the very promising novel applications of superconducting atomchips is to ultimately trap few or single atoms in a single vortex [87]. The experiments done here and in Singapore [84, 81, 85, 83, 74, 100] have so far accounted for the macroscopic effect of vortices i.e. the magnetization currents. The transition from macroscopic traps to microscopic[1] traps with superconductors is rather straightforward. This is done in the same way as ultracold atoms become sensitive to magnetic field fluctuations when brought closer

[1] The terms macroscopic and microscopic are used loosely since in this sense macroscopic is in the vortex length scale ξ typically in the order of nm.

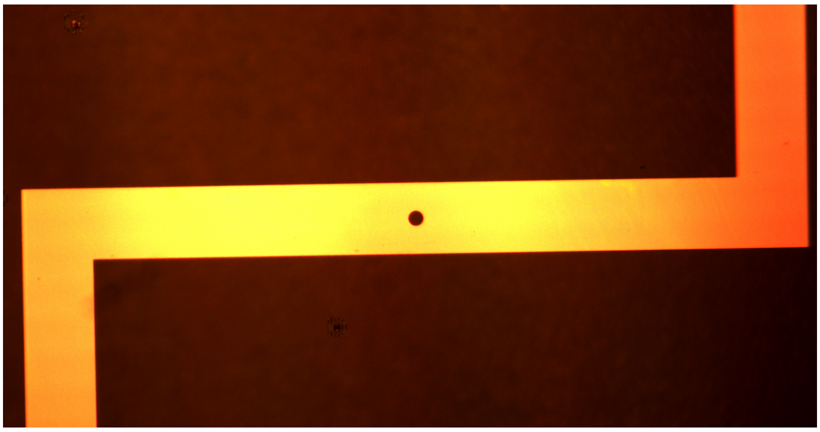

Fig. 8.1 Microscope image of the newly fabricated niobium atomchip with a hole (20 µm in radius). The niobium film is 1 µm thick compared to the old 500 nm old atomchip in figure 6.2. The Z-structure still has the same dimensions 200 µm wide and 2200 µm long. The hole has an estimate ΔB_{freeze} =16.5 mG for a single flux quanta, ϕ_o.

to the trapping wire. Magnetization currents are the net effect of vortices. As colder atomic clouds are brought closer to the trapping structure, they will become sensitive to individual vortices instead of the macroscopic sum of the vortex currents.

8.1.1 Sensing flux quantum ϕ_o with ultracold atoms

Superconducting vortices are quantized super-currents circulating around a normal conducting core. Each vortex carries a quantized flux quanum, $\phi_o = h/2e$. Although the supercurrent is formed by Cooper pairs, it still has a net charge which obeys the Lorenz force. Inside a superconductor, vortices prefers to stay at local minima of the energy landscape in the superconductor. These sites are pinning sites and are sites that allow flux penetration. These are usually defects, impurities, or simply holes in the superconductor. When a superconducting film is fully saturated with vortices, it forms an Abrikosov lattice [89]. This is normally a triangular lattice of about several tens of nm in lattice spacing. This can still vary due to dislocations or the pinning properties in the superconductor. Nowadays, there exist many techniques that allow to shape the pinning landscape of the superconductor with unprecedented control.

Fabricating superconducting films and controlling their pinning properties is a vast field in itself. The small lattice spacings in the Abrikosov lattice make them ideal for creating vortex lattice traps for ultracold atoms. This has the potential of rivaling quantum simulation of condensed matter systems using optical lattices where the lattice spacing is limited by half the lattice laser wavelength (typically 400 nm). With this, previously inaccessible realms in condensed matter physics can be studied [87].

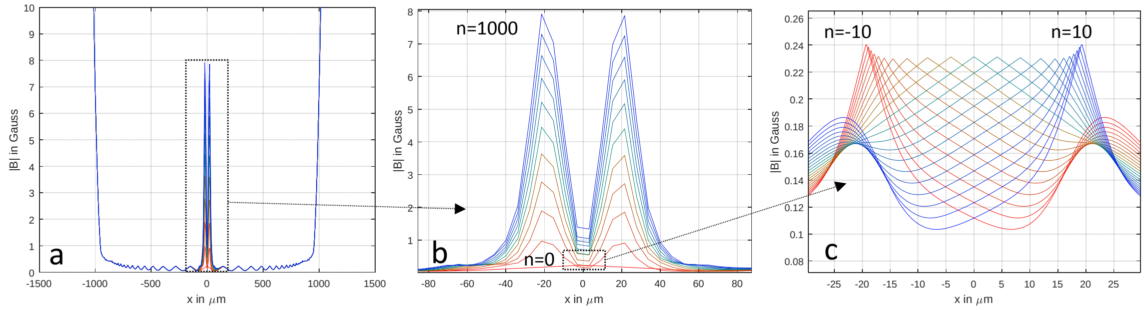

Fig. 8.2 Longitudinal trapping potential for the atomchip with the flux hole in figure 8.1 for a transport current I_t =1.9 A and B_{bias} =120 G with the same current-pulse history in the experimental fits as in figure 7.15. The trap is about 27 µm from the atomchip surface. (a) shows the overall longitudinal potential with the potential distortion from hole in the center. Note that the wiggles at the trap bottom beside the distortion are numerical errors. (b) shows a closer look at the potential distortion caused by the flux hole for $n = 0$ up to $n = 1000$ with increments of 100. (c) An even closer look at the potential distortion from the hole for $n = -10 \rightarrow n = 10$ in steps of $n = 1$.

For superconducting atomchips, the simplest forms of flux pinning can be studied as an initial step to sensing or trapping ultracold atoms in single vortices. The simplest flux pinning method is by introducing holes in the superconducting film. Figure 8.1 shows a new atomchip with a hole in the middle of the Z-structure for flux freezing. Flux can be frozen in the same way as [96]. The appropriate field is applied while $T > T_c$. This creates a flux through the hole, $BA = \Phi$ where A is the area of the hole. Cooling down to below T_c with the applied field should freeze the flux inside the hole. Since the flux penetrating the hole is quantized, $BA = n\phi_o$ where n is the number of trapped flux quanta. The hole in figure 8.1 is 40 µm wide which gives an estimated frozen field of ΔB_{freeze} =16.5 mG for a single ϕ_o.

Figure 8.2 shows the simulation of a how hole carrying n flux quanta can modify the longitudinal potential of the wire-trap. In [162], the flux quanta of a separate ring structure of similar dimensions were detected with ultracold atoms. It was found that the superconducting ring carrying a single flux quantum distorts the trapping potential if the atoms are brought to about 20 µm from the structure. At a trap distance of about 27 µm, an atom cloud colder than 1 µK should also be very sensitive to a single flux quantum trapped in the hole in the niobium structure in figure 8.1.

8.1.2 Lattice traps with superconductors

By structuring holes in superconducting films, lattice traps are very straightforward to make. The goal will be to freeze a strong flux ($n > 1$) in the hole in figure 8.2 that

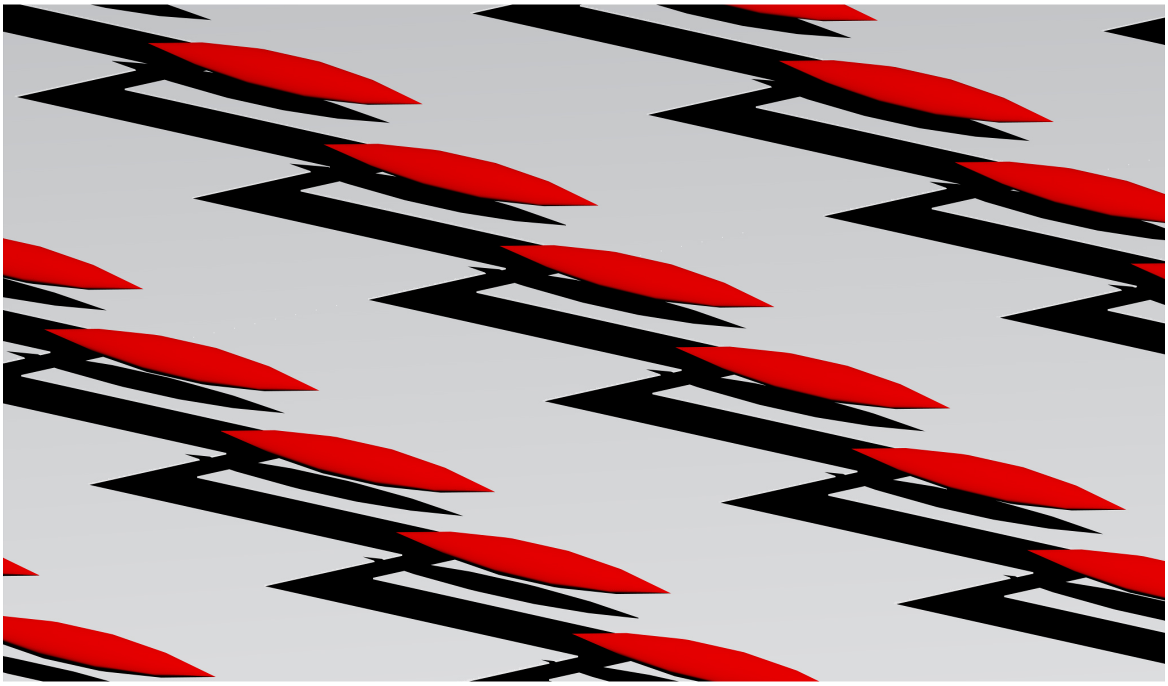

Fig. 8.3 3D rendering of a ladder-like structure that can be fabricated on a superconducting film similar to [163].

can trap atoms with an additional perpendicular field similar to [87, 88]. For niobium, $n \approx 14$ should be possible with the hole in figure 8.2 and even several orders greater for a similar hole in YBCO. The design can be easily extended to many holes with radii that go down close to the vortex size of niobium ($\xi_{Nb} \approx 38\,\mathrm{nm}$) such that each hole is a pinning site for single, or a small number of vortices depending on its size. The holes can be arranged in any desired lattice pattern. Fabricated structures of this length scale should be possible with electron beam lithography.

Instead of holes, lattice traps can also be created by periodic superconducting structures through structured disks or rings. Multiple arrays of periodic magnetized superconducting disks or rings were studied in [88, 143] and were found to create a self-sufficient magnetic lattice trap without the need for an external bias field. Another lattice structure that can also be useful is with ladder-like structures as shown in figure 8.3. Ladder-like structures with sub-micron resolution have already been fabricated and studied using permanent magnets [163, 164]. Unlike permanent magnetic traps where the magnetic film has to be magnetized in a special environment, type-II superconductors bring in a nicer feature of being able to magnetize, re-magnetize, and even reset the superconducting film in the experiment. These ladder-like structures also are basically Z-type traps which means that there will be a non-zero trap bottom, making condensation easier. Since the trapping characteristics are very similar to the permanent magnetic lattices, the same methods from [165, 166] can be applied. Structured superconducting film-based magnetic lattices can extend quantum simulation of condensed matter systems to regimes never before probed in experiments due to their potential to go below optical-lattice spacing [87, 167–169]. Moreover, using superconductors will make this easier and accessible due to the choice of superconductors and its magnetization programmability. Despite the lack of a good microscopic model/theory, the existing macroscopic or phenomenological theories are more than enough for atomchip applications. Interfacing ultracold atomic physics and superconductivity will also open up new possibilities which will require expertise from both fields [87, 170].

8.1.3 Full 2D simulation of type-II superconductors

There are many possible ways to use superconductors for atomchip trapping applications or ultracold atoms to probe superconducting properties. Though simple[2] macroscopic theories were proven to be successful in explaining certain behaviors in superconducting atomchips, as shown in the last chapter, in the long run it will be necessary to do full 2D simulations of the superconducting film. This will provide better insight into the system, especially for the lattice traps discussed in the last section. Despite the demands on computational power of numerical methods, it is worthwhile investing time to understand how the current density distribution of a 2D structure behaves, especially for atomchips containing resonator structures for hybrid quantum system applications. It is still unknown whether the magnetic trap will remain intact in the presence of the Meissner effect of the superconducting resonator. Calculating the Meissner currents for the full geometry can already shed light on this question. The numerical method proposed by [155, 156] is currently being implemented due to its simplicity. It accounts for the critical state model and as well as for Meissner-London effects, so that any magnetic or current history of the system can be calculated for any desired geometry. The method involves minimizing the free energy of the system through iterative variations of an initial magnetization for the desired geometry.

[2]The simple infinitely long wire rectangular film approximation discussed in the last chapter.

8.2 Hybrid Quantum Systems: cQED

As discussed in the first chapter, the initial strong motivation for combining ultracold atoms and superconductivity is to be able to perform hybrid quantum systems experiments. During the course of this thesis, this was pursued in parallel along with studying new superconducting atomchip traps. Lumped element resonators both in niobium and YBCO were fabricated as shown in figure 5.3. Unfortunately, none of the resonators fabricated provided an acceptable resonance. This may be due to the lack of a bounding metal box[3]. Despite the lack of success, this is still being pursued as well as 3D cavities that can provide a larger mode volume with the help of our colleagues [72]. Further developments will be discussed in upcoming theses [109, 171].

[3]The bounding metal box was avoided since atoms need to be loaded into the resonator.

Chapter 9

Summary and Outlook

This thesis laid down the steps and important experimental details that led to the very first superconducting atomchip in the Atominstitut. The magnetic conveyor belt transport including the new vertical design proved to be robust in bringing 3×10^8 ultracold ^{87}Rb atoms into a cryogenic environment. The rapid turn-around time of the design allowed repeated, unrestrained maintenance and upgrade of the Science chamber. The transport design can easily be adapted to a dilution refrigerator system as well as other for use with species[1].

The key feature that had to be accounted for loading into the superconducting Z-structure was the 45° offset between the wire trap and the superconducting quadrupole-Ioffe trap, 3×10^6 atoms at 30 µK were subsequently loaded into the superconducting atomchip [99]. The ultracold atoms were also used as a magnetic field microscope for the niobium trapping structure. These measurements were compared to μHall magnetic field microscopy measurements from the low-temperature group of the Atominstitut [104]. The features observed from the ultracold atoms were found to match the defects in the magnetization measurement of the μHall scan.

Superconducting traps using niobium and YBCO were presented and investigated. Evidence of a Z-wire-like magnetic trap that existed with zero transport current was also presented and found to be caused by a current-induced remnant magnetization. Under the critical state model, the history dependence of the current-induced remnant magnetization was found to greatly influence the current density distribution of the 200 µm-wide niobium trapping wire. This changed the effective width of the trapping wire so that the 200 µm wide wire behaved like an infinitely thin wire. In the future, this can be used to precisely control the current distribution cross-section of the

[1] The strongly dipolar BEC of Dysprosium which has a magnetic dipole moment of $d = 10\mu_B$ will be ideal for the magnetic transport [172, 173].

superconducting trap in order to tailor the effective width of the trapping wire. Niobium magnetization hysteresis behavior was found to be current-dominated, while for YBCO it was found to be more field-dominated. The macroscopic model based on critical state model was found to be sufficient in describing superconducting atomchips [142, 152].

Despite the lack of a proper microscopic theory for type-II superconductors, phenomenological models coupled with good fabrication techniques are sufficient to understand the effects of superconductivity in atomchip trapping. The setup opens up many promising experiments with hybrid quantum systems or new superconducting atomchip traps. There has also been growing interest in superconducting vortex-based lattice traps for ultracold atoms due to the never before accessible potential for quantum simulation of condensed matter systems [87, 167–169]. The key will be to integrate the vast available superconducting fabrication and probing techniques along with ultracold atomic physics technologies where even mechanical control over single vortices at the nanometer scale is possible [174, 175, 170, 176]. For instance, magneto-optic imaging techniques allow time-resolved imaging of vortices and magnetization. These setups are very simple and robust and have already allowed time-resolved imaging of dendritic avalanche effects of vortices [148, 177]. Evidence of dendritic avalanche effects in a superconducting atomchip setting has already been studied [90]. Alternative 2D single-crystal nanostructures of $NbSe_2$ superconduting films might also be promising for atomchip applications due to it being natural defect-free, making vortex control easier [178]. Understanding the interplay of both fields will open up even more hybrid experiments never before possible.

References

[1] Matthias Weidemüller and Claus Zimmermann. *Zeitschrift fuer Physik. D, Atoms, molecules and clusters*. Berli; Heidelberg: Springer, english edition edition, 1997.

[2] Hugh Young and Roger Freedman. *University Physics with Modern Physics*. Pearson, 14th edition, 2012.

[3] G. P. Thomson and A. Reid. Diffraction of Cathode Rays by a Thin Film. , 119:890, June 1927.

[4] L. H. Davisson C. J., Germer. Refelection of electrons by a crystal of Nickel. *Proceedings of the National Academy of Sciences of the USA*, pages 317–322, 1928.

[5] Mark P. Silverman. Neutron Interferometry: Lessons in Experimental Quantum Mechanics, Wave–Particle Duality, and Entanglement. 2nd Ed. By Helmut Rauch and Samuel A. Werner. Oxford University Press, 2015. Price (hardcover) GBP 70. ISBN 978-0-19-871251-0. *Journal of Applied Crystallography*, 48(5):1607–1608, Oct 2015.

[6] Stefan Gerlich, Sandra Eibenberger, Mathias Tomandl, Stefan Nimmrichter, Klaus Hornberger, Paul J Fagan, Jens Tüxen, Marcel Mayor, and Markus Arndt. Quantum interference of large organic molecules. *Nature communications*, 2:263, 2011.

[7] Mark Fox. *Quantum Optics: An Introduction*. Oxford University Press, 1st edition, 2006.

[8] Fritz Diorico. Non-abelian atom optics with ultracold atoms. Master's thesis, Heriot-Watt University, Edinburgh, United Kingdom, 2010.

[9] Barry R. Masters. Satyendra Nath Bose and Bose-Einstein Statistics. *Optics and Photonics, OSA*, pages 41–47, April 2013.

[10] Satyendranath Bose. Planck's law and the light quantum hypothesis, 1994.

[11] Matthias Weidemüller and Claus Zimmermann. *Cold Atoms and Molecules*. WILEY-VCH, 1 edition, 4 2009.

[12] David Andrews. *Structured light and Its Applications*. Elsevier, 1st edition, 2008.

[13] Heike Kamerlingh Onnes. Investigations into the properties of substances at low temperatures , which have led , amongst other things , to the preparation of liquid helium. *Nobel Lecture*, pages 306–336, 1913.

[14] P. Kapitza. Viscosity of Liquid Helium below the λ-Point. , 141:74, January 1938.

[15] J. F. Allen and A. D. Misener. Flow Phenomena in Liquid Helium II. , 142:643–644, October 1938.

[16] David Pines. Richard Feynman and Condensed Matter Physics. *Physics Today*, 42(2):61–66, 1989.

[17] T. H. Maiman. Stimulated Optical Radiation in Ruby. *Nature*, 187(4736):493–494, 1960.

[18] Steven Chu. Nobel lecture: The manipulation of neutral particles. *Rev. Mod. Phys.*, 70:685–706, Jul 1998.

[19] Claude N. Cohen-Tannoudji. Nobel lecture: Manipulating atoms with photons. *Rev. Mod. Phys.*, 70:707–719, Jul 1998.

[20] William D. Phillips. Nobel lecture: Laser cooling and trapping of neutral atoms. *Rev. Mod. Phys.*, 70:721–741, Jul 1998.

[21] E. A. Cornell and C. E. Wieman. Nobel lecture: Bose-einstein condensation in a dilute gas, the first 70 years and some recent experiments. *Rev. Mod. Phys.*, 74:875–893, Aug 2002.

[22] Wolfgang Ketterle. Nobel lecture: When atoms behave as waves: Bose-einstein condensation and the atom laser. *Rev. Mod. Phys.*, 74:1131–1151, Nov 2002.

[23] Alexander D. Cronin, Jörg Schmiedmayer, and David E. Pritchard. Optics and interferometry with atoms and molecules. *Rev. Mod. Phys.*, 81:1051–1129, Jul 2009.

[24] D. W. Keith, M. L. Schattenburg, Henry I. Smith, and D. E. Pritchard. Diffraction of atoms by a transmission grating. *Phys. Rev. Lett.*, 61:1580–1583, Oct 1988.

[25] Coldquanta company page. http://coldquanta.com/. Accessed: 2016-16-08.

[26] Muquans company page. http://www.muquans.com/. Accessed: 2016-16-08.

[27] Robert Bücker, Ulrich Hohenester, Tarik Berrada, Sandrine van Frank, Aurélien Perrin, Stephanie Manz, Thomas Betz, Julian Grond, Thorsten Schumm, and Jörg Schmiedmayer. Dynamics of parametric matter-wave amplification. *Phys. Rev. A*, 86:013638, Jul 2012.

[28] Robert Buecker. *Twin-atom beam generation in a one-dimensional Bose gas*. PhD thesis, Atominstitut TU Wien, Austria, January 2013.

[29] Immanuel Bloch, Jean Dalibard, and Wilhelm Zwerger. Many-body physics with ultracold gases. *Rev. Mod. Phys.*, 80:885–964, Jul 2008.

[30] Immanuel Bloch. Ultracold quantum gases in optical lattices. *Nature Physics*, 1(1):23–30, 2005.

[31] Jae-yoon Choi, Sebastian Hild, Johannes Zeiher, Peter Schauß, Antonio Rubio-Abadal, Tarik Yefsah, Vedika Khemani, David A. Huse, Immanuel Bloch, and Christian Gross. Exploring the many-body localization transition in two dimensions. *Science*, 352(6293):1547–1552, 2016.

[32] J. Ruseckas, G. Juzeliūnas, P. Öhberg, and M. Fleischhauer. Non-abelian gauge potentials for ultracold atoms with degenerate dark states. *Phys. Rev. Lett.*, 95:010404, Jun 2005.

[33] Jean Dalibard, Fabrice Gerbier, Gediminas Juzeliūnas, and Patrik Öhberg. *Colloquium* : Artificial gauge potentials for neutral atoms. *Rev. Mod. Phys.*, 83:1523–1543, Nov 2011.

[34] M. J. Edmonds, M. Valiente, G. Juzeliūnas, L. Santos, and P. Öhberg. Simulating an interacting gauge theory with ultracold bose gases. *Phys. Rev. Lett.*, 110:085301, Feb 2013.

[35] Fabrice Gerbier and Jean Dalibard. Gauge fields for ultracold atoms in optical superlattices. *New Journal of Physics*, 12(3):033007, 2010.

[36] Y-J Lin, R L Compton, K Jiménez-García, J V Porto, and I B Spielman. Synthetic magnetic fields for ultracold neutral atoms. *Nature*, 462(7273):628–32, 2009.

[37] T. Rindler-Daller. Vortices in rotating boseeinstein condensates confined in homogeneous traps. *Physica A: Statistical Mechanics and its Applications*, 387(89):1851 – 1874, 2008.

[38] J. Bardeen, L. N. Cooper, and J. R. Schrieffer. Theory of superconductivity. *Phys. Rev.*, 108:1175–1204, Dec 1957.

[39] Lilia Vitalyevna Yerosheva, Director Dr, and Peter M. Kogge. High-level prototyping for the htmt petaflop machine, 2001.

[40] Mark Keil, Omer Amit, Shuyu Zhou, David Groswasser, Yonathan Japha, and Ron Folman. Fifteen years of cold matter on the atom chip: promise, realizations, and prospects. *Journal of Modern Optics*, 63(18):1840–1885, 2016.

[41] 10 nanometer technology. https://en.wikipedia.org/wiki/10_nanometer. Accessed: 2016-08-01.

[42] John M. Martinis, Michel H. Devoret, and John Clarke. Energy-level quantization in the zero-voltage state of a current-biased josephson junction. *Phys. Rev. Lett.*, 55:1543–1546, Oct 1985.

[43] Caspar H. van der Wal, A. C. J. ter Haar, F. K. Wilhelm, R. N. Schouten, C. J. P. M. Harmans, T. P. Orlando, Seth Lloyd, and J. E. Mooij. Quantum superposition of macroscopic persistent-current states. *Science*, 290(5492):773–777, 2000.

[44] Jonathan R. Friedman, Jonathan R. Friedman, V Patel, V Patel, W Chen, W Chen, Sk Tolpygo, Sk Tolpygo, J. E. Lukens, and J. E. Lukens. Quantum superposition of distinct macroscopic states. *Nature*, 406(6791):43–6, 2000.

[45] Jens Koch, Terri M. Yu, Jay Gambetta, A. A. Houck, D. I. Schuster, J. Majer, Alexandre Blais, M. H. Devoret, S. M. Girvin, and R. J. Schoelkopf. Charge-insensitive qubit design derived from the cooper pair box. *Phys. Rev. A*, 76:042319, Oct 2007.

[46] Vladimir E. Manucharyan, Jens Koch, Leonid I. Glazman, and Michel H. Devoret. Fluxonium: Single cooper-pair circuit free of charge offsets. *Science*, 326(5949):113–116, 2009.

[47] R. Barends, J. Kelly, A. Megrant, D. Sank, E. Jeffrey, Y. Chen, Y. Yin, B. Chiaro, J. Mutus, C. Neill, P. O'Malley, P. Roushan, J. Wenner, T. C. White, A. N. Cleland, and John M. Martinis. Coherent josephson qubit suitable for scalable quantum integrated circuits. *Phys. Rev. Lett.*, 111:080502, Aug 2013.

[48] IBM quantum computing. http://www.research.ibm.com/quantum/. Accessed: 2016-08-01.

[49] R Barends, A Shabani, L Lamata, J Kelly, A Mezzacapo, U Las Heras, R Babbush, G Fowler, B Campbell, Yu Chen, Z Chen, B Chiaro, A Dunsworth, E Jeffrey, E Lucero, A Megrant, J Y Mutus, M Neeley, C Neill, P J J O Malley, C Quintana, P Roushan, A Vainsencher, J Wenner, T C White, E Solano, H Neven, and John M Martinis. Digitized adiabatic quantum computing with a superconducting circuit. *Nature*, 534(7606):222–226, 2016.

[50] Matthew Reagor, Wolfgang Pfaff, Christopher Axline, Reinier W. Heeres, Nissim Ofek, Katrina Sliwa, Eric Holland, Chen Wang, Jacob Blumoff, Kevin Chou, Michael J. Hatridge, Luigi Frunzio, Michel H. Devoret, Liang Jiang, and Robert J. Schoelkopf. Quantum memory with millisecond coherence in circuit qed. *Phys. Rev. B*, 94:014506, Jul 2016.

[51] R. J Schoelkopf and S. M Girvin. Wiring up quantum systems. *Nature*, 451:664–669, Feb 2008.

[52] M Wallquist, K Hammerer, P Rabl, M Lukin, and P Zoller. Hybrid quantum devices and quantum engineering. *Physica Scripta*, 2009(T137):014001, 2009.

[53] Ze-Liang Xiang, Sahel Ashhab, J. Q. You, and Franco Nori. Hybrid quantum circuits: Superconducting circuits interacting with other quantum systems. *Rev. Mod. Phys.*, 85:623–653, Apr 2013.

[54] P. Rabl, D. DeMille, J. M. Doyle, M. D. Lukin, R. J. Schoelkopf, and P. Zoller. Hybrid quantum processors: Molecular ensembles as quantum memory for solid state circuits. *Phys. Rev. Lett.*, 97:033003, Jul 2006.

[55] A. Andre, D. DeMille, J. M. Doyle, M. D. Lukin, S. E. Maxwell, P. Rabl, R. J. Schoelkopf, and P. Zoller. Wiring up quantum systems. *Nature Phys.*, 2:636–642, 2008.

[56] A. S. Sørensen, C. H. van der Wal, L. I. Childress, and M. D. Lukin. Capacitive coupling of atomic systems to mesoscopic conductors. *Phys. Rev. Lett.*, 92:063601, Feb 2004.

[57] D. Petrosyan and M. Fleischhauer. Quantum information processing with single photons and atomic ensembles in microwave coplanar waveguide resonators. *Phys. Rev. Lett.*, 100:170501, Apr 2008.

[58] D. Petrosyan, G. Bensky, G. Kurizki, I. Mazets, J. Majer, and J. Schmiedmayer. Reversible state transfer between superconducting qubits and atomic ensembles. *Phys. Rev. A*, 79:040304, Apr 2009.

[59] J. Verdú, H. Zoubi, Ch. Koller, J. Majer, H. Ritsch, and J. Schmiedmayer. Strong magnetic coupling of an ultracold gas to a superconducting waveguide cavity. *Phys. Rev. Lett.*, 103:043603, Jul 2009.

[60] K. Henschel, J. Majer, J. Schmiedmayer, and H. Ritsch. Cavity qed with an ultracold ensemble on a chip: Prospects for strong magnetic coupling at finite temperatures. *Phys. Rev. A*, 82:033810, Sep 2010.

[61] M. Hafezi, Z. Kim, S. L. Rolston, L. A. Orozco, B. L. Lev, and J. M. Taylor. Atomic interface between microwave and optical photons. *Phys. Rev. A*, 85:020302, Feb 2012.

[62] Simon Bernon, Helge Hattermann, Daniel Bothner, Martin Knufinke, Patrizia Weiss, Florian Jessen, Daniel Cano, Matthias Kemmler, Reinhold Kleiner, Dieter Koelle, and József Fortágh. Manipulation and coherence of ultra-cold atoms on a superconducting atom chip. *Nature commun.*, 4:2380, 2013.

[63] Hua Wu, Richard E. George, Janus H. Wesenberg, Klaus Mølmer, David I. Schuster, Robert J. Schoelkopf, Kohei M. Itoh, Arzhang Ardavan, John J. L. Morton, and G. Andrew D. Briggs. Storage of multiple coherent microwave excitations in an electron spin ensemble. *Phys. Rev. Lett.*, 105:140503, Sep 2010.

[64] D. I. Schuster, A. P. Sears, E. Ginossar, L. DiCarlo, L. Frunzio, J. J. L. Morton, H. Wu, G. A. D. Briggs, B. B. Buckley, D. D. Awschalom, and R. J. Schoelkopf. High-cooperativity coupling of electron-spin ensembles to superconducting cavities. *Phys. Rev. Lett.*, 105:140501, Sep 2010.

[65] Y. Kubo, F. R. Ong, P. Bertet, D. Vion, V. Jacques, D. Zheng, A. Dréau, J.-F. Roch, A. Auffeves, F. Jelezko, J. Wrachtrup, M. F. Barthe, P. Bergonzo, and D. Esteve. Strong coupling of a spin ensemble to a superconducting resonator. *Phys. Rev. Lett.*, 105:140502, Sep 2010.

[66] Atac Imamoğlu. Cavity qed based on collective magnetic dipole coupling: Spin ensembles as hybrid two-level systems. *Phys. Rev. Lett.*, 102:083602, Feb 2009.

[67] J Majer, J M Chow, J M Gambetta, Jens Koch, B R Johnson, J A Schreier, L Frunzio, D I Schuster, A A Houck, A Wallraff, A Blais, M H Devoret, S M Girvin, and R J Schoelkopf. Coupling superconducting qubits via a cavity bus. *Nature*, 449(7161):443–447, 2007.

[68] R. J. Schoelkopf and S. M. Girvin. Wiring up quantum systems. *Nature*, 451(7179):664–669, 2008.

[69] Christian Koller. *Towards teh experimental realization of Hybrid Quantum Systems*. PhD thesis, Atominstitut TU Wien, Austria, January 2012.

[70] G. Kleine Büning, J. Will, W. Ertmer, E. Rasel, J. Arlt, C. Klempt, F. Ramirez-Martinez, F. Piéchon, and P. Rosenbusch. Extended coherence time on the clock transition of optically trapped rubidium. *Phys. Rev. Lett.*, 106:240801, Jun 2011.

[71] R. Folman, P. Krüger, D. Cassettari, B. Hessmo, T. Maier, and J. Schmiedmayer. Controlling cold atoms using nanofabricated surfaces: Atom chips. *Phys. Rev. Lett.*, 84:4749–4752, May 2000.

[72] Andreas Angerer, Thomas Astner, Daniel Wirtitsch, Hitoshi Sumiya, Shinobu Onoda, Junichi Isoya, Stefan Putz, and Johannes Majer. Collective strong coupling with homogeneous rabi frequencies using a 3d lumped element microwave resonator. *Applied Physics Letters*, 109(3), 2016.

[73] Ulrich Hohenester, Asier Eiguren, Stefan Scheel, and E. A. Hinds. Spin-flip lifetimes in superconducting atom chips: Bardeen-cooper-schrieffer versus eliashberg theory. *Phys. Rev. A*, 76:033618, Sep 2007.

[74] R Fermani, T Mller, B Zhang, M J Lim, and R Dumke. Heating rate and spin flip lifetime due to near-field noise in layered superconducting atom chips. *Journal of Physics B: Atomic, Molecular and Optical Physics*, 43(9):095002, 2010.

[75] Nogues, G., Roux, C., Nirrengarten, T., Lupascu, A., Emmert, A., Brune, M., Raimond, J.-M., Haroche, S., Plas, B., and Greffet, J.-J. Effect of vortices on the spin-flip lifetime of atoms in superconducting atom-chips. *EPL*, 87(1):13002, 2009.

[76] Amir Fruchtman and Baruch Horovitz. Single vortex fluctuations in a superconducting chip as generating dephasing and spin flips in cold atom traps. *EPL (Europhysics Letters)*, 99(5):53002, 2012.

[77] C. Hermann-Avigliano, R. Celistrino Teixeira, T. L. Nguyen, T. Cantat-Moltrecht, G. Nogues, I. Dotsenko, S. Gleyzes, J. M. Raimond, S. Haroche, and M. Brune. Long coherence times for rydberg qubits on a superconducting atom chip. *Phys. Rev. A*, 90:040502, Oct 2014.

[78] T. Mukai, C. Hufnagel, A. Kasper, T. Meno, A. Tsukada, K. Semba, and F. Shimizu. Persistent supercurrent atom chip. *Phys. Rev. Lett.*, 98:260407, Jun 2007.

[79] C. Hufnagel. *Superconducting microtraps for ultracold atoms*. PhD thesis, Atominstitut TU Wien / NTT Japan, April 2011.

[80] Christoph Hufnagel, Tetsuya Mukai, and Fujio Shimizu. Stability of a superconductive atom chip with persistent current. *Phys. Rev. A*, 79:053641, May 2009.

[81] B. Zhang, M. Siercke, K. S. Chan, M. Beian, M. J. Lim, and R. Dumke. Magnetic confinement of neutral atoms based on patterned vortex distributions in superconducting disks and rings. *Phys. Rev. A*, 85:013404, Jan 2012.

[82] V. Y. F. Leung, A. Tauschinsky, N. J. Druten, and R. J. C. Spreeuw. Microtrap arrays on magnetic film atom chips for quantum information science. *Quantum Information Processing*, 10(6):955–974, 2011.

[83] T. Müller, B. Zhang, R. Fermani, K. S. Chan, M. J. Lim, and R. Dumke. Programmable trap geometries with superconducting atom chips. *Phys. Rev. A*, 81:053624, May 2010.

[84] M. Siercke, K. S. Chan, B. Zhang, M. Beian, M. J. Lim, and R. Dumke. Reconfigurable self-sufficient traps for ultracold atoms based on a superconducting square. *Phys. Rev. A*, 85:041403, Apr 2012.

[85] B. Zhang, R. Fermani, T. Müller, M. J. Lim, and R. Dumke. Design of magnetic traps for neutral atoms with vortices in type-ii superconducting microstructures. *Phys. Rev. A*, 81:063408, Jun 2010.

[86] V. Dikovsky, V. Sokolovsky, B. Zhang, C. Henkel, and R. Folman. Superconducting atom chips: advantages and challenges. *Eur. J. Phys. D*, 51(2):247–259, Dec 2008.

[87] O. Romero-Isart, C. Navau, A. Sanchez, P. Zoller, and J. I. Cirac. Superconducting vortex lattices for ultracold atoms. *Phys. Rev. Lett.*, 111:145304, Oct 2013.

[88] Vladimir Sokolovsky and Leonid Prigozhin. Lattices of ultracold atom traps over arrays of nano- and mesoscopic superconducting disks. *Journal of Physics D: Applied Physics*, 49(16):165006, 2016.

[89] A. A. Abrikosov. Nobel lecture: Type-ii superconductors and the vortex lattice*. *Rev. Mod. Phys.*, 76:975–979, Dec 2004.

[90] Fujio Shimizu, Christoph Hufnagel, and Tetsuya Mukai. Stable neutral atom trap with a thin superconducting disc. *Phys. Rev. Lett.*, 103:253002, Dec 2009.

[91] Markus Greiner, Immanuel Bloch, Theodor W. Hänsch, and Tilman Esslinger. Magnetic transport of trapped cold atoms over a large distance. *Phys. Rev. A*, 63:031401, Feb 2001.

[92] S. Haslinger, R. Amsüss, C. Koller, C. Hufnagel, N. Lippok, J. Majer, J. Verdu, S. Schneider, and J. Schmiedmayer. Electron beam driven alkali metal atom source for loading a magneto-optical trap in a cryogenic environment. *Applied Physics B*, 102(4):819–823, 2011.

[93] Nils Lippok. A magnetic transport for ultracold atoms. Master's thesis, Atominstitut TU Wien, Austria, 2008.

[94] T. Nirrengarten, A. Qarry, C. Roux, A. Emmert, G. Nogues, M. Brune, J.-M. Raimond, and S. Haroche. Realization of a superconducting atom chip. *Phys. Rev. Lett.*, 97:200405, Nov 2006.

[95] C. Roux, A. Emmert, A. Lupascu, T. Nirrengarten, G. Nogues, M. Brune, J.-M. Raimond, and S. Haroche. Bose-einstein condensation on a superconducting atom chip. *EPL (Europhysics Letters)*, 81(5):56004, 2008.

[96] Hiromitsu Imai, Kensuke Inaba, Haruka Tanji-Suzuki, Makoto Yamashita, and Tetsuya Mukai. Bose–einstein condensate on a persistent-supercurrent atom chip. *Applied Physics B*, 116(4):821–829, 2014.

[97] D. Cano, B. Kasch, H. Hattermann, R. Kleiner, C. Zimmermann, D. Koelle, and J. Fortágh. Meissner effect in superconducting microtraps. *Phys. Rev. Lett.*, 101:183006, Oct 2008.

[98] F. Jessen, M. Knufinke, S. C. Bell, P. Vergien, H. Hattermann, P. Weiss, M. Rudolph, M. Reinschmidt, K. Meyer, T. Gaber, D. Cano, A. Günther, S. Bernon, D. Koelle, R. Kleiner, and J. Fortágh. Trapping of ultracold atoms in a 3he/4he dilution refrigerator. *Applied Physics B*, 116(3):665–671, 2014.

[99] Stefan Minniberger, Fritz Diorico, Stefan Haslinger, Christoph Hufnagel, Christian Novotny, Nils Lippok, Johannes Majer, Christian Koller, Stephan Schneider, and Jörg Schmiedmayer. Magnetic conveyor belt transport of ultracold atoms to a superconducting atomchip. *Applied Physics B*, 116(4):1017–1021, 2014.

[100] T Mller, B Zhang, R Fermani, K S Chan, Z W Wang, C B Zhang, M J Lim, and R Dumke. Trapping of ultra-cold atoms with the magnetic field of vortices in a thin-film superconducting micro-structure. *New Journal of Physics*, 12(4):043016, 2010.

[101] Matthew A. Naides, Richard W. Turner, Ruby A. Lai, Jack M. DiSciacca, and Benjamin L. Lev. Trapping ultracold gases near cryogenic materials with rapid reconfigurability. *Applied Physics Letters*, 103(25), 2013.

[102] S. Haslinger. *Cold Atoms in a Cryogenic Environment*. PhD thesis, Atominstitut TU Wien, Austria, April 2011.

[103] Christian Novotny. Transport of ultracold atoms into a superconducting QuIC-Trap. Master's thesis, Atominsisut Der Oesterreichsichen Universitaeten, TU Wien, Vienna, Austria, 2011.

[104] J. Hecher. *Current Transport in Polycrystallin Iron Based Superconductors*. PhD thesis, Atominstitut TU Wien, January 2016.

[105] J. Dalibard and C. Cohen-Tannoudji. Laser cooling below the doppler limit by polarization gradients: simple theoretical models. *J. Opt. Soc. Am. B*, 6(11):2023–2045, Nov 1989.

[106] D. Sesko, C. G. Fan, and C. E. Wieman. Production of a cold atomic vapor using diode-laser cooling. *J. Opt. Soc. Am. B*, 5(6):1225–1227, Jun 1988.

[107] Steven Chu, L. Hollberg, J. E. Bjorkholm, Alex Cable, and A. Ashkin. Three-dimensional viscous confinement and cooling of atoms by resonance radiation pressure. *Phys. Rev. Lett.*, 55:48–51, Jul 1985.

[108] R. Folman, P. Krüger, J. Schmiedmayer, J. Denschlag, and C. Henkel. Microscopic atom optics: From wires to an atom chip. *Advances In Atomic, Molecular, and Optical Physics*, 48:263–356, Feb 2002.

[109] Stefan Minniberger. *(Tentative)Ultracold Atoms in a Cryogenic Environment.* PhD thesis, Atominstitut TU Wien, Austria, October 2016.

[110] Robert Amsuess. Development of a Source of Ultracold Atoms for Cryogenic Environments. Master's thesis, Atominsisut Der Oesterreichsichen Universitaeten, TU Wien, Vienna, Austria, 2008.

[111] David A. Smith, Simon Aigner, Sebastian Hofferberth, Michael Gring, Mauritz Andersson, Stefan Wildermuth, Peter Krüger, Stephan Schneider, Thorsten Schumm, and Jörg Schmiedmayer. Absorption imaging of ultracold atoms on atom chips. *Opt. Express*, 19(9):8471–8485, Apr 2011.

[112] Benedikt Gerstenecker. TBA. Master's thesis, Atominsisut Der Oesterreichsichen Universitaeten, TU Wien, Vienna, Austria, 2017.

[113] Qi Liang. *Tentative: Superior Experimental Control over Quantum Relaxation setups.* PhD thesis, Atominstitut TU Wien, Austria, April 2019.

[114] Aurélien Perrin, Robert Bücker, Stephanie Manz, Thomas Betz, Christian Koller, Thomas Plisson, Thorsten Schumm, and Jörg Schmiedmayer. Hanbury Brown and Twiss correlations across the Bose-Einstein condensation threshold. *Nature Physics*, 8(3):195–198, 2010.

[115] R. Amsüss, Ch. Koller, T. Nöbauer, S. Putz, S. Rotter, K. Sandner, S. Schneider, M. Schramböck, G. Steinhauser, H. Ritsch, J. Schmiedmayer, and J. Majer. Cavity qed with magnetically coupled collective spin states. *Phys. Rev. Lett.*, 107:060502, Aug 2011.

[116] Wolfgang Rohringer. *Dynamics of One-Dimensional Bose Gases in Time-Dependent Traps.* PhD thesis, Atominstitut TU Wien, Austria, April 2014.

[117] Stephan Schneider. *Bose-Einstein Kondensation in einer magnetischen Z-Falle.* PhD thesis, Atominstitut TU Wien, Austria, July 2003.

[118] T. Esslinger, I. Bloch, and T. W. Hänsch. Bose-einstein condensation in a quadrupole-ioffe-configuration trap. *Phys. Rev. A*, 58:R2664–R2667, Oct 1998.

[119] David E. Pritchard. Cooling neutral atoms in a magnetic trap for precision spectroscopy. *Phys. Rev. Lett.*, 51:1336–1339, Oct 1983.

[120] Wolfgang Ketterle and N.J. Van Druten. Evaporative cooling of trapped atoms. volume 37 of *Advances In Atomic, Molecular, and Optical Physics*, pages 181 – 236. Academic Press, 1996.

[121] Jakob Reichel and Vladan Vuletic. *Atom Chips.* WILEY-VCH, Berlin, 1 edition, February 2011.

[122] S. Groth, P. Krger, S. Wildermuth, R. Folman, T. Fernholz, J. Schmiedmayer, D. Mahalu, and I. Bar-Joseph. Atom chips: Fabrication and thermal properties. *Applied Physics Letters*, 85(14), 2004.

[123] James R. B. Garfield. Superconducting contacts for use in niobium thin film applications. *Review of Scientific Instruments*, 68(4), 1997.

[124] Torsten Henning. *Coulomb blockade effects in anodised niobium nanostructures.* 1997.

[125] S. Hofferberth, B. Fischer, T. Schumm, J. Schmiedmayer, and I. Lesanovsky. Ultracold atoms in radio-frequency dressed potentials beyond the rotating-wave approximation. *Phys. Rev. A*, 76:013401, Jul 2007.

[126] T. Schumm, J. Estève, C. Figl, J.-B. Trebbia, C. Aussibal, H. Nguyen, D. Mailly, I. Bouchoule, I. C. Westbrook, and A. Aspect. Atom chips in the real world: the effects of wire corrugation. *The European Physical Journal D - Atomic, Molecular, Optical and Plasma Physics*, 32(2):171–180, 2005.

[127] J. Estève, C. Aussibal, T. Schumm, C. Figl, D. Mailly, I. Bouchoule, C. I. Westbrook, and A. Aspect. Role of wire imperfections in micromagnetic traps for atoms. *Phys. Rev. A*, 70:043629, Oct 2004.

[128] Stephan Wildermuth, Sebastian Hofferberth, Igor Lesanovsky, Elmar Haller, L. Mauritz Andersson, Sönke Groth, Israel Bar-Joseph, Peter Krüger, and Jörg Schmiedmayer. Microscopic magnetic-field imaging. 435(May):435440, 2005.

[129] S. Wildermuth, S. Hofferberth, I. Lesanovsky, S. Groth, P. Krger, J. Schmiedmayer, and I. Bar-Joseph. Sensing electric and magnetic fields with bose-einstein condensates. *Applied Physics Letters*, 88(26), 2006.

[130] P. Krüger, L. M. Andersson, S. Wildermuth, S. Hofferberth, E. Haller, S. Aigner, S. Groth, I. Bar-Joseph, and J. Schmiedmayer. Potential roughness near lithographically fabricated atom chips. *Phys. Rev. A*, 76:063621, Dec 2007.

[131] S. Aigner, L. Della Pietra, Y. Japha, O. Entin-Wohlman, T. David, R. Salem, R. Folman, and J. Schmiedmayer. Long-range order in electronic transport through disordered metal films. *Science*, 319(5867):1226–1229, 2008.

[132] Ernst Helmut Brandt and Grigorii P. Mikitik. Meissner-london currents in superconductors with rectangular cross section. *Phys. Rev. Lett.*, 85:4164–4167, Nov 2000.

[133] Will Turner, Shenglan Qiao, Josh Straquadine, Jack Disciacca, and Benjamin L Lev. A Scanning Quantum Cryogenic Atom Microscope. 94305(1):1–16, 2015.

[134] F Hengstberger, M Eisterer, M Zehetmayer, and H W Weber. Assessing the spatial and field dependence of the critical current density in ybco bulk superconductors by scanning hall probes. *Superconductor Science and Technology*, 22(2):025011, 2009.

[135] M Lao, M Eisterer, O Stadel, A Meledin, and G van Tendeloo. The effect of y 2 o 3 and yfeo 3 additions on the critical current density of ybco coated conductors. *Journal of Physics: Conference Series*, 507(2):022012, 2014.

[136] M Lao, J Bernardi, M Bauer, and M Eisterer. Critical current anisotropy of gdbco tapes grown on isdmgo buffered substrate. *Superconductor Science and Technology*, 28(12):124002, 2015.

[137] C. P. Bean. Magnetization of hard superconductors. *Phys. Rev. Lett.*, 8:250–253, Mar 1962.

[138] Ch. Jooss, R. Warthmann, A. Forkl, and H. Kronmller. High-resolution magneto-optical imaging of critical currents in yba2cu3o7?? thin films. *Physica C: Superconductivity*, 299(34):215 – 230, 1998.

[139] Bradley J. Roth, Nestor G. Sepulveda, and John P. Wikswo. Using a magnetometer to image a two-dimensional current distribution. *Journal of Applied Physics*, 65(1):361–372, 1989.

[140] Xiao-Guang Lv and Ting-Zhu Huang. A note on inversion of toeplitz matrices. *Applied Mathematics Letters*, 20(12):1189 – 1193, 2007.

[141] john cunningham and william zhang. Toeblitz toolkit for fast toeplitz matrix operations, 2014. http://mloss.org/software/view/496/.

[142] EH Brandt and Mikhail Indenbom. Type-II-superconductor strip with current in a perpendicular magnetic field. *Physical review B*, 48(17), 1993.

[143] Vladimir Sokolovsky, Daniel Rohrlich, and Baruch Horovitz. Trapping neutral atoms in the field of a vortex pinned by a superconducting nanodisk. *Phys. Rev. A*, 89:053422, May 2014.

[144] Peter Schmüser. Superconductivity. *Lecture Course*.

[145] A P Drozdov, M I Eremets, I A Troyan, V Ksenofontov, and S I Shylin. Conventional superconductivity at 203 kelvin at high pressures in the sulfur hydride system. *Nature*, 525(7567):73–76, 2015.

[146] Lev Gorkov. Developing BCS ideas in the former Soviet Union. *arXiv*, 1102.1098:1–20, 2011.

[147] M Cyrot. Ginzburg-Landau theory for superconductors. *Reports on Progress in Physics*, 36(2):103–158, 1973.

[148] PErik Goa, Harald Hauglin, Michael Baziljevich, Eugene Il'yashenko, Peter L Gammel, and Tom H Johansen. Real-time magneto-optical imaging of vortices in superconducting nbse 2. *Superconductor Science and Technology*, 14(9):729, 2001.

[149] Charles P. Bean. Magnetization of high-field superconductors. *Rev. Mod. Phys.*, 36:31–39, Jan 1964.

[150] J. A. Thompson. Characterization of niobium films and a bulk niobium sample with rrr, sims and a squid magnetometer. *Journal of Undergraduate Research.*

[151] A. Emmert, A. Lupaşcu, M. Brune, J.-M. Raimond, S. Haroche, and G. Nogues. Microtraps for neutral atoms using superconducting structures in the critical state. *Phys. Rev. A*, 80:061604, Dec 2009.

[152] E. Zeldov, John R. Clem, M. McElfresh, and M. Darwin. Magnetization and transport currents in thin superconducting films. *Phys. Rev. B*, 49:9802–9822, Apr 1994.

[153] Ruixing Liang, D. A. Bonn, W. N. Hardy, and David Broun. Lower critical field and superfluid density of highly underdoped $\mathrm{yba}_2\mathrm{cu}_3\mathrm{o}_{6+x}$ single crystals. *Phys. Rev. Lett.*, 94:117001, Mar 2005.

[154] R.A. French. Intrinsic type-2 superconductivity in pure niobium. *Cryogenics*, 8(5):301 – 308, 1968.

[155] Guillem Via, Carles Navau, and Alvaro Sanchez. Magnetic and transport currents in thin film superconductors of arbitrary shape within the london approximation. *Journal of Applied Physics*, 113(9), 2013.

[156] Guillem Via, Nuria Del-Valle, Alvaro Sanchez, and Carles Navau. Simultaneous magnetic and transport currents in thin film superconductors within the critical-state approximation. *Superconductor Science and Technology*, 28(1):014003, 2015.

[157] Du-Xing Chen, E. Pardo, and A. Sanchez. Demagnetizing factors of rectangular prisms and ellipsoids. *IEEE Transactions on Magnetics*, 38(4):1742–1752, Jul 2002.

[158] Ruslan Prozorov, Daniel V. Shantsev, and Roman G. Mints. Collapse of the critical state in superconducting niobium. *Phys. Rev. B*, 74:220511, Dec 2006.

[159] E.A. Gijsbertse and L.J.M. van de Klundert. Deviations from the critical state model observed in niobium. *Physics Letters A*, 77(5):335 – 337, 1980.

[160] A E Youssef, Z Švindrych, J Hada, and Z Jan. Critical State in Nb Thin Film. *WDS'07 Proceedings of Contributed Papers*, pages 48–53, 2007.

[161] Fritz Diorico, Stefan Minniberger, and Joerg Schmiedmayer. Tailored transport current distributions in superconducting atomchips. *ArXiV paper in prepartion*, 2016.

[162] P. Weiss, M. Knufinke, S. Bernon, D. Bothner, L. Sárkány, C. Zimmermann, R. Kleiner, D. Koelle, J. Fortágh, and H. Hattermann. Sensitivity of Ultracold Atoms to Quantized Flux in a Superconducting Ring. *Physical Review Letters*, 114(11):113003, March 2015.

[163] I Herrera, Y Wang, P Michaux, D Nissen, P Surendran, S Juodkazis, S Whitlock, R J McLean, A Sidorov, M Albrecht, and P Hannaford. Sub-micron period lattice structures of magnetic microtraps for ultracold atoms on an atom chip. *Journal of Physics D: Applied Physics*, 48(11):115002, 2015.

[164] R. Gerritsma, S. Whitlock, T. Fernholz, H. Schlatter, J. A. Luigjes, J.-U. Thiele, J. B. Goedkoop, and R. J. C. Spreeuw. Lattice of microtraps for ultracold atoms based on patterned magnetic films. *Phys. Rev. A*, 76:033408, Sep 2007.

[165] Roman Schmied, Dietrich Leibfried, Robert J C Spreeuw, and Shannon Whitlock. Optimized magnetic lattices for ultracold atomic ensembles. *New Journal of Physics*, 12(10):103029, 2010.

[166] S Whitlock, R Gerritsma, T Fernholz, and R J C Spreeuw. Two-dimensional array of microtraps with atomic shift register on a chip. *New Journal of Physics*, 11(2):023021, 2009.

[167] Jinlong Yu, Zhi-Fang Xu, Rong Lü, and Li You. Dynamical generation of topological magnetic lattices for ultracold atoms. *Phys. Rev. Lett.*, 116:143003, Apr 2016.

[168] Michael E. Beverland, Gorjan Alagic, Michael J. Martin, Andrew P. Koller, Ana M. Rey, and Alexey V. Gorshkov. Realizing exactly solvable SU(n) magnets with thermal atoms. *Phys. Rev. A*, 93:051601, May 2016.

[169] Vitaly Lutsky and Boris A. Malomed. One- and two-dimensional solitons supported by singular modulation of quadratic nonlinearity. *Phys. Rev. A*, 91:023815, Feb 2015.

[170] Jun-Yi Ge, Vladimir N. Gladilin, Cun Xue, Jacques Tempere, Jozef T. Devreese, Joris Van de Vondel, Youhe Zhou, and Victor V. Moshchalkov. Magnetic dipoles at topological defects in the meissner state of a nanostructured superconductor. *Phys. Rev. B*, 93:224502, Jun 2016.

[171] Naz Shokrani. TBA. Master's thesis, Atominsisut Der Oesterreichsichen Universitaeten, TU Wien, Vienna, Austria, 2017.

[172] Yijun Tang, Nathaniel Q. Burdick, Kristian Baumann, and Benjamin L. Lev. Bose-Einstein condensation of 162Dy and 160Dy. *New Journal of Physics*, 17(4):045006, 2015.

[173] Mingwu Lu, Nathaniel Q. Burdick, Seo Ho Youn, and Benjamin L. Lev. Strongly dipolar bose-einstein condensate of dysprosium. *Phys. Rev. Lett.*, 107:190401, Oct 2011.

[174] Anna Kremen, Shai Wissberg, Noam Haham, Eylon Persky, Yiftach Frenkel, and Beena Kalisky. Mechanical Control of Individual Superconducting Vortices. *Nano Letters*, 16(3):1626–1630, 2016.

[175] L Embon, Y Anahory, A Suhov, D Halbertal, J Cuppens, A Yakovenko, A Uri, Y Myasoedov, M L Rappaport, M E Huber, A Gurevich, and E Zeldov. Probing dynamics and pinning of single vortices in superconductors at nanometer scales. *Scientific Reports*, 5:7598, 2015.

[176] Alexander Volodin, Kristiaan Temst, Chris Van Haesendonck, and Yvan Bruynseraede. Imaging of vortices in conventional superconductors by magnetic force microscopy. *Physica C: Superconductivity*, 332(14):156 – 159, 2000.

[177] E. Altshuler and T. H. Johansen. *Colloquium* : Experiments in vortex avalanches. *Rev. Mod. Phys.*, 76:471–487, Apr 2004.

[178] Y. Liu. *Superconductivity and vortex dynamics in nanostructures of two-dimensional crystals of niobium diselenide*. PhD thesis, Eberly Colloge of Science, The Pennsylvania State University, August 2016.

[179] Daniel A. Steck. Rubidium87 d line data 2010. 2010.

Nomenclature

Abbreviations

AOM	Acousto Optic Modulator
BCS	Bardeen-Cooper-Schrieffer
BEC	Bose-Einstein Condensate
CAD	Computer Animater Drawing
cQED	Cavity Quantum Electrodyanamics
DFB	Distributed Feedback laser
ECDL	External Cavicty Diode Laser
FM	Frequency-Modulation
FO	Frequency-Offset
GL	Ginzburg-Landau
MOT	Magneto-Optical Trap
NC	Normal Conducting
PBS	Polarization Beam Splitter
PC	Personal Computer
QUIC	quadrupole-Ioffe
RMS	Root-Mean-Squared
SC	Superconducting
SMA	SubMiniature version A
TOF	Time of Flight
UHV	Ultra High Vacuum

List of Symbols

Δp	The uncertainty of the momentum of a particle
Δx	The uncertainty of the position of a particle
$\hbar$	The reduced Planck's constant, $h/2\pi$
λ_{deB}	De Broglie wavelength
μ_B	Bohr magneton
μ_o	Magnetic permeability

π	π, circumference of a circle divided by its diameter
π'	Linear polarization of light
σ_+	Right-handed circularly polarization of light
σ_-	Left-handed circularly polarization of light
B	Magnetic induction where $\mu_o H = B$.
B_{bias}	Applied bias field to create the atomchip trap,
B_{Ioffe}	Ioffe bias field
B_{vert}	Vertical bias field
d	Thickness of the superconducting film
F	Rubidium Hyperfine levels
H	Magnetic field.
h	The Planck's constant
H_a	Applied magnetic field, perpendicular to the superconducting film
H_c	Thermodynamic critical field
H_{c1}	First critical field of a type-II superconductor
H_{c2}	Second critical field of a type-II superconductor
I_{chip}	Z-wire applied transport current
I_c	Critical current of the superconducting structure. For the bare cross-section of the superconducting film, this is $2wdJ_c$.
I_{Ioffe}	Current in the Ioffe coil
I_{quad}	Transport current in the final superconducting quadruople trap
J	Current density of a superconductor in units of current per cross-sectional area. In the case of equations (7.3), (7.2) and similar equations, the current density (J) is calculated for every position along the cross-section. For every point (y), J is defined by the discrete area which is the $d\Delta y$ where d is the thickness of the thin film and $d\Delta y$ is the step length chosen for discretization.
J_c	Critical current density of a superconductor in units of current per cross-sectional area
k_B	Boltzmann constant
m_F	Zeeman Hyperfine sublevels
T	Temperature
T_c	Critical temperature either for superconductivity or Bose-Einstein Condensate depending on the context.
T_D	Doppler limit temperature
T_R	Recoil limit temperature

w	Half width of the Z-wire structure

Appendix A

Transition Dipole Moment

For nearly resonant optical radiation, the interaction strength of the D1 and D2 line of Rubidium 87 is characterized by the dipole matrix elements. The transitions follow the selection rules follow $\Delta m_F = -1$, $\Delta m_F = 0$, and $\Delta m_F = 1$ for σ^-, π, and σ^+ polarized light, respectively. Figures A.1, A.2 and A.3 show the entire D2, $780.241nm$ line transitions with the corresponding relative transition strengths normalized to the weakest transition. The results shown on the figures are taken from [179].

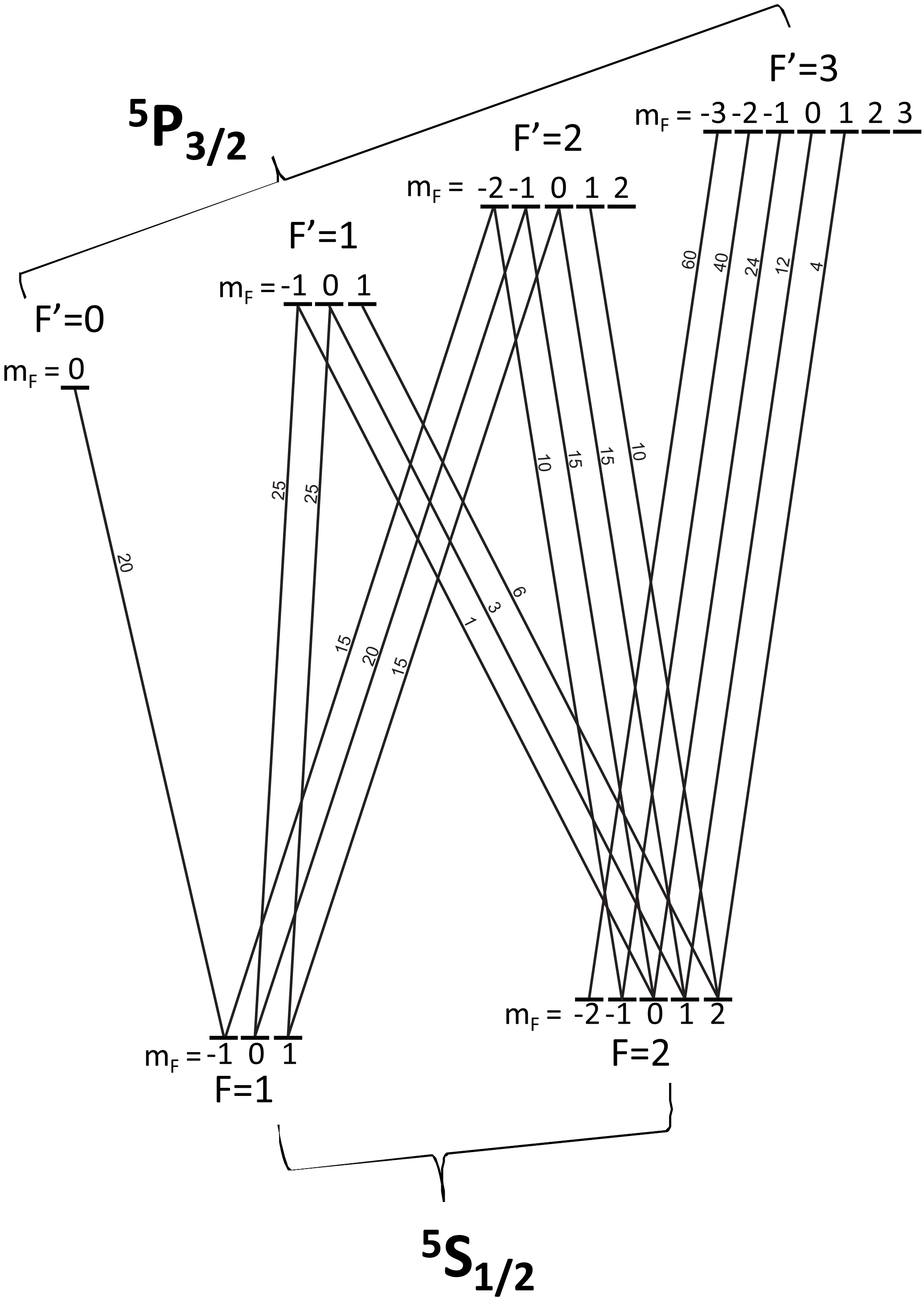

Fig. A.1 Complete energy level scheme with relative transition strengths for the D2 line of Rubidium 87 for σ^- polarization.

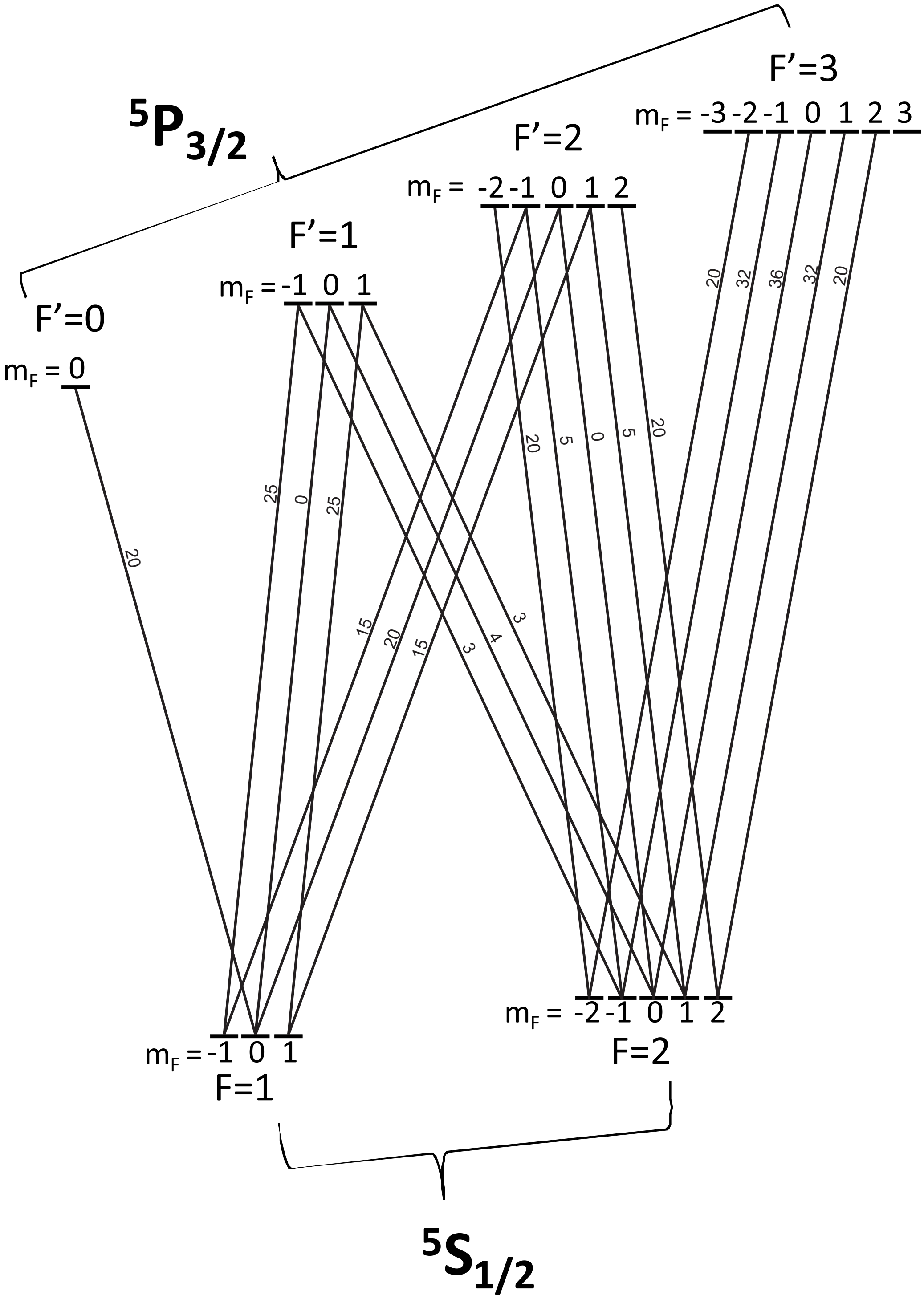

Fig. A.2 Complete energy level scheme with relative transition strengths for the D2 line of Rubidium 87 for π polarization.

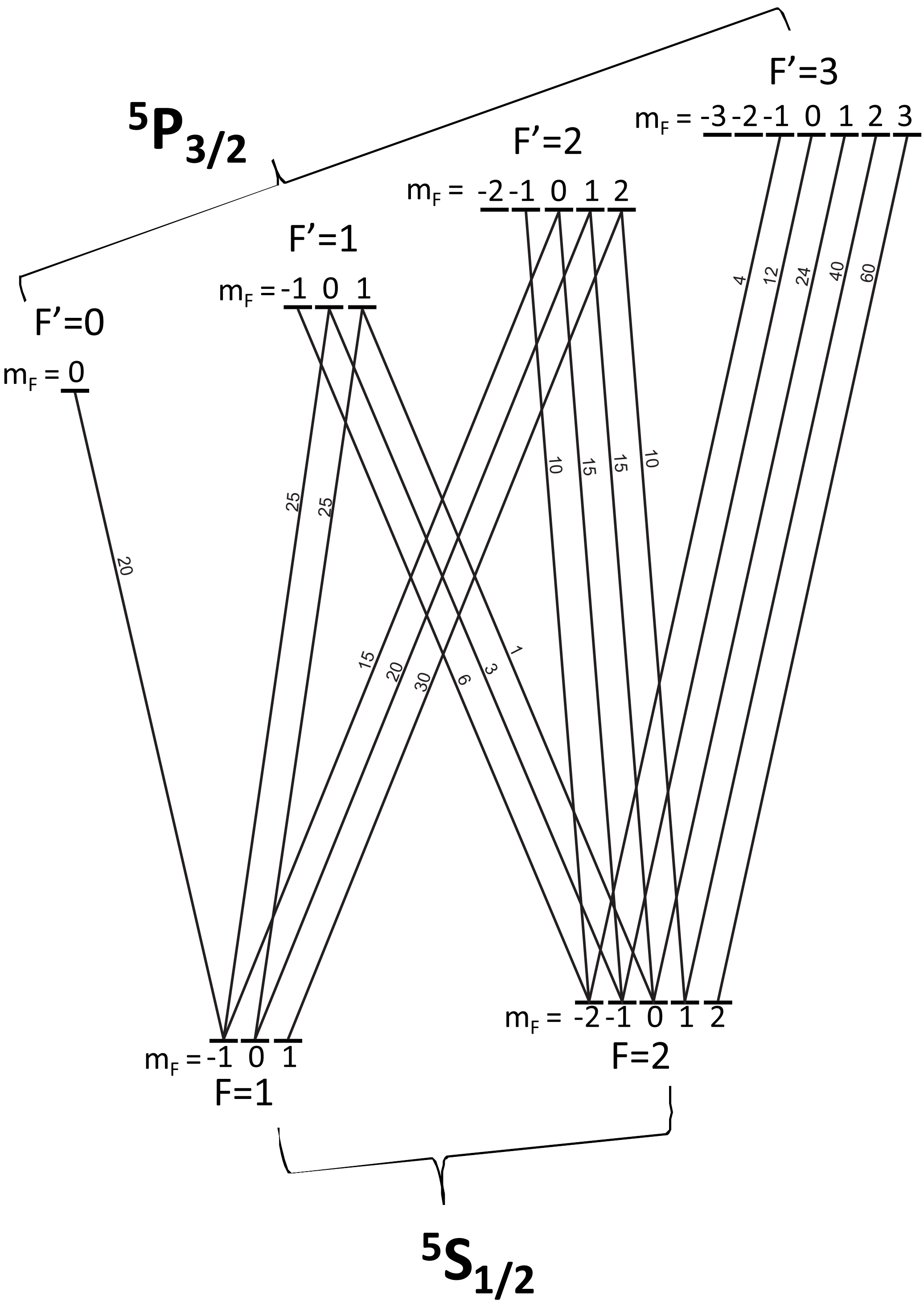

Fig. A.3 Complete energy level scheme with relative transition strengths for the D2 line of Rubidium 87 for σ^+ polarization.

Appendix B

Current Electronics and Laser Optics

Figure B.1 the power splitter originally intended to connect the quadrupole-Ioffe trap in series. The non-linear behavior proved very unstable for practical use. Figure B.2 shows the full TOF movie of the quadrupole-Ioffe trap. The random motion due to the massive induction fields can be observed. Figure B.3 shows the fastest possible switch off achieved of the quadrupole-Ioffe trap. Figure B.4 shows the laser setup built for the alternative optical pumping.

Fig. B.1 Power splitter built by the Atominstitut electronics workshop.

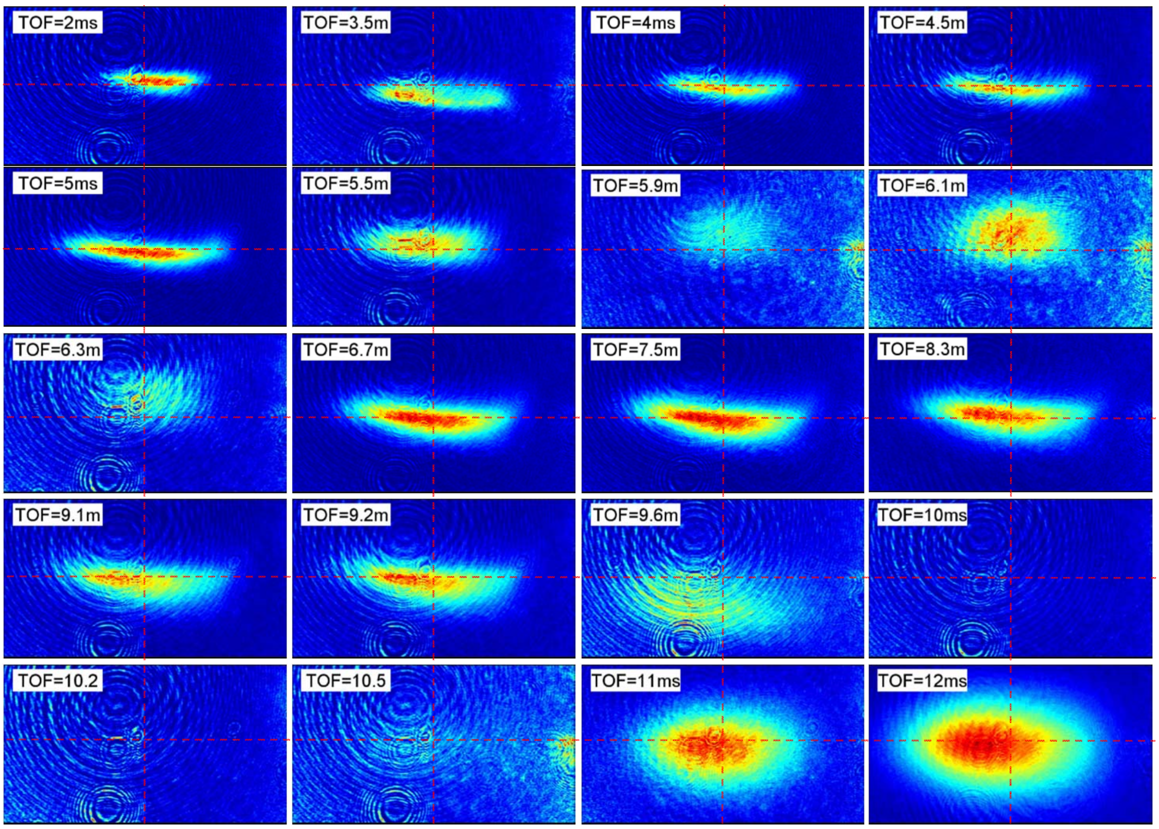

Fig. B.2 Time of Flight (TOF) movie snapshot of the QUIC trap. A full movie is available by request or in the atomchip server.

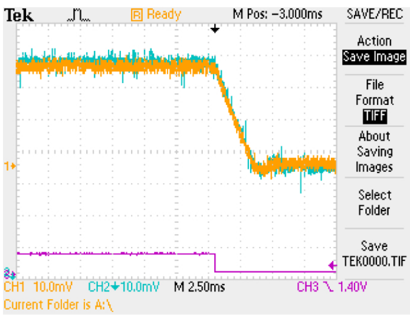

Fig. B.3 Switch off.

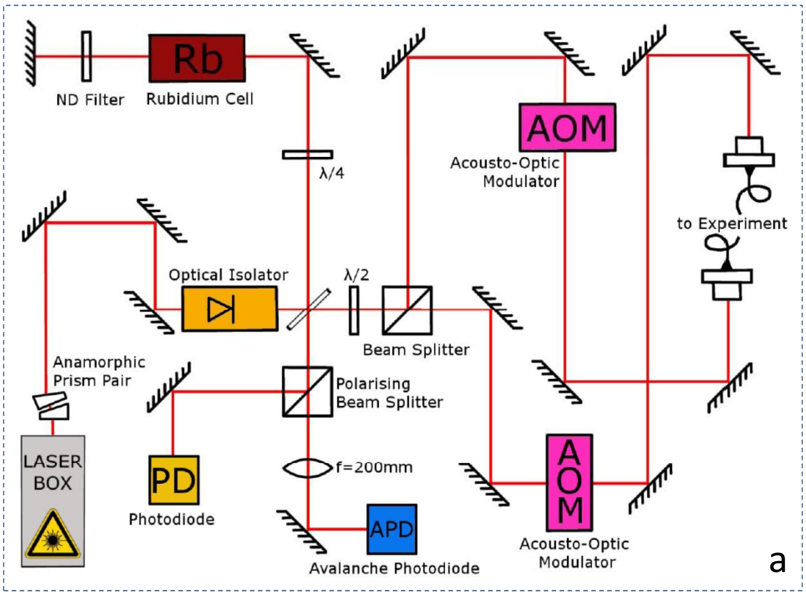

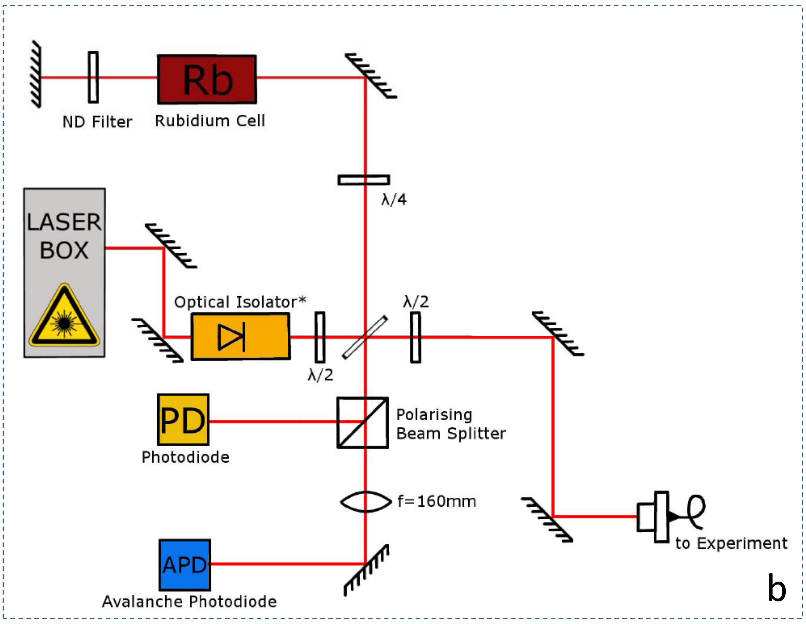

Fig. B.4 DFB setup for the rempumping line (a) and the ECDL setup for the regular optical pumping line (b).

Appendix C

UHV and Cryostat

It is possible to revive ultra high vacuum of the MOT chamber in about 1-2 weeks. This is important in case if the Rubidium dispenser needs to be replaced. Assuming a spare Rubidium dispenser is already attached to the high current feed-through, the old dispenser can be replaced easily. A turbo pump can be attached to the pumping valve and heating stripes can be wrapped around the chamber where ever possible. The magnets of the ion pump can also be removed. This allows the ion pump to be wrapped with heating tape. With moderate power on the heating tape while avoiding heating of the turbo pump, chamber can be heated. The main chamber can also be heated with the MOT coils. Typically, about continuously application of 10 A through MOT coils is enough while making sure the water cooling is off. When the pressure is low enough, heating tapes on the ion pump can be removed and the magnets reinstalled. With the ion pump switched on, it should be possible to revive the original pressure in the MOT following standr UHV procedure.

The ARS CS202*E-DMX-20 cryostat requires less maintenance over several weeks of continuous operation. Slight degradation of the base temperature up 1 to 3K over a span of 1-3 months of continuously operation may be observed and is normal. To regain the lowest possible base temperature, the cryostat can be turned off and warmed up to room temperature with the turbo pump continuously pumping. The cryostat can be then be switched on again and the previously reached pressure should be attained within a few days. After 20 000 h of accumulated operation, the cryostat head will need to be serviced by the company. Otherwise, the gaskets will break and destroy the cryostat head internals entirely.

There are also gas clean up procedures for the helium high pressure lines that can be done once or twice a year to make sure that the high pressure lines are clean. The compressor helium pressure should not go below a certain prescribed level. There is also an adsorber replacement needed for the cryostat after 1-2 years of operation. Some ARS engineers have pointed out that this might not be necessary. For more information and specific details, refer to the cryostat manual. Various photos can also be found on the Atomchip Samba server.

Appendix D

Superconducting Atomchip designs and Misc.

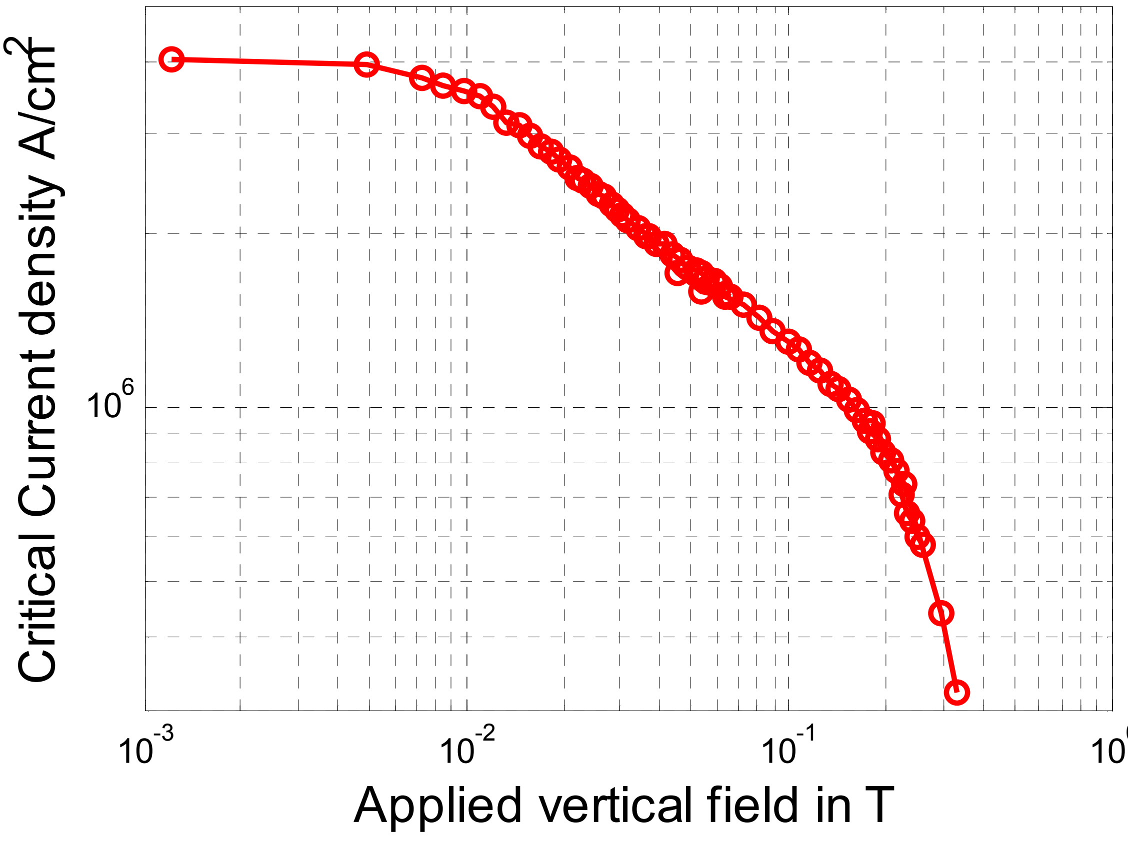

Fig. D.1 I_c vs applied perpendicular field behavior of the Niobium atomchip in figure 6.2

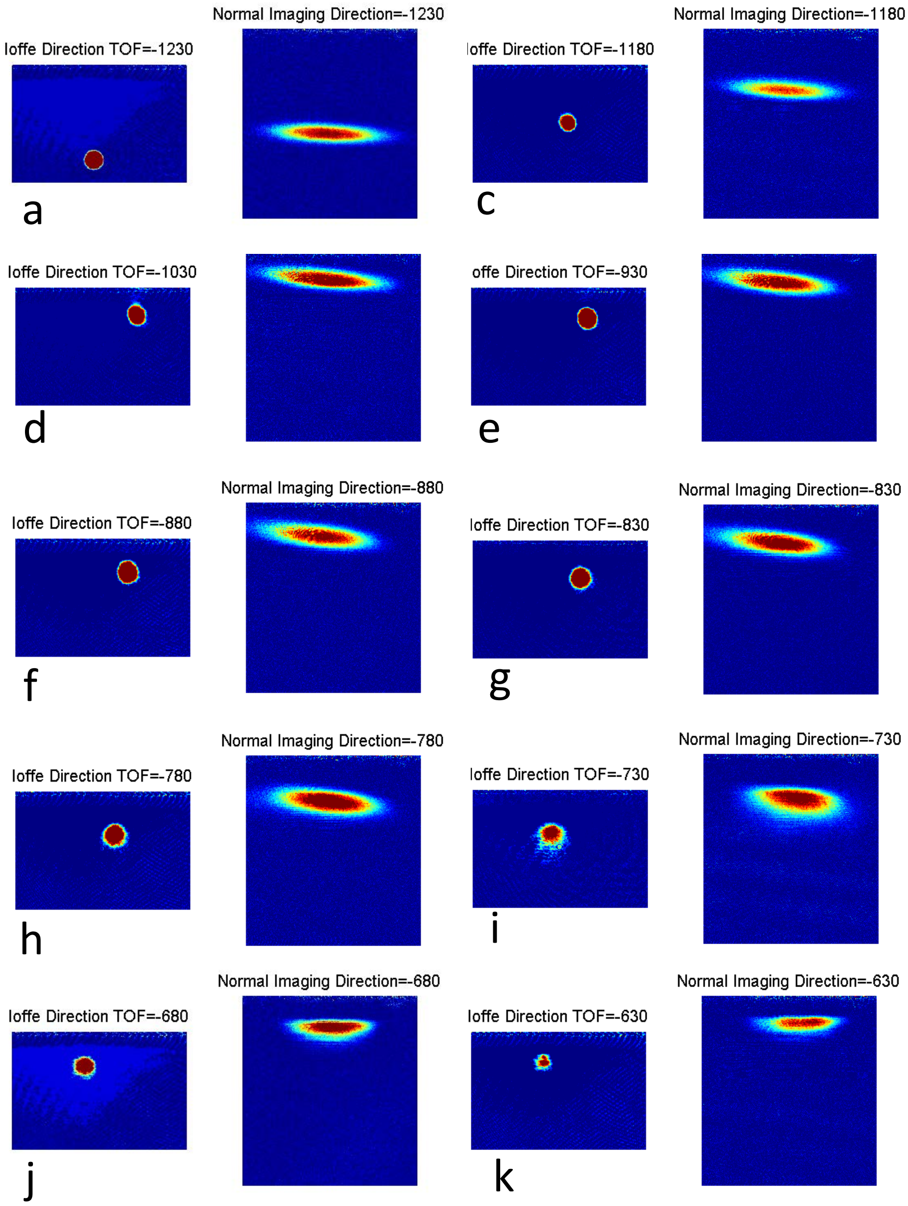

Fig. D.2 Full snapshot movie of the reloading of the superconducting atomchip from the QUIC trap. (a) to (k) are correspond exactly to

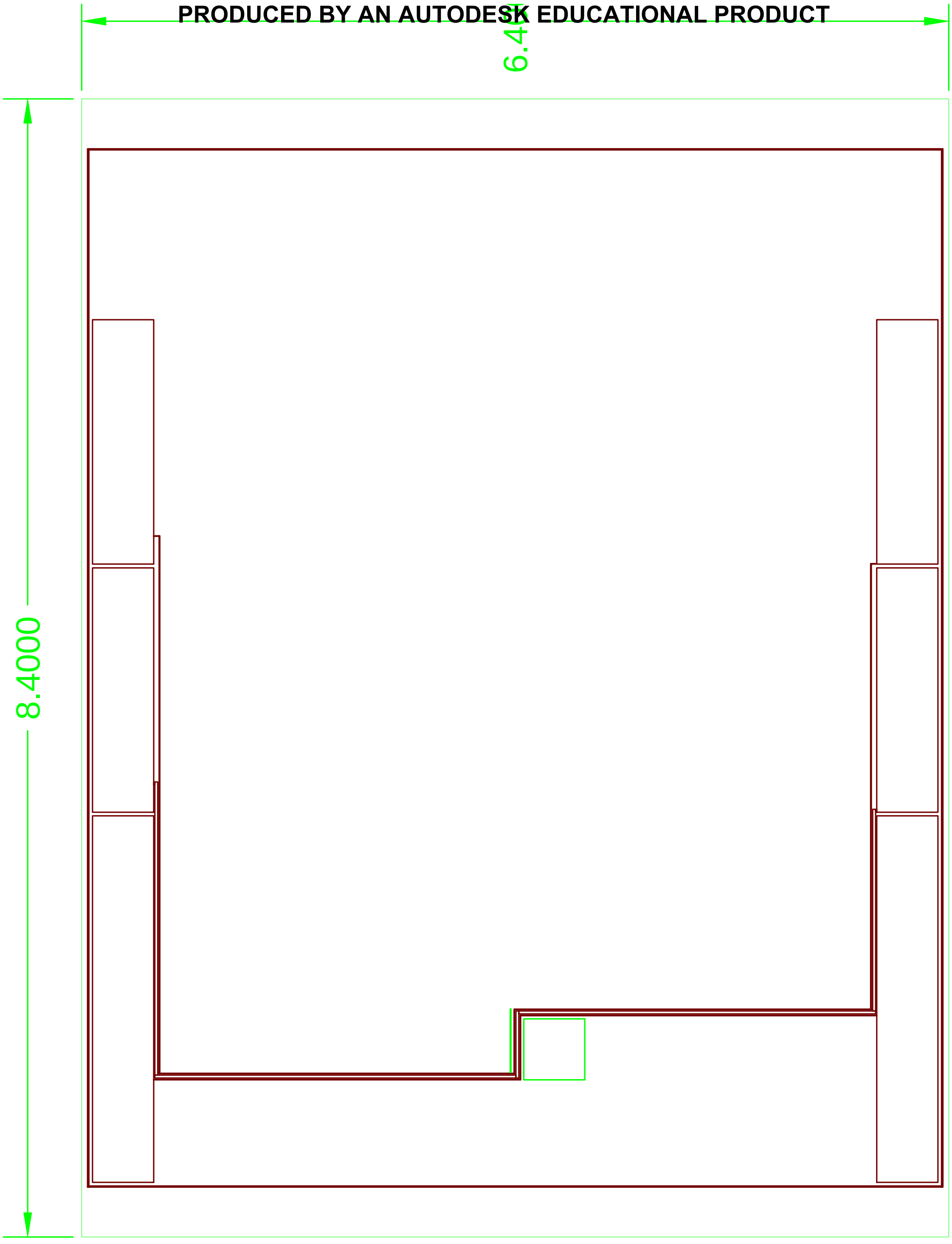

Fig. D.3 YBCO atomchip without resonator.

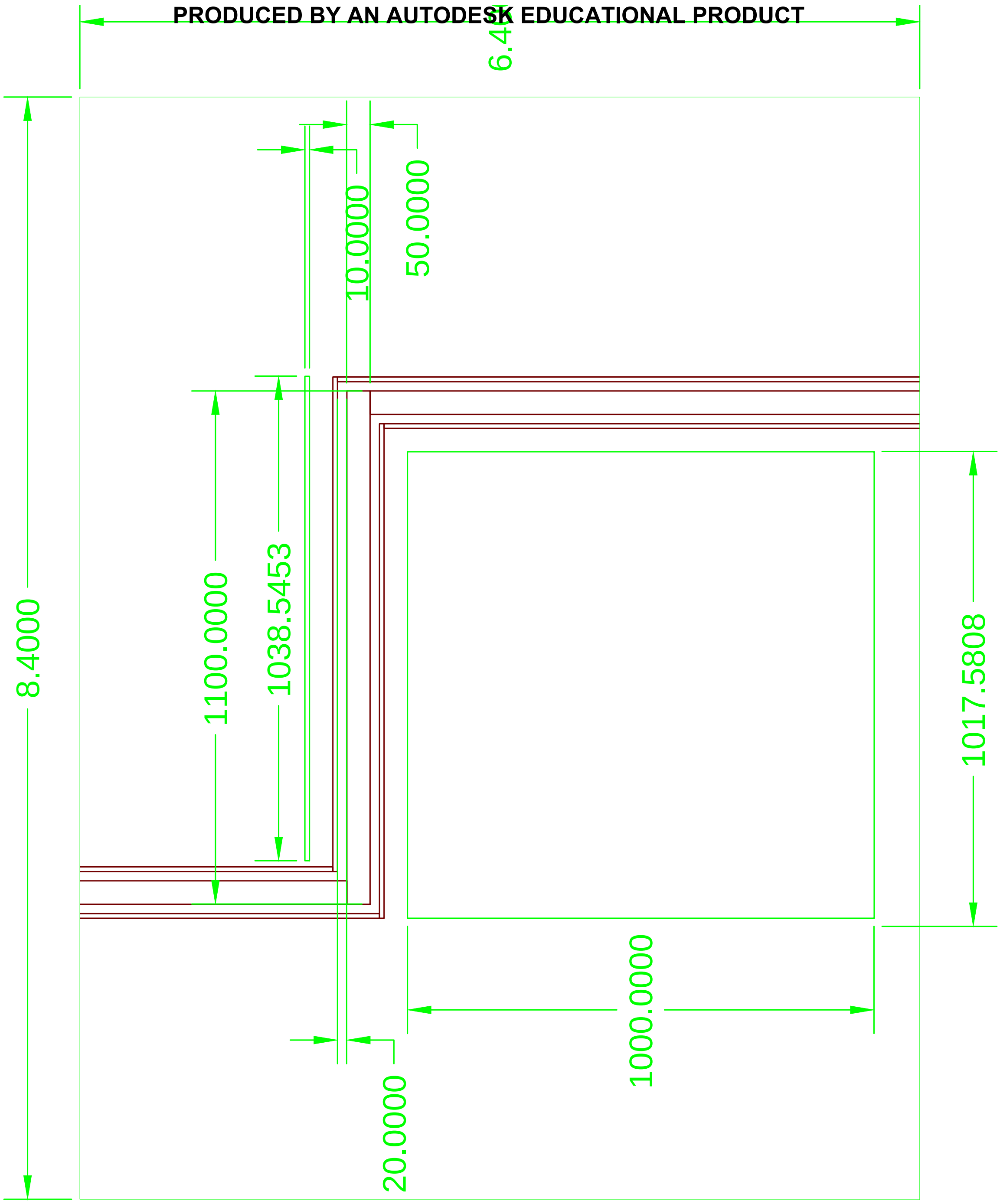

Fig. D.4 A closer view of the YBCO atomchip without resonator.

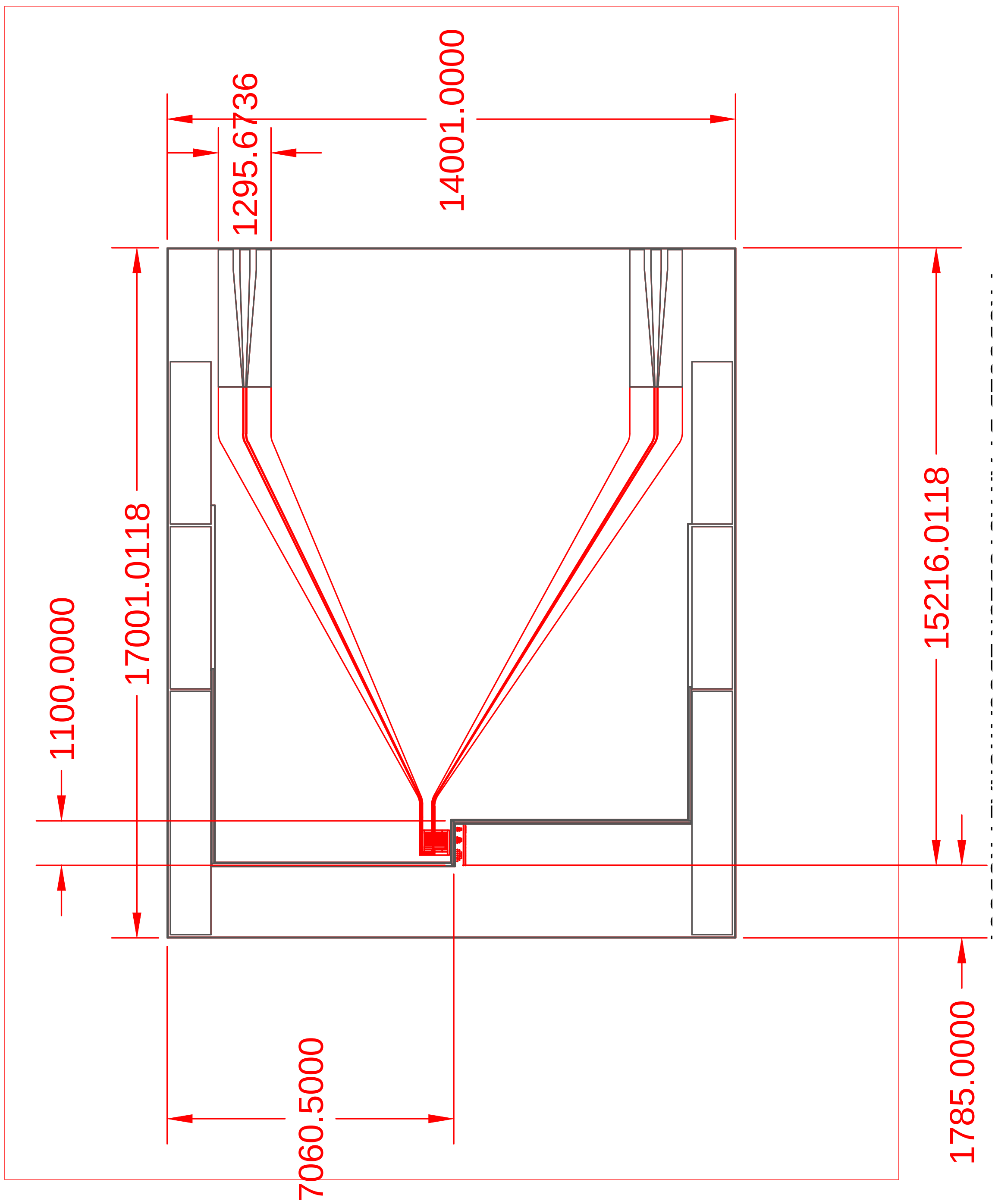

Fig. D.5 YBCO atomchip with resonator and other structures.

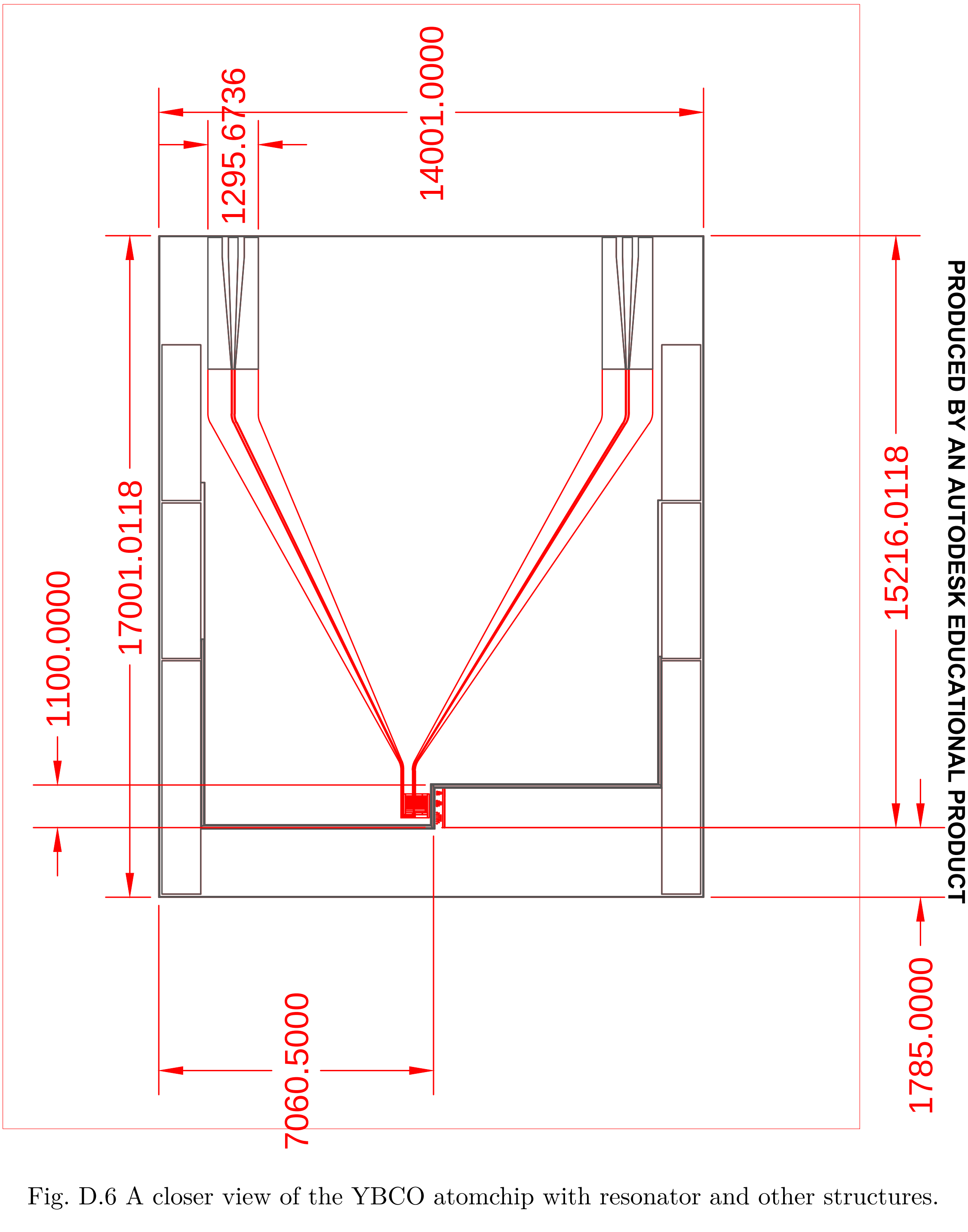

Fig. D.6 A closer view of the YBCO atomchip with resonator and other structures.

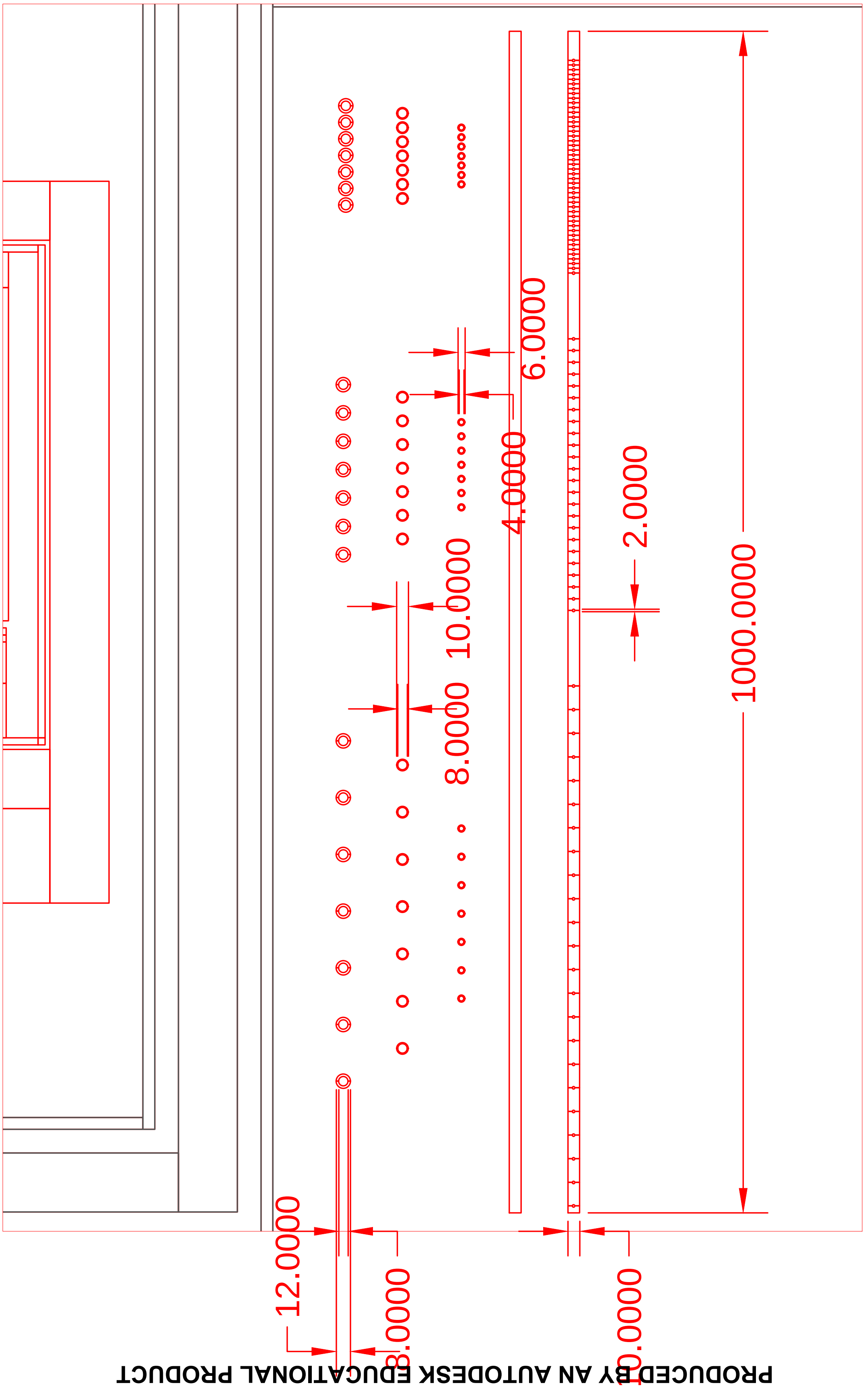

Fig. D.7 A closer view of the YBCO atomchip with resonator and other structures. The Niobium version only has the first big row of rings.

Acknowledgements

This was not the easiest of journeys that I've ever undertook and not the last. My journey in space and time, not in the relativistic sense has brought me to difference places around the world. Meeting different people and to some extent becoming a part of them has certainly broadened my humanity in ways I could never imagine.

Firstly, I will forever be indebted to my supervisor Jörg Schmiedmayer for giving me the opportunity to engage in this experiment that has never before been conceived. His unending enthusiasm and wisdom always brought you back to the proper direction and inspiration. Chapter 7 was mostly due to Jörg telling me to look at the data closely and some interesting stuff were indeed there.

I'd also like to thank my CoQuS thesis advisory committee, Thorsten Schumm for always providing realistic insight and advice. Of course, there were people nearby who were always there for quick physics and technical questions that provided quick knowledge when need at its urgency for the task at hand. I would like to thank Johannes Majer and Michael Trupke for this reason and for reading and correction this thesis. I'd also like to thank the QUIC team old and new: Stefan Haslinger, Christian Novotny, Christoph Hufnagel, Robert Amssues, Stefan Putz, Andreas Angerer, Thomas Astner and Christian Koller.

Superconductivity is serious business which was almost unknown to me when I started. I would like to thank Alvar Sanchez, Oriol Romero-Isart, Mayraluna Lao, Johannes Hecher, Franz Sauerzopf, for the eye-opening discussions and insights about superconductors and what you can do with it.

I would also like to thank the CoQuS doctoral program for important avenue for meeting other physicists. The program allowed me to further my connections and even broadened my scientific circle even further. They are, perhaps, the most brilliant individuals I've ever met.

Lastly, I would like to time this time to thank everyone I've ever met in the atomchip group who has made my experience most memorable. I can never forget the unending support of my experiment colleague, Stefan Minniberger[1]. His patience and insight has kept me sane through the years and has made me my adjustment to his local environment smooth. The others who the Austria awesome and the coffee corner discussions unforgetable: Igor M., Bernhard R., Thomas S., Matthias S., Georg W., Rugway W., Qi L., and the rest. If I forgot, I apologize deeply.

Lastly, my mama and papa, my relatives, my dawata-kini friends, my Kraxen[2] buddies in Vienna. Thank you for the unending support... To the creator whether you really do exist or not... Thank you[3]

[1] Get to the choppa!

[2] You all made everything worth every moment.

[3] And I would like to acknowledge my legs for always supporting me, my arms for always being by my side... Most of all, my fingers.. Because I can always count on them... .

Appl. Phys. B (2014) 116:1017–1021
DOI 10.1007/s00340-014-5790-5

Applied Physics B
Lasers and Optics

Magnetic conveyor belt transport of ultracold atoms to a superconducting atomchip

Stefan Minniberger · Fritz Diorico · Stefan Haslinger · Christoph Hufnagel · Christian Novotny · Nils Lippok · Johannes Majer · Christian Koller · Stephan Schneider · Jörg Schmiedmayer

Received: 21 November 2013 / Accepted: 30 January 2014 / Published online: 18 March 2014

Abstract We report the realization of a robust magnetic transport scheme to bring $>3 \times 10^8$ ultracold ^{87}Rb atoms into a cryostat. The sequence starts with standard laser cooling and trapping of ^{87}Rb atoms, transporting first horizontally and then vertically through the radiation shields into a cryostat by a series of normal- and superconducting magnetic coils. Loading the atoms in a superconducting microtrap paves the way for studying the interaction of ultracold atoms with superconducting surfaces and quantum devices requiring cryogenic temperatures.

1 Introduction

There has been growing interest in studying hybrid quantum systems [1–17]. Superconducting quantum devices are expected to be capable of fast quantum information processing but exhibit only short coherence times making them unsuitable for qubit storage [1]. Hybrid quantum systems promise that coupling to a different system with a long coherence time will allow for high fidelity storage of qubits. The hyperfine spin states in ultracold atoms are a promising candidate [6–12], which can be manipulated with great precision. For experiments with ultracold atoms and superconducting quantum devices, one must be able to efficiently trap ultracold atoms in a cryogenic environment.

Transport of ultracold atomic ensembles is a well established technique to separate the physical experiment from the initial preparation of an ultracold atomic ensemble. Since the first experiments with ultracold quantum gases aim for Bose–Einstein condensation, several transport mechanisms based on moving magnetic traps [18] and moving optical lattices [19] or optical tweezers [20] were developed. Transfer of atoms into a 4K cryogenic environment has been demonstrated with either a single moving magnetic quadrupole trap [21], by operating a MOT in the cryogenic environment [22–24], or using an optical tweezer [25]. We report a robust magnetic transport scheme for ultracold atoms from a room temperature MOT into a cryostat and successful loading into a superconducting atomchip microtrap.

2 Experimental details

The experiment uses a combination of horizontal magnetic transport following [18] and vertical magnetic transport to enter the cryostat. Figure 1 shows a drawing of the entire setup. A 90 degree angle in the path of the transport efficiently blocks stray light from the MOT. The non-overlapping arrangement of the vertical coils allows efficient transition into the cryogenic environment. The MOT chamber is separated by a valve, allowing independent maintenance of the science chamber.

The cryostat is an ultra-low vibration Gifford-McMahon closed cycle cryocooler [26, 27]. It provides a cooling power of about 800 mW at the 4 K stage. The cold finger rests in a CF200 vacuum chamber. An aluminum shield is

Stefan Minniberger and Fritz Diorico have contributed equally to the efforts leading to this paper.

S. Minniberger (✉) · F. Diorico · S. Haslinger · C. Hufnagel · C. Novotny · N. Lippok · J. Majer · C. Koller · S. Schneider · J. Schmiedmayer (✉)
Vienna Center for Quantum Science and Technology, Atominstitut/TU-Wien, Stadionallee 2, 1020 Vienna, Austria
e-mail: sminniberger@ati.ac.at

J. Schmiedmayer
e-mail: schmiedmayer@atomchip.org

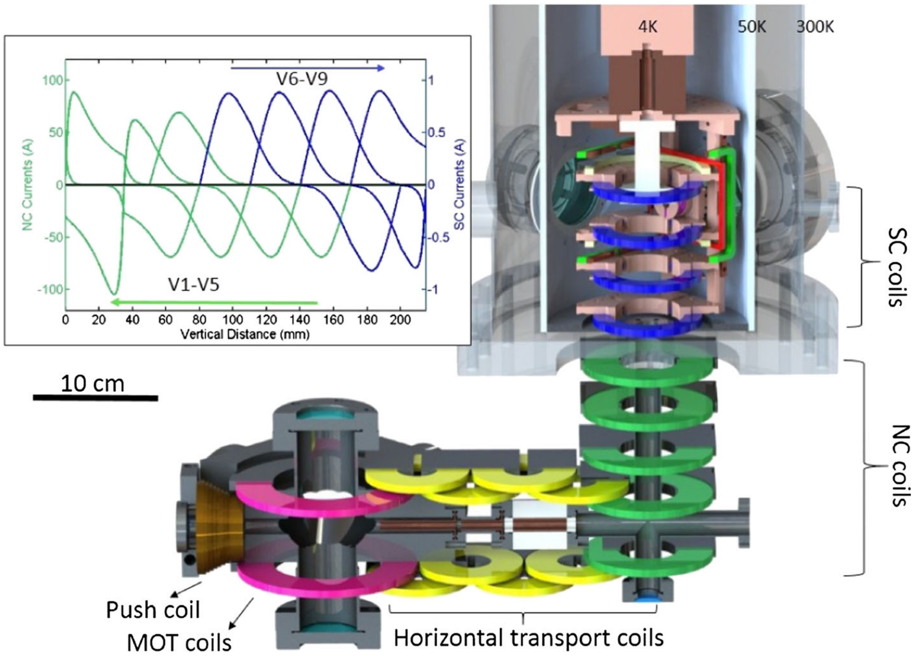

Fig. 1 Cut through a CAD drawing of the setup with the MOT chamber on the bottom left and the copper cage holding the superconducting coils and the chip on the top right. The cryo chamber is made semi-transparent for clarity. The *inset* shows the currents used for the vertical transport. Currents for the normal conducting coils *V1–V5* refer to the *left axis*, while the superconducting coils *V6–V9* are driven with much lower currents (*right axis*)

connected to the 50 K stage. It has four anti-reflection coated windows for optical access and shields the inner part from thermal radiation [28]. To thermally isolate the 50 K shield, its outside is wrapped with several layers of aluminized Mylar foil. Radiation shielding is particularly important for the superconducting wires, therefore all of them are covered with reflective aluminum tape.

The MOT chamber is a pancake-shaped steel octagon that contains the Rb-dispenser. It provides optical access for a standard six beam vapor cell MOT. Following a ten second MOT phase, the atoms are sub-Doppler cooled and then optically pumped into the strongest low-field seeking state $|2,2\rangle$. The initial magnetic trap is loaded with typically 5×10^8 atoms at a temperature of about 300 μK.

2.1 Magnetic transport

To initiate the horizontal transport a so-called push coil shifts the quadrupole trap created by the MOT coils toward the magnetic conveyor belt. Currents for the horizontal section are calculated by defining the zero of the quadrupole field along the transport axis, a constant vertical trap gradient of 130 G/cm and a constant aspect ratio of 1.62.

The vertical transport section consists of nine coils in total, five normal- and four superconducting each with a vertical spacing of 30 mm. The normal conducting coils, which are mounted on water- cooled aluminum bodies, have 40 windings each and are operated up to 100 A. For the superconducting coils, a commercial Niobium–Titanium (NbTi) wire with a thickness of 127 μm is used [27]. Each coil has 3,000 windings and is wound on a copper mounting, consisting of four isolated segments in order to prevent eddy currents. The superconducting coils can be operated up to 3 A.

The last coil pair of the horizontal section also acts as the first two vertical transport coils. To maintain a constant aspect ratio of the trap during transport, four coils are used at the same time. In contrast to the horizontal section, transport along the coil axis in vertical direction requires bipolar operation of the respective currents. For simulating the magnetic field of each coil, the analytic solution is used [29]. The currents $I_i(z)$ for coil i and trap location z along the z-axis are obtained using four conditions $|B(z)| = 0$, $|Bz|' = 130$ G/cm, $|B_z|'' = 0$, and $\sum_{i=1}^{4} N_i{\cdot}I_i = 0$ where N_i is the number of windings per coil. The first three conditions imply a quadrupole trap with zero field at location z and a linear gradient of 130 G/cm. The last condition ensures smooth current over time. By specifying a position function $z(t)$ that contains the desired acceleration and maximum velocity, transport currents $I_i(t)$ are obtained from $I_i(z)$ [30].

A maximum efficiency is achieved by using an acceleration of 0.4 m/s^2 and a maximum velocity of 3 m/s for both horizontal and vertical transport, where the power supplies can accurately reproduce the desired currents. With these settings, the whole magnetic transport sequence takes about two seconds [31].

2.2 Cryogenic setup

The main experimental stage is mounted on the 4K stage of the cold finger. It consists of a copper-cage system that holds the coils and the chip mount. The cryostat contains eleven coils in total, four transport coils, one Ioffe coil, and three

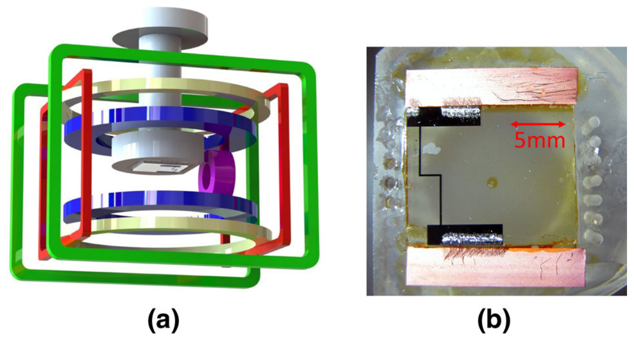

Fig. 2 **a** Coil configuration and the chip mounting in the cryostat, showing the last two transport coils (*blue*), the vertical bias coils (*yellow*), the bias coils for the chip trap (*green*), the bias coils for the third direction (*red*) and the Ioffe coil (*small*, *pink*). **b** Photograph of the actual chip. Several aluminum bonds connect the Nb pads to the high-T_c stripes

coils pairs for homogeneous offset (bias) fields. The upper stage of the coil setup is shown in Fig. 2a. As in most cryogenic experiments, proper anchoring of all wires connecting different temperature stages is crucial. A total of 24 copper wires with a length of 4 m and a diameter of 0.4 mm enter the cryostat. First, the wires are wound around the 50 K stage while minimizing thermal contact using plastic spacers. This increases the length between warm and cold side, hence minimizing heat conduction. Then, the wires are carefully anchored by winding them tightly to the 50 K stage. After entering the 20 K stage, the same scheme is applied: First plastic spacers are used before all wires are put in close contact with the 20 K stage of the cryostat. Commercial high-T_c coated superconductors [27] directly connect the 20 K state and the 4 K stage. They have a smaller cross section than the copper wires, show no ohmic heating while in operation, and their flat structure allows much better thermal contact with the cold finger compared with the round copper wires. At the 4 K stage, the NbTi wires are soldered directly to the high-T_c coated superconductors [27].

The chip mounting is made of single crystal quartz to prevent eddy currents and still have a high thermal conductivity. The chip is made of a Sapphire substrate with a 500-nm-thick sputtered niobium film ($T_c = 9.2$ K). A 100-μm-wide Z-shaped wire with large contact pads is fabricated from this niobium layer with standard lithographic methods. To contact the niobium film, we use aluminum bonds between the contact pads and small pieces of the high-T_c coated superconductors, which can then easily be soldered to the NbTi wires. A maximum current of 1.9 A can be driven through this niobium wire structure, which corresponds to a current density of 3.8×10^6 A/cm^2. This is limited by the ohmic heating from the normal conducting Al bonds. Figure 2b shows the actual chip on the quartz mounting.

3 Results and discussion

At the end of the transport, up to 3×10^8 atoms at about 350 μK are held by the last two superconducting transport coils forming a quadrupole trap. This corresponds to a transport efficiency of about 60 %, which is limited by the background pressure (5×10^{-9} mbar) in the room temperature part of the setup. In principle, the atom number in the cryostat can be increased by upgrading the MOT optics or improving the background pressure in the lower chamber. In the cryostat, the atomic clouds exhibit lifetimes of up to five minutes due to the low pressure in the cryogenic environment. After transport, the atoms are loaded into an intermediate trap using the vertical bias coils in anti-Helmholtz configuration. This allows the quadrupole trap to be connected in series with the Ioffe coil. This forms a quadrupole-Ioffe configuration (QUIC) trap that minimizes heating due to current fluctuations [32]. After switching, the intermediate trap is ramped down, the QUIC trap is ramped up to $I_{\mathrm{QUIC}} = 1.2\,\mathrm{A}$. The atoms are now in a macroscopic trap with trapping frequencies of $(\omega_{\mathrm{long}}, \omega_{\mathrm{radial}})/2\pi = 25,\ 250\,\mathrm{Hz}$ and a trap bottom of 4 G. A slow radio frequency ramp from 30 to 5 MHz precools the atoms in the QUIC trap and increases the density of the cloud by evaporative cooling.

The transverse magnetic field of the Z-wire chip trap is rotated by 45° relative to the corresponding field in the QUIC trap, which is fixed by the axis of the vertical transport. This makes direct loading difficult. This is overcome by implementing a "swing-by maneuver." Figure 3a shows the whole loading sequence used to transfer the atoms from the QUIC trap into the superconducting Z-trap. The sequence starts by moving the QUIC trap closer to the chip with a vertical bias field, B_{vert}, while at the same time moving it off-center with the chip bias field in opposite polarity, $-B_{\mathrm{bias}}$. The actual loading into the chip trap happens in the next step, when I_{QUIC} is ramped to zero, I_{chip} is ramped up and $-B_{\mathrm{bias}}$ is ramped to the actual bias field $+B_{\mathrm{bias}}$. This allows a smooth transition between the two rotated magnetic field configurations. The chip loading sequence was found to be optimal for a ramp time of 500 ms. Due to the high inductivity, the supply electronics do not reproduce faster ramps accurately. Figure 3b shows the atoms in the chip trap at different points during the transfer. The swing-by maneuver is best observed through the longitudinal direction, where the sideward motion of the trap is visible. At the end of the sequence, the superconducting microtrap holds around 2×10^6 atoms at 20 μK. Using a current of $I_{\mathrm{chip}} = 1.12\,\mathrm{A}$ in the Z-wire and a bias field of $B_{\mathrm{bias}} = 7.6\,\mathrm{G}$ results in a trap around 350 μm from the chip surface. The measured trapping frequencies are $(\omega_{\mathrm{long}}, \omega_{\mathrm{radial}})/2\pi = 20,\ 370\mathrm{Hz}$ with a trap bottom of 2 Gauss.

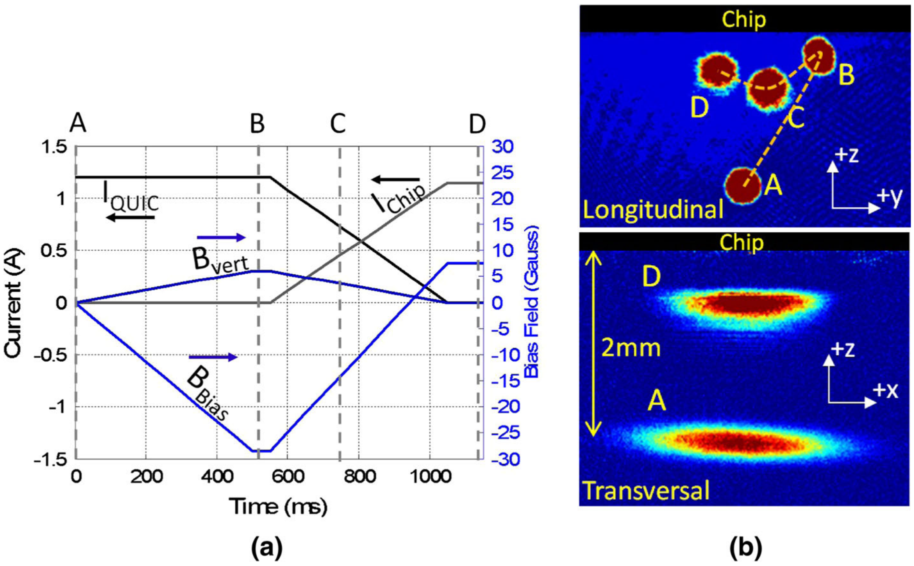

Fig. 3 **a** Current sequence for loading, **b** absorption images of the atoms taken along the longitudinal (*top*) and transversal (*bottom*) axes of the chip trap. Here, four images corresponding to different points throughout the loading sequence are stacked. *A* initial QUIC trap, *B* $-B_{Bias}$ and vertical offset at maximum, *C* middle of the ramp and *D* final chip trap. The *dashed line* shows the trajectory of the atoms through the entire loading sequence

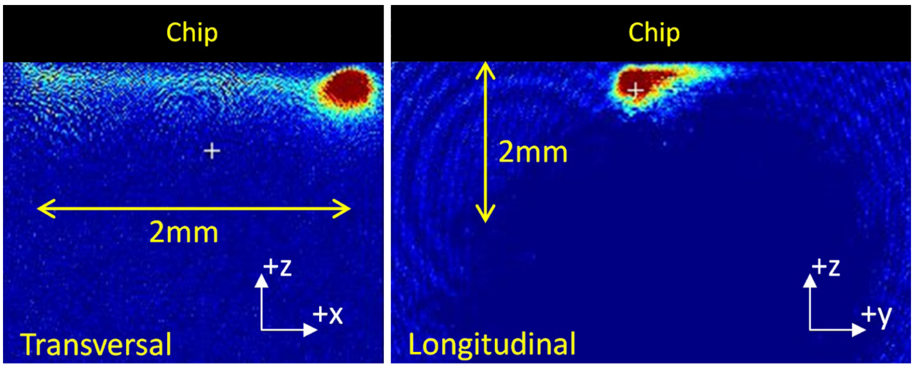

Fig. 4 Meissner trap formation after ramping down I_{QUIC} to zero while leaving only the vertical bias field on. Since the QUIC trap is not centered with respect to the Z-wire, the majority of the atoms are trapped on one of the Z-leads. The rest of the Z-structure is also weakly outlined by the Meissner trap

Bringing the trap closer than 2.5 times, the width of the superconducting wire (here 100 μm) opens it up toward the chip surface due to the Meissner effect [33]. In fact, the Meissner effect can be used to keep atoms close to the surface by applying a vertical bias field [34]. This "Meissner trap" has its minimum at the surface of the superconductor, where the atoms are lost quickly. It can easily be loaded directly from the QUIC trap. Figure 4 shows atoms in the "Meissner trap" along the superconducting surface of the Z-wire.

4 Summary and outlook

We have successfully transported thermal atoms into a cryogenic environment and trapped them on a superconducting atomchip. The magnetic conveyor belt shows high robustness due to the absence of alignment sensitive parts and avoids the operation of a MOT close to superconducting surfaces. Furthermore, the turnaround time for modifications in the science chamber is less than a day due to cryopumping. The transport scheme described here is fully compatible with a dilution refrigerator since they have similar cooling powers at the 4 K stage. This will enable experiments where ultracold atoms interact with superconducting quantum circuits. A superconducting microwave resonator can be integrated on the atomchip to study the coupling of ultracold atoms to microwave photons. Ultracold atoms near superconducting surfaces also open the possibility to use unique superconducting lattice traps [35]. Furthermore, being able to transport ultracold atoms into a cryostat allows sympathetic cooling of buffer gas cooled atoms or molecules [36], reduction of the blackbody radiation-induced light shifts in optical lattice clocks [37], and the usage of cold atoms to probe surfaces at cryogenic temperatures [38, 39].

Acknowledgments SM and FD would like to acknowledge the support of the COQUS doctoral program. This work was funded through the European Union Integrated Project SIQS and the Austrian Science Fund FWF (Wittgenstein Prize, SFB FOQUS).

References

1. R.J. Schoelkopf, S.M. Girvin, Wiring up quantum systems. Nature **451**, 664–669 (2008)

2. M. Wallquist, K. Hammerer, P. Rabl, M. Lukin, P. Zoller, Hybrid quantum devices and quantum engineering. Phys. Scr. **2009**(T137), 014001 (2009)
3. Z.-L. Xiang, J. Sahel Ashhab, Q. You, N. Franco, Hybrid quantum circuits: superconducting circuits interacting with other quantum systems. Rev. Mod. Phys. **85**, 623–653 (2013)
4. P. Rabl, D. DeMille, J.M. Doyle, M.D. Lukin, R.J. Schoelkopf, P. Zoller, Hybrid quantum processors: molecular ensembles as quantum memory for solid state circuits. Phys. Rev. Lett. **97**, 033003 (2006)
5. A. Andre, D. DeMille, J.M. Doyle, M.D. Lukin, S.E. Maxwell, P. Rabl, R.J. Schoelkopf, P. Zoller, Wiring up quantum systems. Nat. Phys. **2**, 636–642 (2008)
6. A.S. Sørensen, C.H. van der Wal, L.I. Childress, M.D. Lukin, Capacitive coupling of atomic systems to mesoscopic conductors. Phys. Rev. Lett. **92**, 063601 (2004)
7. D. Petrosyan, M. Fleischhauer, Quantum information processing with single photons and atomic ensembles in microwave coplanar waveguide resonators. Phys. Rev. Lett. **100**, 170501 (2008)
8. D. Petrosyan, G. Bensky, G. Kurizki, I. Mazets, J. Majer, J. Schmiedmayer, Reversible state transfer between superconducting qubits and atomic ensembles. Phys. Rev. A **79**, 040304 (2009)
9. J. Verdú, H. Zoubi, Ch. Koller, J. Majer, H. Ritsch, J. Schmiedmayer, Strong magnetic coupling of an ultracold gas to a superconducting waveguide cavity. Phys. Rev. Lett. **103**, 043603 (2009)
10. K. Henschel, J. Majer, J. Schmiedmayer, H. Ritsch, Cavity QED with an ultracold ensemble on a chip: prospects for strong magnetic coupling at finite temperatures. Phys. Rev. A **82**, 033810 (2010)
11. M. Hafezi, Z. Kim, S.L. Rolston, L.A. Orozco, B.L. Lev, J.M. Taylor, Atomic interface between microwave and optical photons. Phys. Rev. A **85**, 020302 (2012)
12. S. Bernon, H. Hattermann, D. Bothner, M. Knufinke, P. Weiss, F. Jessen, D. Cano, M. Kemmler, R. Kleiner, D. Koelle, J. Fortágh, Manipulation and coherence of ultra-cold atoms on a superconducting atom chip. Nat. Commun. **4**, 2380 (2013)
13. R. Amsüss, Ch. Koller, T. Nöbauer, S. Putz, S. Rotter, K. Sandner, S. Schneider, M. Schramböck, G. Steinhauser, H. Ritsch, J. Schmiedmayer, J. Majer, Cavity qed with magnetically coupled collective spin states. Phys. Rev. Lett. **107**, 060502 (2011)
14. H. Wu, R.E. George, J.H. Wesenberg, K. Mølmer, D.I. Schuster, R.J. Schoelkopf, K.M. Itoh, A. Ardavan, J.L. Morton, G. Briggs, D. Andrew, Storage of multiple coherent microwave excitations in an electron spin ensemble. Phys. Rev. Lett. **105**, 140503 (2010)
15. D.I. Schuster, A.P. Sears, E. Ginossar, L. DiCarlo, L. Frunzio, J.J.L. Morton, H. Wu, G.A.D. Briggs, B.B. Buckley, D.D. Awschalom, R.J. Schoelkopf, High-cooperativity coupling of electron-spin ensembles to superconducting cavities. Phys. Rev. Lett. **105**, 140501 (2010)
16. Y. Kubo, F.R. Ong, P. Bertet, D. Vion, V. Jacques, D. Zheng, A. Dréau, J.F. Roch, A. Auffeves, F. Jelezko, J. Wrachtrup, M.F. Barthe, P. Bergonzo, D. Esteve, Strong coupling of a spin ensemble to a superconducting resonator. Phys. Rev. Lett. **105**, 140502 (2010)
17. A. Imamoğlu, Cavity QED based on collective magnetic dipole coupling: spin ensembles as hybrid two-level systems. Phys. Rev. Lett. **102**, 083602 (2009)
18. M. Greiner, I. Bloch, T.W. Hänsch, T. Esslinger, Magnetic transport of trapped cold atoms over a large distance. Phys. Rev. A **63**, 031401 (2001)
19. S. Schmid, G. Thalhammer, K. Winkler, F. Lang, J.H. Denschlag, Long distance transport of ultracold atoms using a 1d optical lattice. New J. Phys. **8**(8), 159 (2006)
20. A.P. Chikkatur, Y. Shin, A.E. Leanhardt, D. Kielpinski, E. Tsikata, T.L. Gustavson, D.E. Pritchard, W. Ketterle, A continuous source of Bose–Einstein condensed atoms. Science **296**(5576), 2193–2195 (2002)
21. T. Mukai, C. Hufnagel, A. Kasper, T. Meno, A. Tsukada, K. Semba, F. Shimizu, Persistent supercurrent atom chip. Phys. Rev. Lett. **98**, 260407 (2007)
22. C. Roux, A. Emmert, A. Lupascu, T. Nirrengarten, G. Nogues, T. Brune, J.M. Raimond, S. Haroche, Bose–Einstein condensation on a superconducting atom chip. Eur. Phys. Lett. **81**, 81 (2008)
23. T. Nirrengarten, A. Qarry, C. Roux, A. Emmert, G. Nogues, M. Brune, J.M. Raimond, S. Haroche, Realization of a superconducting atom chip. Phys. Rev. Lett. **97**, 200405 (2006)
24. F. Jessen, M. Knufinke, S. C. Bell, P. Vergien, H. Hattermann, P. Weiss, M. Rudolph, M. Reinschmidt, K. Meyer, T. Gaber, D. Cano, A. Günther, S. Bernon, D. Koelle, R. Kleiner, J. Fortágh. Trapping of ultracold atoms in a ^{3}He/^{4}He dilution refrigerator. Appl. Phys. B 1–7 (2013). doi:10.1007/s00340-013-5750-5
25. M.A. Naides, R.W. Turner, R.A. Lai, J.M. DiSciacca, B.L. Lev, Trapping ultracold gases near cryogenic materials with rapid reconfigurability. Appl. Phys. Lett. **103**(25), 251112 (2013)
26. P.B. Antohi, D. Schuster, G.M. Akselrod, J. Labaziewicz, Y. Ge, Z. Lin, W.S. Bakr, I.L. Chuang, Cryogenic ion trapping systems with surface-electrode traps. Rev. Sci. Instrum. **80**(1), 013103 (2009)
27. Cryostat: Advanced Research Systems (arscryo.com), Type ARS CS210*F-GMX-20, high-Tc wires: Superpower Inc. (http://www.superpower-inc.com), Type SCS4050, Niobium–Titanium wires: Supercon Inc.(superconinc.com), Type 54S43
28. T. McMillan, P. Taborek, J.E. Rutledge, A low drift high resolution cryogenic null ellipsometer. Rev. Sci. Instrum. **75**(11), 5005 (2004)
29. J. Simpsons, J. Lane, C. Immer, R. Youngquist, Simple analytic expressions for the magnetic field of a circular current loop. NASA technical documents, 2001
30. N. Lippok, A magnetic transport for ultracold atoms. Master's thesis, Atominstitut TU Wien, Austria, 2008
31. S. Haslinger, Cold atoms in a cryogenic environment. PhD thesis, Atominstitut TU Wien, Austria, 2011
32. T. Esslinger, I. Bloch, T.W. Hänsch, Bose–Einstein condensation in a quadrupole-Ioffe-configuration trap. Phys. Rev. A **58**, R2664–R2667 (1998)
33. V. Dikovsky, V. Sokolovsky, B. Zhang, C. Henkel, R. Folman, Superconducting atom chips: advantages and challenges. Eur. J. Phys. D **51**(2), 247–259 (2008)
34. C. Hufnagel, Superconducting microtraps for ultracold atoms. PhD thesis, Atominstitut TU Wien / NTT Japan, 2011
35. O. Romero-Isart, C. Navau, A. Sanchez, P. Zoller, J.I. Cirac, Superconducting vortex lattices for ultracold atoms. Phys. Rev. Lett. **111**, 145304 (2013)
36. S. Doret, C. Colin, K. Wolfgang, D. John, Buffer-gas cooled Bose–Einstein condensate. Phys. Rev. Lett. **103**(10), 103005 (2009)
37. J.A. Sherman, N.D. Lemke, N. Hinkley, M. Pizzocaro, R.W. Fox, A.D. Ludlow, C.W. Oates, High-accuracy measurement of atomic polarizability in an optical lattice clock. Phys. Rev. Lett. **108**(15), 153002 (2012)
38. S. Wildermuth, S. Hofferberth, I. Lesanovsky, S. Groth, P. Krüger, J. Schmiedmayer, I. Bar-Joseph, Sensing electric and magnetic fields with Bose–Einstein condensates. Appl. Phys. Lett. **88**(26), 264103 (2006)
39. A. Emmert, A. Lupacu, G. Nogues, M. Brune, J.M. Raimond, S. Haroche, Measurement of the trapping lifetime close to a cold metallic surface on a cryogenic atom-chip. Eur. J. Phys. D **51**(2), 173–177 (2009)